university of groningen / faculty of science and engineering / nanoscience

Detailed balance in the Numerical Integration of the Schrödinger Equation

Master Thesis

For the Physics Master,
Quantum Universe track (theoretical physics)

by

Pieter van Vliet

Supervisor/First Examiner:

prof. dr. T.L.C. Jansen

Second Examiner:

prof. dr. A. Borschevsky

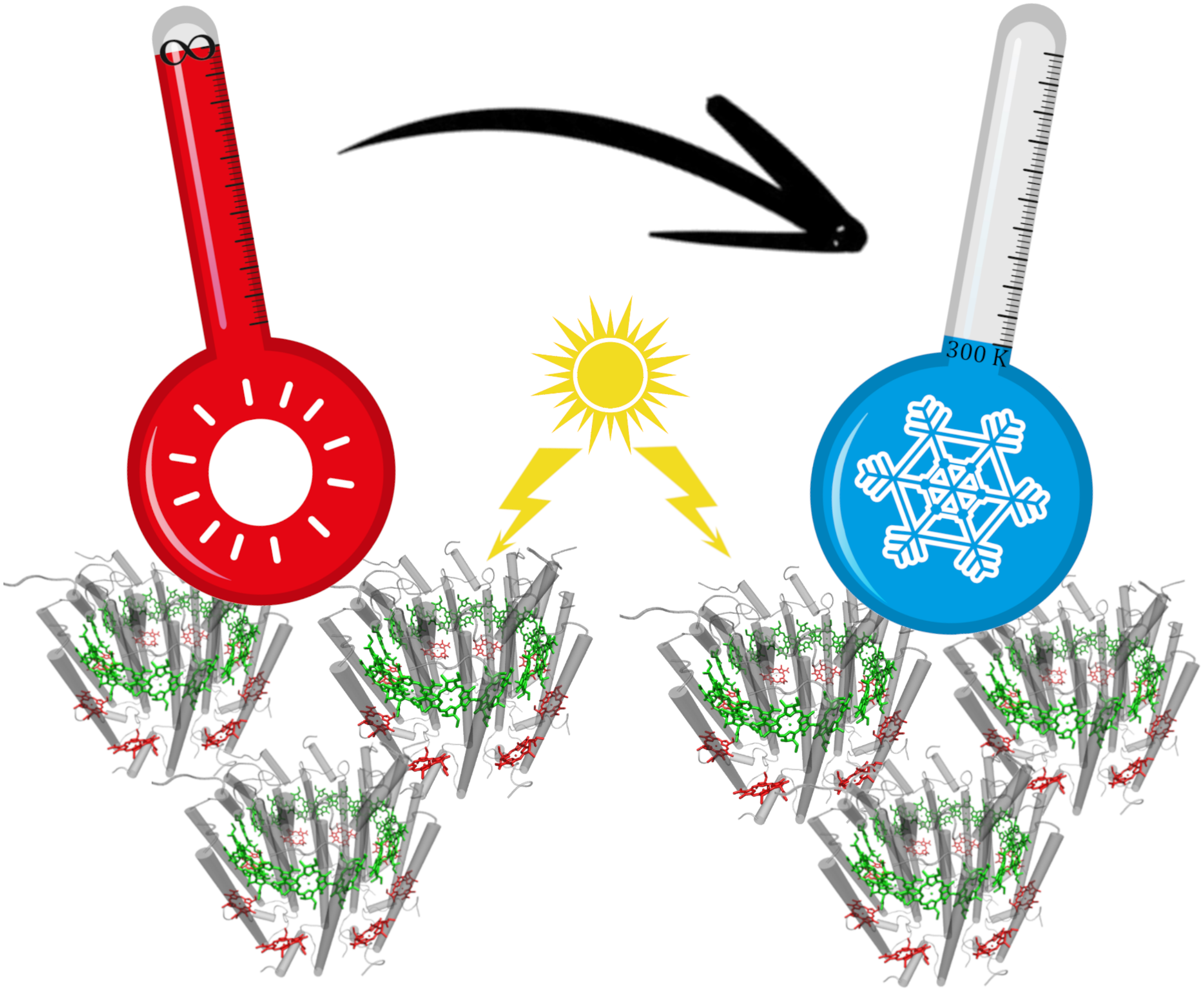

A schematic overview of the problem tackled in this research: addressing thermalisation (finite-temperature effects) in open quantum systems, such as the LH2 light harvesting complex found in the purple bacteria *Rhodospirillum (Rsp.) molischianum* at the bottom of the figure (adapted with permission from Ref. 1, © 2015, American Chemical Society). Vector images by freepik.com

Abstract

In this research, I have examined two methods of including detailed balance in the otherwise temperature-agnostic Numerical Integration of the Schrödinger Equation (NISE) method of quantum mechanical population. These methods are compared to the Hierarchical Equations of Motion (HEOM), a 'gold standard' in quantum dynamics. The models studied are Frenkel exciton Hamiltonians with dynamic disorder given by overdamped Brownian harmonic oscillator coordinates. These models include subsystems of the Fenna-Matthews-Olson (FMO) complex, the LH2 complex and the amide I and II modes, along with numerous artificial systems. While not always reproducing the HEOM results closely, both methods provide an improvement on the NISE results, especially in the regime of small (or slowly-fluctuating) dynamic disorder. The computationally favourable scaling of these two methods will hopefully allow for the cheap computation of two-dimensional electronic spectra (2DES) and allow meaningful comparison to experimental results.

Contents

Conventions

In this work, we make use of Dirac notation to denote our wavefunctions, operators and expectation values, similar to most other modern works in quantum mechanics [2,3]. Our conventions do not stray far from those outlined in those works, and the reader is referred there for a more thorough discussion of quantum mechanics.

Occasionally, we will use the quantum mechanical *density matrix formalism* described in Ref. 2. Important are the definition of *populations* and *coherences*. Note that these definitions are independent of basis, but that their physical meanings are not.

Definition 1. *Population: A diagonal component of the density matrix, denoting the probability of finding the system in the corresponding basis state.*

Definition 2. *Coherence: An off-diagonal component of the density matrix, denoting a phase relation between two basis states.*

Our operators and wavefunctions are embedded in an N-dimensional Hilbert space, where N indicates the number of possible states our system N_m molecules can be in. We shall consider $N = N_m$ for our excitonic Hamiltonians, due to the fact that both the ground state and higher-order excited states are inaccessible on short timescales. In more technical language, our systems live on a *single-exciton manifold*.

Throughout this work, reference will be made to Numerical Integration of the Schrödinger Equation (NISE), according to conventions established in Ref. 4, which is another name for the Ehrenfest method without quantum feedback on the bath, according to conventions in Ref. 5.

Definition 3. *Local basis: A basis composed of* vectors *or* fuctions *corresponding to individual chromophores. Also called 'site basis'.*

Definition 4. *Average eigenbasis: A basis composed of vectors corresponding to the eigenstates of the average (or ideal) Hamiltonian.*

Definition 5. *Adiabatic basis: A basis composed of time-dependent vectors corresponding to the instantaneous eigenstates of the Hamiltonian.*

Chapter 1

General Introduction

In this chapter, we will be talking about the main motivations behind this work. The first section will cover the need for research into natural and artificial light harvestings from a societal standpoint. The second section will cover the recent developments in quantum biology. The third section is a brief introduction to the multiscale modelling paradigm through which light harvesting systems are studied computationally. The fourth section will cover the theoretical methods used to describe exciton transport in biological systems, their benefits and drawbacks, and the proposed solutions to some of their drawbacks.

1.1 Light harvesting

A significant and pressing problem of our time is the transition to clean and abundant energy. With energy consumption, and the associated production of CO_2, rising quickly, it is imperative that renewable energy sources are developed. Of all renewable energy sources, solar energy takes the largest exploitable share by far [6, 7], and thus it will have to play a large role in the energy transition. For aeons, it has played the deciding role in the production of biochemical organic matter [8]. Although very little is known about the origins of photosynthesis, there is suggestive evidence that photosynthetic organisms were already present between 3.5 and 3.2 billion years ago [9]. Modern human research into light harvesting, however, only started slightly less than two centuries ago, with Alexandre Becquerel discovering the photovoltaic effect [10]. Research into photovoltaics has yielded systems that are much more efficient than natural light-harvesting in plants when considering annual yield [11]. One of the reasons for this is that plants must be robust and protect their biological systems against variations in light intensity, and especially high light exposure [12–14]. However, there are bacteria that have significantly higher photosynthetic efficiency than plants [15], though the definitions of efficiency vary slightly between Refs. 11 and 15.

As an example, let us consider *Rhodospirillum (Rsp.) photometricum*, a purple bacterium whose light-harvesting complexes manage to capture light even in the most low-light conditions imaginable [6,16]. The pathway from photonic to chemical energy starts at chromophores (light-harvesting molecules) arranged into so-called 'antenna systems', which are excited by incoming photons. From these antennae, the excitation energy transport (EET) takes this excitation to the photosynthetic reaction centre (RC), where it is converted to a long-lived charge-separated state. This provides the potential energy needed for the formation of complex biological molecules.

In *Rsp. photometricum*, the bacteriochlorophyll chromophores are grouped into two complexes: LH1 (chromophores surrounding the reaction centre) and LH2 (the 'antennae'). Research has shown that bacteria adapted to low-light conditions contain significantly more LH2 complexes, meaning a larger area which is able to receive light. A diagram of this phenomenon, taken from Ref. 16, is shown in Fig. 1.1. In such situations, excitation energy must travel for a long time before reaching a reaction centre, and efficient EET is a prerequisite for the viability of photosynthetic energy production [17].

If we want to learn from nature and facilitate our transition to cleaner energy, we must look at these systems and find the factors that contribute to their efficiency of light-harvesting and EET. For this, we need physical (and computational) models. This brings us to the motivation behind this study: the development of computationally cheap and accurate methods of simulating EET in light-harvesting systems.

1.2 Quantum biology

Recent research has uncovered a wealth of new possibilities for the field of quantum biology [18]: the supposed measurement of long-lived quantum coherences in biological systems such as light harvesting systems has become a recent interest for many researchers. Research suggests the discovery of such coherences in cryogenic environments (77 K) in the Fenna-Matthews-Olson (FMO) complex of the green sulphur bacterium (GSB) *Chlorobium tepidium* [19] and in the purple bacterium *Rhodobacter sphaeroides* [20], but more recent research has also provided suggestive evidence of coherences surviving at timescales of longer than 100 fs at ambient temperatures in the FMO complex of *C. tepidium* [21], long

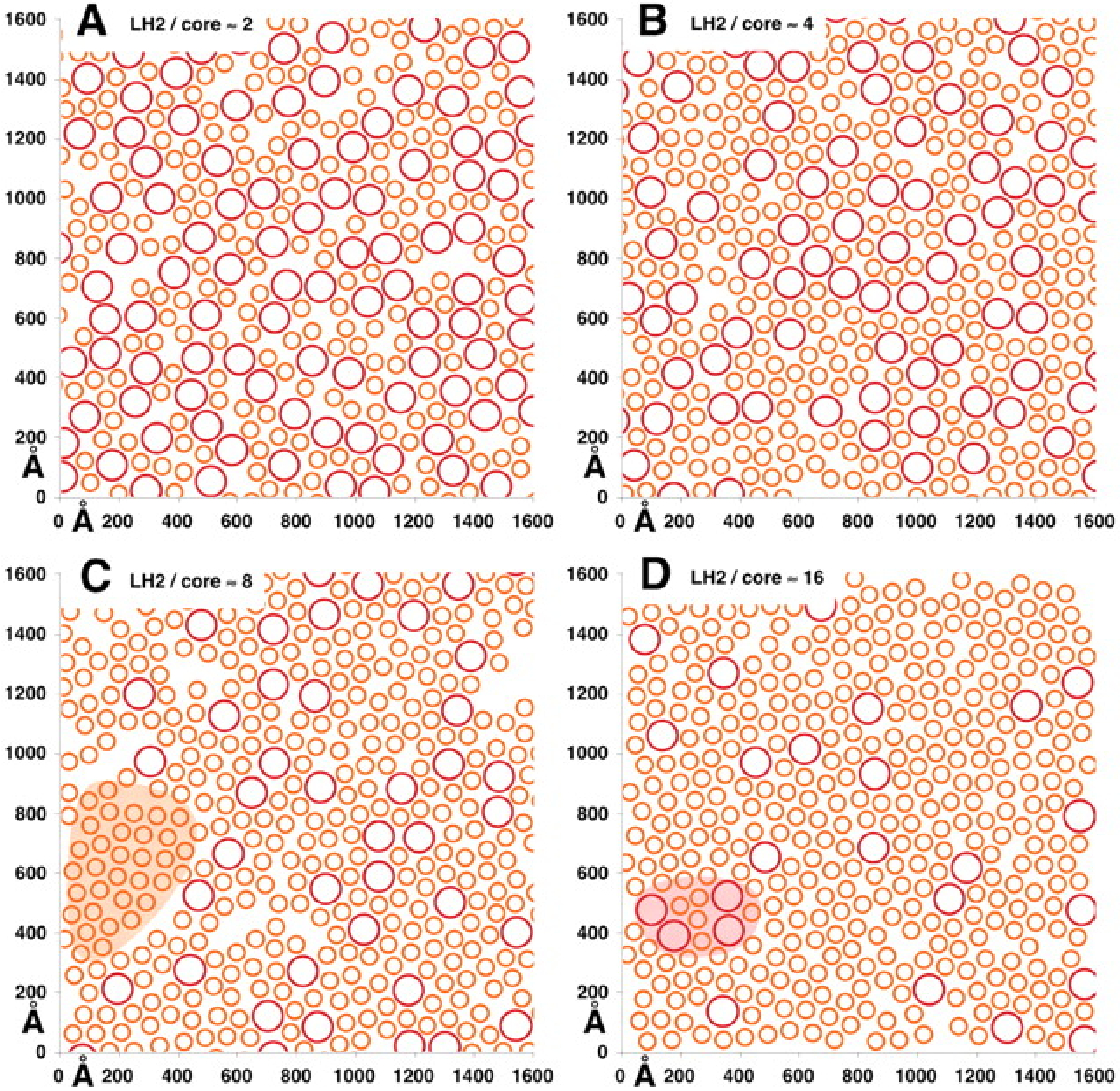

FIGURE 1.1: The dependence of the concentration of reaction centres against LH2 antennae on light intensity, as determined by computational modelling. The density of LH2 complexes (orange circles) with respect to the number of LH1 complexes with reaction centres (bigger red circles) is displayed in the top-left corner of each subfigure. (A) and (B) represent biological systems adapted to high-light conditions, with only (B) observed experimentally. (C) and (D) show systems adapted to low-light conditions, with only (C) observed experimentally. Reprinted with permission from Ref. 16.

enough to have an effect on EET.

However, these long-lived coherences can actually be explained by the coupling between electronic and vibrational states, which does not have such a clear-cut connection to EET. This can produce long-lived oscillations (so-called ‘quantum beats’) in optical spectra [22–24]. Neglecting this coupling in a model falsely suggests that oscillations due to electronic coherence are the only possible source of these quantum beats.

A reason that can explain the confusion, is given in Ref. 24, and boils down to the different language used between theory and experiment. In order to understand properly what is meant by coherences, the reader is firstly referred to the Conventions laid out at the beginning of this work. The technical definition of a coherence is an off-diagonal element of the quantum mechanical density matrix. However, due to a free choice of basis, there is no single physical explanation of a coherence that describes what happens in a biological system. As mentioned in Ref. 24, defining the coherences specifically in the average eigenbasis, has the most relevance to optical experiments. This is associated with the *excitonic* picture [25–27]: instead of a single molecule being excited, this excitation is shared in a coherent superposition of multiple chromophores. More in-depth discussion of the coherences and different bases is given in Chapter 2.

1.3 Multiscale modelling

Given the large number of possible structural configurations of organic molecules in aggregates, we need a way to translate molecular structure into optical properties. This is a highly non-trivial problem, since current experimental techniques are not able to resolve such structure at molecular level. To validate which structures contribute to the optical properties observed in these aggregates, we must rely on the multiscale modelling paradigm [28]. This combines several types of modelling. Firstly, experimental constraints provide initial structures for our aggregates. These structures are assessed with a Frenkel exciton model without dynamic disorder. Any structures that do not provide a reasonable explanation of experimental spectra will be discarded, and we will continue with those structures that do. After this, molecular dynamics (MD) simulations and electrostatic calculations on the molecular level provide time-dependent trajectories (including dynamic disorder) of the Frenkel exciton Hamiltonian. Finally, using these time-dependent Hamiltonians, more accurate optical spectra are modelled. A flowchart of the methodology is presented in Fig. 1.2.

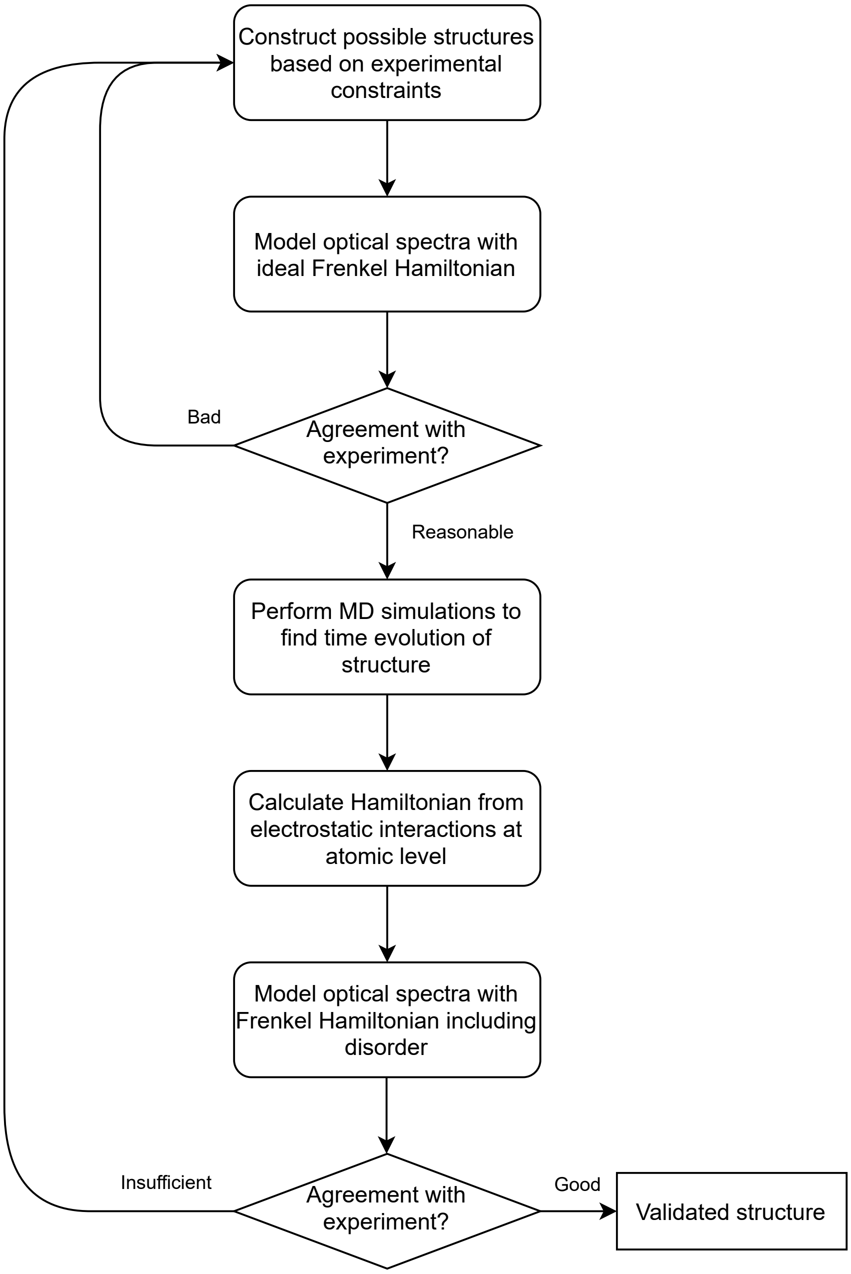

FIGURE 1.2: A flowchart of the multiscale modelling methodology, inspired by Ref. 28.

1.3.1 Modelling optical spectra

Interpretation of optical experiments is key to determining the validity of particular models of light harvesting. Two methods of studying light harvesting systems are two-dimensional electronic and infrared spectroscopy (2DES [29] and 2DIR [30], respectively), while more methods are being developed and studied, such as fluorescence-detected two-dimensional electronic spectroscopy [31]. With any theoretical model, we must ask ourselves how well it is able to predict experimental data. For this, computational spectroscopy is necessary. However, this work will not focus on that particular part of the multiscale modelling workflow.

1.3.2 Focusing on quantum dynamics

From experiment, molecular dynamics (MD) simulations and electrostatic calculations, it might become evident that the system can be modelled with simpler parameters, allowing us to skip the MD simulations and electrostatic calculations altogether. Provided that the bath fluctuates quickly enough, we can model the diagonal elements of the Hamiltonian as overdamped Brownian harmonic oscillators. This allows us to quickly generate many bath trajectories and start optical modelling, thus circumventing the laborious MD step.

The eventual goal of this research is to validate a new method of simulating quantum dynamics in open quantum systems, as discussed in Section 1.4. To test this, we will compare the results of a quantum dynamics simulation to the results given by the Hierarchical Equations of Motion (HEOM), a purported 'gold standard' of quantum dynamics. Since similar quantum dynamics yield similar optical spectra, this research will not cover the optical modelling step, and instead compare the quantum dynamics between different methods. This research method is shown in the flowchart in Fig. 1.3.

The quantum dynamics that will be simulated are *waiting-time* or *population time* dynamics, corresponding to t_2 of the 2D optical experiments [30]. This means that the density matrix will start out in a *population*, after which *coherences* will form that cause oscillations in population.

1.4 Semi-classical methods

Theoretical models suggest that long-lived quantum coherences in light harvesting systems are responsible for their efficiency [32]. To study the implications of these statements, it is

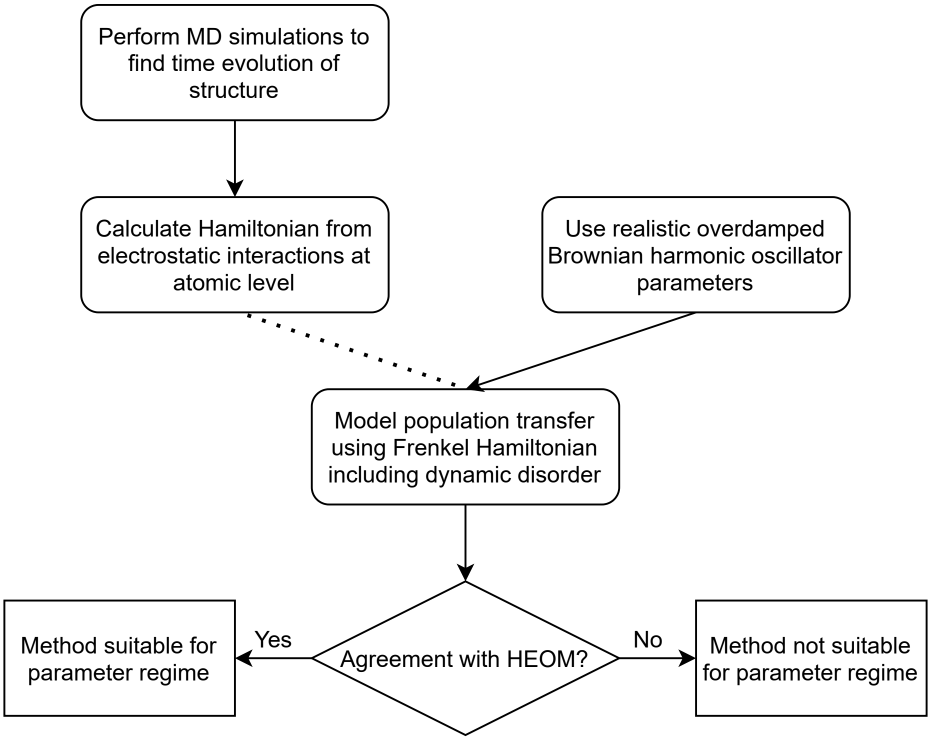

FIGURE 1.3: The flowchart according to which this research is done. The agreement betweeen different models of quantum mechanical population transfer is used as a metric to decide whether a new semi-classical method is able to describe a particular system.

useful to view light harvesting systems as *open quantum systems*. This view distinguishes a *system* consisting of an arbitrary number of states connected to a *bath*, whose quantum mechanical properties are of less interest (because, for instance, they do not display strong absorptive qualities). Due to the loss of information about the bath, the system itself loses its coherence: after a certain amount of time, it is no longer in a pure quantum state [2]. A question that arises from this, is how quantum coherences can survive for a significantly long timescale, i.e. have a noticeable effect on EET. Ref. 32 provides a possible answer, suggesting that adding *dynamic disorder* to the system, a result of bath fluctuations, can improve exciton diffusion, rather than impede it. In fact, theoretical research [33, 34] suggests the existence of a so-called 'quantum Goldilocks effect', which states that exciton diffusion is optimised where the relative strengths of the excitonic coupling, static and dynamic disorder are in the same ballpark.

A physically exact model of a light-harvesting system would consider all degrees of freedom (system *and* bath) as quantum mehanical. However, this would become computationally intractable very quickly, because the bath contains a staggeringly large number of phonon modes. Instead, a choice is usually made to work with a so-called *semi-classical method*: only a select few degrees of freedom are computed quantum mechanically, while the rest are modelled stochastically or through other means.

1.4.1 Hierarchical Equations of Motion

The Hierarchical Equations of Motion (HEOM), developed by Tanimura and Kubo [35,36] and further developed by Ishizaki and Fleming [37], are a set of non-perturbative equations that describe the dynamics of open quantum systems. Throughout this work, we will be using this method as a baseline, as it is considered a 'gold standard' in quantum dynamics.

Research has been done in comparing experimental two-dimensional electronic spectra of the FMO complex at a temperature of 150 K after a waiting time of 400 fs (Ref. 21) to those modelled with the HEOM approach (Ref. 38), from which it becomes clear that HEOM is able to predict certain features in the experimental spectra, such as the cross-peaks and excited-state absorption peak. Sadly, the correspondence between the two spectra is not perfect (their physical meanings differ), and few other studies have been done that compare HEOM-modelled spectra to experiment. The experimental and computational spectra can be compared in Fig. 1.4.

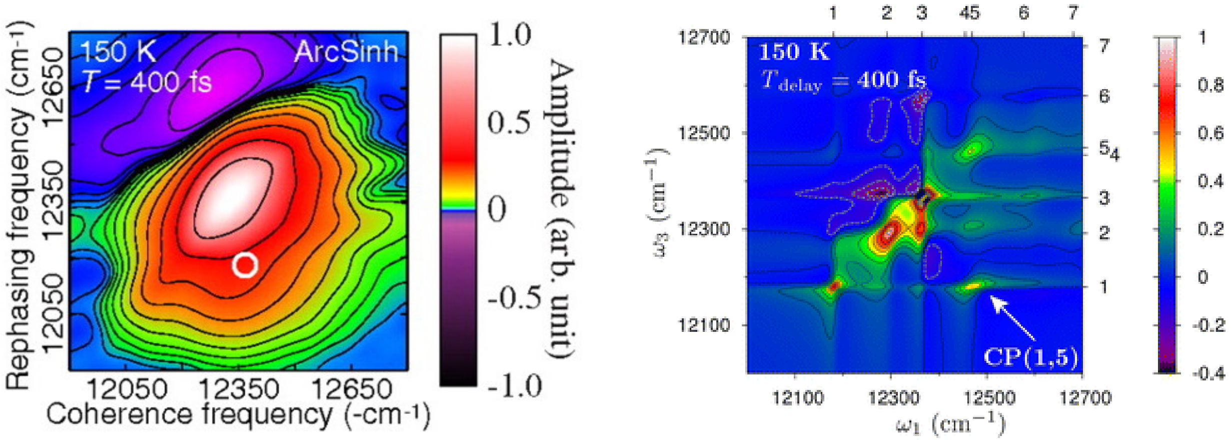

(a) The 2DES experimental data for the FMO complex. This diagram shows the sum of the rephasing and non-rephasing parts of the 2D spectrum, which is customary for most spectra. A notable feature is the purple excited-state absorption peak. Adapted with permission from Ref. 21.

(b) The HEOM-modelled data of the FMO complex. This diagram shows only the rephasing part of the optical spectra, as opposed to Fig. 1.4a. Hints of an excited state absorption peak are shown in purple. Adapted with permission from Ref. 38. © 2012, American Chemical Society.

Figure 1.4: A comparison of experimental and computational spectra. The correspondence between the two diagrams is slightly worse because Fig. 1.4b does not incorporate the non-rephasing part of the spectrum. An important feature is that there are no bleaching (positive) peaks in the upper left corner, due to correct thermalisation. A negative peak implies excited state absorption (EA), which is present in both diagrams.

1.4.2 Surface hopping

Surface hopping is a semi-classical method that considers the bath modes as living on certain potential energy surfaces (PES) associated with the electronic quanta: the *adiabatic surfaces*. At each point in time, the classical degrees of freedom 'feel' a force due to the gradient of the PES (a Hellmann-Feynman force [3,39]) and the algorithm chooses whether to perform a 'hop' between two adiabatic surfaces based on so-called *nonadiabatic couplings* that will be defined in Section A.3. An implementation that is used often is Tully's Fewest Switches Surface Hopping (FSSH) [40].

A downside of the surface hopping algorithm is that classical and quantum degrees of freedom must be propagated simultaneously, which proves computationally expensive for large systems [4].

1.4.3 Numerical Integration of the Schrödinger Equation

The Numerical Integration of the Schrödinger Equation (NISE) is a semi-classical method that treats only a few degrees of freedom quantum mechanically - those that are relevant in the Frenkel exciton model [25,42]. It computes the dynamics of the excitonic wavefunctions, which is then used to generate spectra such as in Figs. 1.4 and 1.5.

In principle, all bath coordinates are treated classically. As mentioned before in Section 1.3, these bath coordinates can be generated through elaborate MD simulations, or computed with a Brownian oscillator model. As a result, this method is stochastic. Using only a single trajectory for each bath coordinate means we are not sampling enough of its phase space, leading to wobbly population dynamics. To mitigate this, we need to take enough samples (at least 10000 is advised to smooth out the population dynamics significantly) and take the average of their population trajectories.

The method is an approximation of the Ehrenfest method, which differs from NISE in that the excitonic states give a feedback to the bath variables due to Hellmann-Feynman forces, similar to the surface hopping algorithm described in Section 1.4.2 [4].

One limitation of this method is the fact that the bath coordinates are always propagated on the PES of the electronic ground state [4]. This means that measurable effects such as the Stokes shift [43] are completely neglected.

Another very important limitation of NISE is that the Schrödinger equation contains no explicit notion of temperature - in quantum dynamics, any thermal effects come about by considering the many vibrational quanta that can couple to the excitonic ones. Reducing

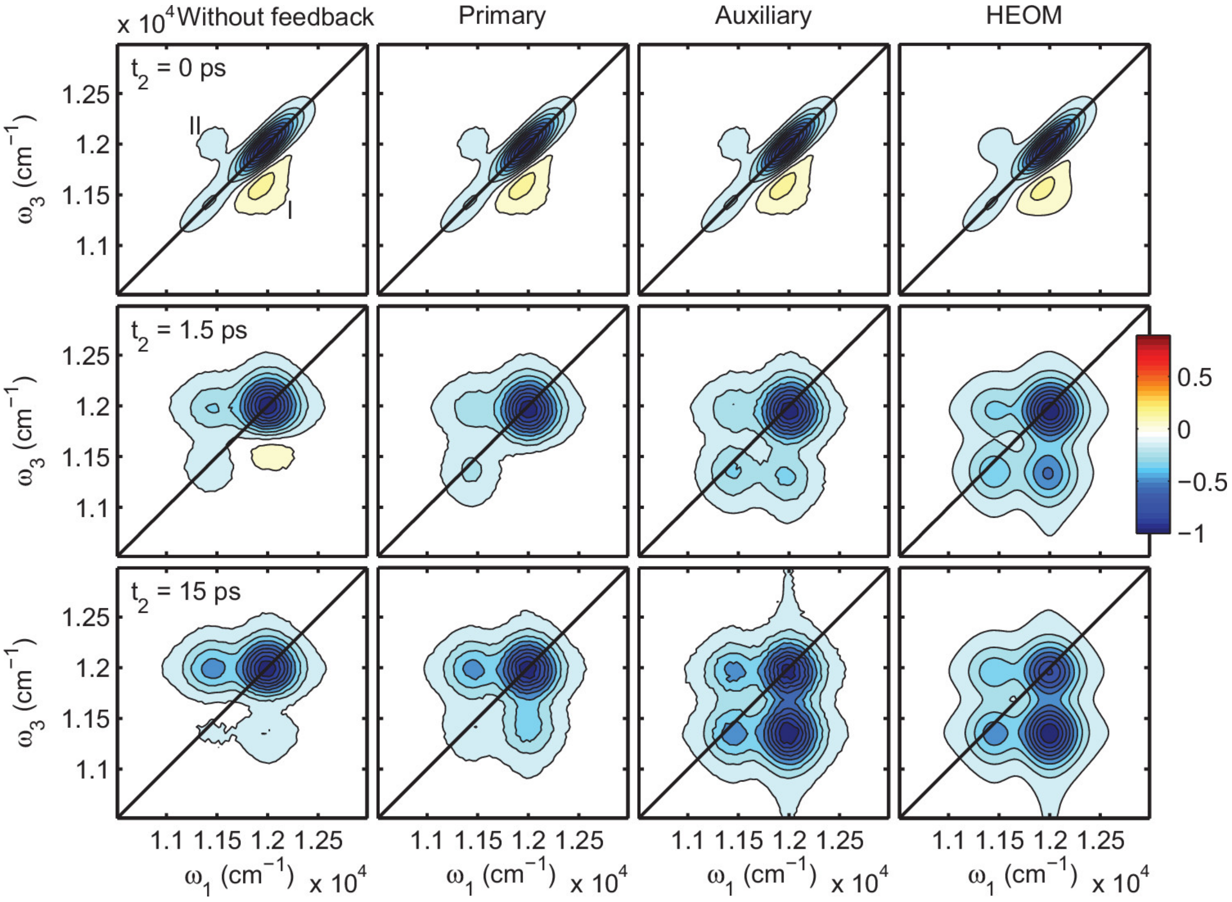

FIGURE 1.5: 2D spectra for a dimer system at waiting times of 0, 1.5 ps and 15 ps, simulated with NISE (left), surface hopping (middle columns) and HEOM (right). Surface hopping methods appear to yield the right thermalisation features, as opposed to NISE. Reprinted with permission from Ref. 41.

these vibrational quanta to classical degrees of freedom causes us to lose the thermal properties that emerge in the real world. The resulting 2D spectra simulated with NISE are compared to surface hopping and HEOM in Fig. 1.5 and to surface hopping in Fig. 1.6.

The cross-peak in the bottom right of Fig. 1.6 is highly suppressed compared to the same cross-peak as simulated by surface hopping. Such cross-peaks occur when population initially on the higher-energy excitonic states relaxes to the lower-energy excitonic states, which is a thermally favoured process. The fact that the diagonal peak in the upper right spectrum in Fig. 1.6 does not 'migrate' to a cross-peak over time indicates that population relaxation is not described correctly by NISE, i.e. the Boltzmann distribution is not reached.

A part where the computational capabilities of NISE exceed those of HEOM, is in the form of the bath potential. HEOM, and particularly the PHI implementation by Strümpfer [44] has been derived in the limit where the bath coordinates can be described as overdamped Brownian harmonic oscillators. This is a reasonable assumption if the bath fluctuations are sufficiently fast (the time-averaged phonon coordinates will follow the Gaussian distribution thanks to the *central limit theorem* [45]) but it breaks down quickly if the bath happens to be dominated by anharmonic modes. In NISE, the bath potential can take any shape, and the semi-classical Hamiltonian can be generated by a separate program, which means that it can be made through MD and electrostatic calculations. In this work, however, we will stick to generating the Hamiltonian as a overdamped Brownian oscillator, to facilitate the comparison between NISE and HEOM.

While NISE may produce computational artifacts due to bad thermalisation, its computational cheapness is a main factor for consideration. As the quantum systems we study increase in size and complexity, NISE vastly outperforms HEOM in terms of computational time [4].

1.4.4 Previously proposed solutions

The end goal of this research is to validate multiple methods of mitigating the poor thermalisation that NISE provides. A few such methods have been proposed [4, 5, 46–48].

The first of these, Ref. 4, is based on a rescaling of particular nonadiabatic transitions based on a rate equation: thermalisation is ensured by correcting the nonadiabatic couplings with a thermal correction factor. However, this method does not preserve invariant subspaces of the system's Hilbert space, and is therefore not suited to systems larger than

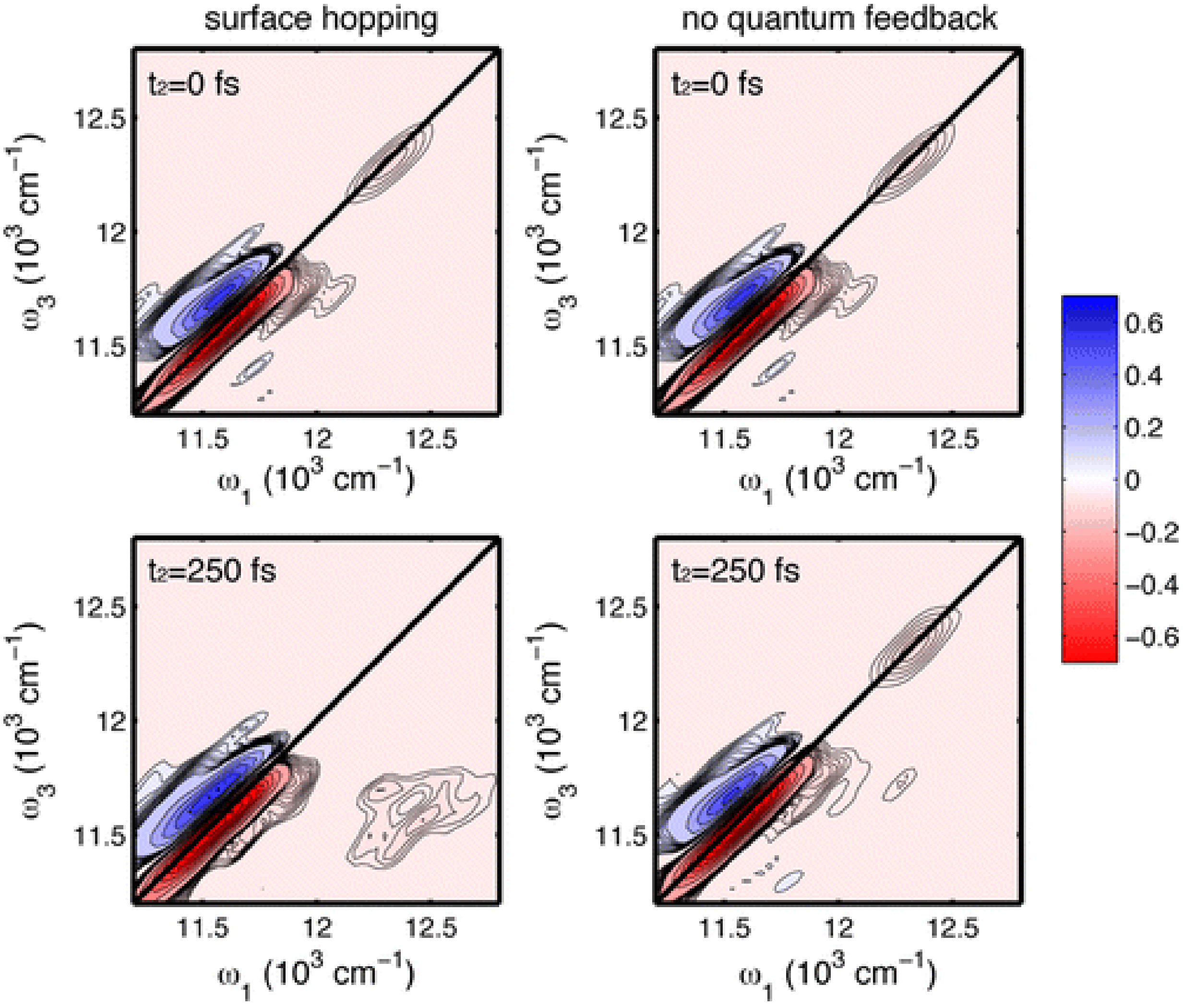

Figure 1.6: 2D spectra of the LH2 complex at waiting times 0 (top) and 250 fs (bottom) simulated with surface hopping (left) and NISE (right). Important to note is the underrepresented cross-peak in the bottom right of the spectrum in the fourth panel (bottom right) compared to that in the third (bottom left): an artifact of poor thermalisation. Reprinted with permission from Ref. 1.

2 chromophores.

The second, Ref. 5, uses a quantum correction factor derived in earlier work (Ref. 49,50) and works by correcting the perturbations in average eigenbasis (scaling down perturbations that transport population from low-energy excitonic states to high-energy excitonic states and favouring EET in the opposite direction) rather than the nonadiabatic couplings. This method still has a flaw, in that its high-temperature results do not correspond to predictions with the uncorrected method. The third, Ref. 46, corrects the nonadiabatic couplings instead. The fourth, Ref. 47, proposes a solution to the problem in Ref. 5 by introducing a wavefunction-dependent scaling in the thermal correction. Fifth, Ref. 48 provides a correction to the nonadiabatic couplings and also includes a so-called 'coherence penalty function' (CPF) that drives the density matrix away from high coherences.

1.4.5 New proposals

First of all, the proposal by Aghtar *et al.* (Ref. 47) has not been applied to the corrections to the nonadiabatic couplings in computational experiment, and doing so might help obtain computational results that are close to those predicted by HEOM. This work will add a similar wavefunction-dependent correction to this method. The method outlined in Ref. 47 will here be named NISE-DBb (NISE with detailed balance, version b), whereas the method that corrects the nonadiabatic couplings in NISE shall be named NISE-DBa (NISE with detailed balance, version a). In Refs. 5, 46 the methods of propagation are called bundle of trajectories (BT) and individual trajectory (IT), respectively.

A full comparison of NISE-DBa and NISE-DBb has not been made before. Refs. 5, 46 have compared the methods without the high-temperature adjustment proposed in Ref. 47. This work will compare the two methods to NISE and HEOM in different parameter regimes, to simulate both nature-like and artificial systems.

Lastly, populations have only been calculated in two bases: one being the local basis, in which the highest-energy chromophore is initially excited, the other being the adiabatic basis, in which the highest-energy instantaneous eigenstate is initially excited. It is difficult to interpret the results of HEOM in the adiabatic basis, since the adiabatic populations are ill-defined for that method. This is because HEOM only considers the dynamics of the complete ensemble, i.e. it does not consider individual bath trajectories. This work will thus also compare the results of different methods in the average eigenbasis, hopefully giving a more well-rounded insight into the accuracy of 2D electronic spectra generated with these methods.

1.4.6 Summary

In summary, the two methods that will be tested and compared in this work are NISE-DB, i.e. NISE with detailed balance. Both methods offer perturbative corrections to the NISE method, hoping to alleviate the problem that the latter has with thermalisation. The commonality between NISE-DBa and NISE-DBb is the fact that they treat the dynamic disorder in an open quantum system perturbatively, and that they offer a correction such that the dynamics will reach the Boltzmann distribution after sufficient time has passed. Their difference is the nature of the perturbation: NISE-DBa computes the probability of transport between adiabatic states with the derivative of the Hamiltonian or its eigenstates. NISE-DBb, on the other hand, computes the probability of transport between average eigenstates, and compares the Hamiltonian at each timestep to the 'ideal' Hamiltonian, where dynamic disorder is averaged out.

The methods will be used to compute population dynamics: the time evolution of the occupations of individual chromophores, average eigenstates or adiabatic states. The methods are designed to have similarly fast computational speeds to NISE, which is one of the fastest methods of simulating population dynamics. Next, the methods are hoped to reproduce the more accurate dynamics (especially thermalisation) as predicted by HEOM.

Chapter 2

The Schrödinger Equation and Detailed Balance

In this chapter, we will be discussing the theory that underpins this research. In the first section, we will quickly cover the NISE algorithm. The second section covers the exciton Hamiltonians used to describe EET, the different parameter regimes that come into play and the effects that they would have on our results. The third section is about the recovery of the Boltzmann distribution in quantum dynamics with a semi-classical thermal correction, both in low- and high-temperature regimes. Lastly, the fourth section is a summary of the two methods that will be tested in this work.

2.1 Quantum dynamics

To talk about waiting-time dynamics in optical spectroscopy, we need the time-dependent Schrödinger equation (TDSE) [3] given in Eq. (2.1).

$$i\hbar\frac{\partial}{\partial t}\left|\psi(t)\right\rangle = H(t)\left|\psi(t)\right\rangle \tag{2.1}$$

Indicating that the time dependence of the wavefunction $|\psi(t)\rangle$ indicating our state at a time t is given by a quantity which depends on the Hamiltonian $H(t)$. This Hamiltonian can be separated into a time-independent part, H_0, and a time-dependent part, $V(t)$. This is particularly useful for the perturbative treatment of EET.

2.1.1 Numerical Integration of the Schrödinger Equation

The method of NISE is based around the solution of the time-dependent Schrödinger equation by discrete integration, where our Hamiltonian may change at every timestep. Solving Eq. (2.1) gives us the following result:

$$|\psi(t+\mathrm{d}t)\rangle = e^{-\frac{i}{\hbar}\int\limits_{t}^{t+\mathrm{d}t} H(t')\mathrm{d}t'} |\psi(t)\rangle \tag{2.2}$$

If we go by the assumption that the Hamiltonian $H(t)$ remains roughly constant between t and $t+\mathrm{d}t$, we can take $H(t)$ out of the integral, and Eq. (2.2) is simplified to Eq. (2.3).

$$|\psi(t+\mathrm{d}t)\rangle = U(t+\mathrm{d}t, t)\,|\psi(t)\rangle = e^{-\frac{i}{\hbar}H(t)\mathrm{d}t}\,|\psi(t)\rangle \tag{2.3}$$

With $U(t+\mathrm{d}t, t)$, we indicate a unitary (probability-conserving) operator, also known as the *time-evolution operator* which takes us from our state at time t to the state at time $t+\mathrm{d}t$. If we want to calculate a complete wavefunction trajectory, we must compute the wavefunction at every timestep as follows:

$$|\psi(t_n)\rangle = \left[\prod_{k=1}^{n} U(k\mathrm{d}t, (k-1)\mathrm{d}t)\right] |\psi(0)\rangle \tag{2.4}$$

where $t_n = n\mathrm{d}t$, the nth timestep.

2.2 Exciton Hamiltonians

In principle, when describing a system that is in contact with a bath, we can consider all degrees of freedom (those of the system and bath) as quantum mechanical. This is done in some cases, for example in reduced density matrix approaches, which are capable of modelling irreversible loss of information, i.e. decoherence. In this work, however, and as is often the case, we consider the system's degrees of freedom quantum mechanically for the purposes of calculating the response functions, while the bath degrees of freedom are propagated classically.

To describe a system of multiple chromophores that can undergo EET, we will use a class of Hamiltonians given by Eq. (2.5).

$$H(t) = H_0 + V(t) \tag{2.5}$$

$$H_0 = \sum_{n=1}^{N} E_n \left|n\right\rangle \left\langle n\right| + \sum_{n\neq m} J_{nm} \left|n\right\rangle \left\langle m\right| \tag{2.6}$$

$$V(t) = \sum_{n=1}^{N} \Delta E_n(t) \left|n\right\rangle \left\langle n\right| \tag{2.7}$$

where we consider the time-dependent Hamiltonian $H(t)$ in site basis, composed of a time-independent part H_0 consisting of the average site energies E_n and the couplings J_{nm}, and a time-dependent perturbing potential $V(t)$. This is the simplification of the class of Frenkel exciton Hamiltonians [25, 42, 51], in which the system can couple to a classical electromagnetic field which can transport the system between the ground states and several excited states. Transport from the singly excited states to the doubly excited state or the ground state is assumed to be negligible: its timescales far exceed those of EET.

The individual chromophores are coupled to a bath (which can have any form, but is often approximated by a harmonic bath with no correlation between the different chromophores), which causes fluctuations $\Delta E_n(t)$ in the diagonal elements (site energies) of the Hamiltonian. In principle, it is also possible for the dipole-dipole couplings J_{nm} to fluctuate, which is due to so-called *structural disorder* [51], i.e. slight fluctuations in the relative orientation and positioning of the chromophores, however they are assumed to be constant in the present model. They can be calculated with the point dipole-dipole interaction formula

$$J = \frac{1}{4\pi\epsilon_0 r_{ij}^3}\left[\vec{\mu}_i \cdot \vec{\mu}_j - 3(\vec{\mu}_i \cdot \hat{r}_{ij})(\vec{\mu}_j \cdot \hat{r}_{ij})\right] \tag{2.8}$$

but other approaches to finding the dipole-dipole couplings exist, such as the extended dipole model [51–53] and TrEsp [53].

2.2.1 The Displaced Harmonic Oscillator Model

The collection of Hamiltonians we will be working with can be described by the displaced harmonic oscillator (DHO) model as seen in Fig. 2.1.

Let us consider the simplest system: a monomer whose electronic state is coupled to a single vibrational degree of freedom through so-called *vibronic coupling* or *system-bath coupling*. The energy of the electronic state will depend on the vibrational displacement,

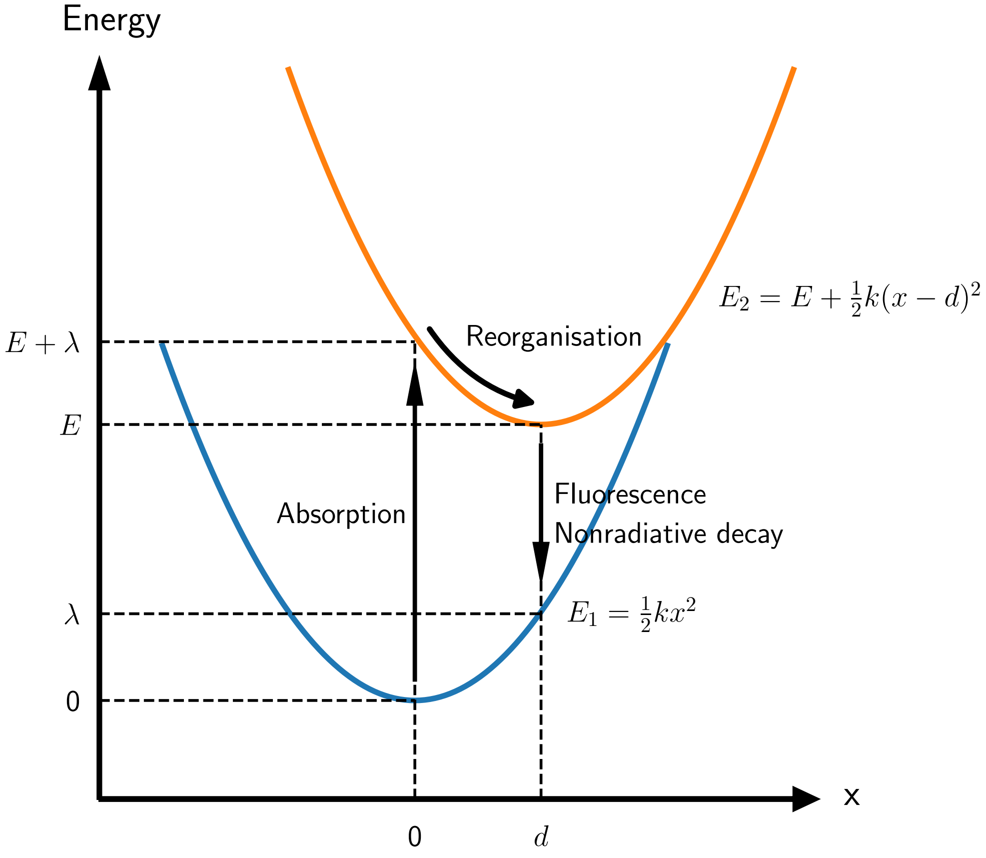

FIGURE 2.1: A graphical overview of the potential-energy surfaces (PES) of two separate electronic states. The simplification to a one-dimensional case is made by assuming each electronic state only couples to a single nuclear degree of freedom. Notice how the shift in equilibrium position, d, causes the existence of a reorganisation energy λ, and the appearance of the Stokes shift 2λ - the difference between absorption and emission spectra.

a phonon coordinate which we will call x, and we can associate a ‘spring constant’ k with this vibrational degree of freedom. As such, the energy of the lower state is given as by Eq. (2.9).

$$E_g = \frac{1}{2}kx^2 \tag{2.9}$$

The higher electronic state couples differently to the vibrational state - and we can assume that for this higher state, the equilibrium length of the vibrational degree of freedom is slightly stretched or compressed by an amount d. Additionally, there is an increase in equilibrium energy, a factor E'. As such, the energy (both by vibronic coupling and energy gap) of the excited state can be described by Eq. (2.10).

$$E_e = E' + \frac{1}{2}k(x+d)^2 = E' + \frac{1}{2}kx^2 + kdx + \frac{1}{2}kd^2 \tag{2.10}$$

Here, the assumption is made that the shape of the potential landscape does not vary widely between the energy levels, such that the spring constant k remains the same.

Since for quantum dynamics, only the difference in energy levels matters, and not the absolute value of individual energies, we can translate the levels by an amount $-\frac{1}{2}kx^2$ and be left with the energies $E_g = 0$ and $E_e = E' + \sigma x + \lambda$, where the term $\lambda = \frac{1}{2}kd^2$ is called the *reorganisation energy* and the term $\sigma x = kdx$ is an energy shift which we will call the *system-bath coupling.* We can simplify this even further by absorbing the reorganisation energy into the energy shift by saying $E = E' + \lambda$, leaving us with $E_e = E + \sigma x$.

A surprising result of the existence of the reorganisation energy, though not one we will discuss in much detail, is the *Stokes shift*: the absorption peaks of this model will occur at higher energies than the emission peaks, which can be used to determine vibrational levels with fluorescence spectroscopy.

Now that we understand the working of the displaced harmonic oscillator model in the case of a monomer, we can start applying it to a dimer of two-level systems, and extrapolate the behaviour for larger systems. Each of the two-level systems given by $E_g^{(i)} = 0$ and $E_e^{(i)} = E^{(i)} + \sigma^{(i)}x_i$, for $i = 1, 2$. The total Hamiltonian for this dimer of two-level systems is given by

$$H(t) = \begin{pmatrix} E_1 + \sigma_1 x_1(t) & J \\ J & E_2 + \sigma_2 x_2(t) \end{pmatrix} \tag{2.11}$$

where J, the coupling, is determined from either the dipole-dipole coupling in the point dipole approximation, extended dipole approximation, but can also include higher-order terms such as the quadrupole coupling.

Simplifying the Hamiltonian, we sometimes translate the diagonal components by an amount $-E_2$, an action which leaves the eigenvectors of the matrix intact but simplifies the model Hamiltonian. Additionally, it is assumed that $\sigma_1 = \sigma_2 = \sigma$ (which is reasonable if the chromophores all have similar vibronic couplings).

$$H(t) = \begin{pmatrix} \Delta_E + \sigma x_1(t) & J \\ J & \sigma x_2(t) \end{pmatrix} \tag{2.12}$$

where $\Delta_E = E_1 - E_2$, called the *energy gap* or *static disorder*.

Relating λ and σ

The bath energy fluctuations are defined as $\sigma x(t) = kdx(t)$, and the reorganisation energy is $\lambda = \frac{1}{2}kd^2$. This can be used to relate σ and λ.

$$\langle(\sigma x(t))^2\rangle = \sigma^2 \langle x(t)^2\rangle = k^2d^2 \langle x(t)^2\rangle = 2\lambda k \langle x(t)^2\rangle \tag{2.13}$$

Now, using the equipartition theorem (Ref. 54), we can equate $\frac{1}{2}k\langle x^2\rangle$ to $\frac{1}{2}k_BT$, yielding:

$$\sigma^2 = 2\lambda k_B T \tag{2.14}$$

This means that the fluctuations in site energies are closely related to the reorganisation energy and the temperature.

2.2.2 Overdamped Brownian oscillators and the Langevin equation

To find the entries of the time-dependent Hamiltonian, we must still find the bath coordinates. There are many ways to do this, among which molecular dynamics (MD) simulations, but for our purposes, we find that making the assumption that they are overdamped Brownian oscillators and thus follow the Langevin equation is a suitable answer.

The bath coordinates $x_i(t)$ are also known as the 'nuclear degrees of freedom'. They can be considered as the lengths of particular phonon modes in a molecule, or (for a simplified explanation) the internuclear distance in a homonuclear diatomic molecule. In many cases, there is a single 'effective' phonon mode which dominates the system-bath interaction, turning the vibronic coupling into a one-dimensional problem. Let us model this primary mode as a particle subject to three forces: a damping force $-\gamma v(t)$ causing it to slow down, a restoring force $-kx(t)$ bringing it back to equilibrium and a random force

$f(t)$ due to interactions with the surrounding bath molecules. This yields the differential equation:

$$m\ddot{x}(t) = -\gamma\dot{x}(t) - kx(t) + f(t) \tag{2.15}$$

where we can divide by m and assume that the damping force is much greater than the restoring force (i.e. the *overdamped limit*) to find

$$\dot{v}(t) = -\frac{\gamma}{m}v(t) + \xi(t) \tag{2.16}$$

This is called the *Langevin equation* [55], whose analytical solution is also covered in Section A.1.

Numerical solution

If we want to solve for the motion of the Brownian oscillator numerically, we can transform the Langevin equation into a differential equation for the position variable to find [56]

$$x(t + \Delta t) = x(t) - \gamma x(t)\Delta t + \sqrt{2\gamma\Delta t}\mathcal{N}(0,\, 1) \tag{2.17}$$

where $\mathcal{N}(0,\, 1)$ is a number drawn from the standard normal distribution, and Δt is assumed to be infinitesimally small. Fig. 2.2 shows a number of trajectories generated in this way.

Autocorrelation functions

In order for the bath trajectories to be suitable for the quantum dynamical simulations done in this work, they must fulfil a few basic needs.

1. $\langle x(t)\rangle = 0$, i.e. they must have zero mean.
2. $C_{xx}(t) = \langle x(t)x(0)\rangle = e^{-\gamma t}$, i.e. their autocorrelation functions (ACF) must decay exponentially, starting with a variance of 1. Note that m is taken to be unity.

We can calculate the ACF using the Wiener-Khinchin theorem, as explained in Ref. 57. In Fig. 2.3, we can see the result of doing this for arbitrary γ. To calculate the ACF, one should keep in mind to generate a sufficiently long bath trajectory, as sampling errors increase with increasing time, given a finite bath trajectory. In the present case, the ACF is shown for a very small fraction of the total bath trajectory, about $4 \cdot 10^{-4}$.

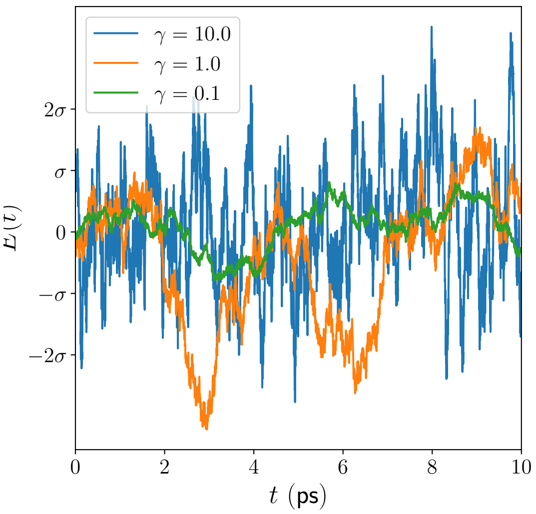

FIGURE 2.2: The behaviour of three overdamped harmonic Brownian oscillators. Note that the size and speed of fluctuations increases with γ, which is a result of the fluctuation-dissipation theorem. The timesteps are $\Delta t = 1\text{fs}$.

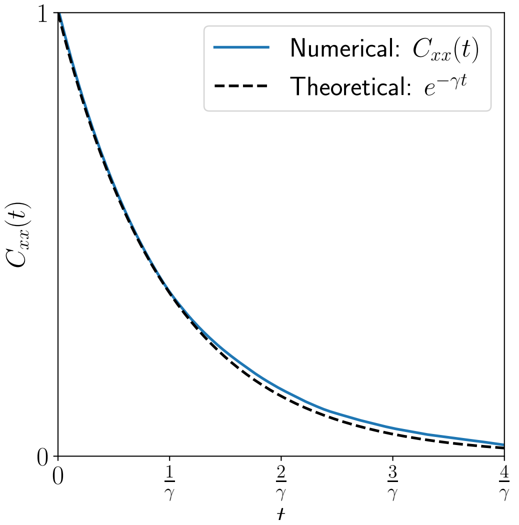

FIGURE 2.3: Predicted and calculated autocorrelation function $C_{xx}(t)$ for the Brownian overdamped harmonic oscillator as governed by Eq. (2.17) and shown in Fig. 2.2. The parameter γ is taken to be arbitrary. Only a small fraction $(4 \cdot 10^{-4})$ of the total trajectory is shown, as this allows errors to be averaged out more easily.

2.2.3 Energy levels and parameter regimes of a dimer

A dimer of two-level systems has the following Hamiltonian in site basis, when considering only the singly-excited states to be accessible:

$$\begin{pmatrix} \Delta_E & J \\ J & 0 \end{pmatrix} \tag{2.18}$$

An excitation, if present on the first molecule (corresponding to our system being in state $|\psi_1\rangle$), can hop over to the other molecule (the system being in state $|\psi_2\rangle$) with a particular probability which depends on the relative magnitude of Δ_E and J. $|\psi_1\rangle$ and $|\psi_2\rangle$ are defined as:

$$|\psi_1\rangle = \begin{pmatrix} 1 \\ 0 \end{pmatrix}, \qquad |\psi_2\rangle = \begin{pmatrix} 0 \\ 1 \end{pmatrix} \tag{2.19}$$

Decomposition in eigenbasis

If we are to consider the time evolution of this dimer system, we must identify the stationary states, which are the eigenstates which remain invariant up to a complex phase upon interaction with the time evolution operator $U(t + \mathrm{d}t, t) = e^{-\frac{i}{\hbar}H(t)\mathrm{d}t}$ (i.e. the *eigenstates*). The eigendecomposition of H includes its eigenvalues:

$$\epsilon_\pm = \frac{\Delta_E}{2} \pm \sqrt{\left(\frac{\Delta_E}{2}\right)^2 + J^2} \tag{2.20}$$

and their corresponding (normalised) eigenvectors:

$$|\psi_+\rangle = \sqrt{\frac{1}{2 + 2\left(\frac{\Delta_E}{2J}\right)^2 + \frac{\Delta_E}{J}\sqrt{\left(\frac{\Delta_E}{2J}\right)^2 + 1}}} \begin{pmatrix} \frac{\Delta_E}{2J} + \sqrt{\left(\frac{\Delta_E}{2J}\right)^2 + 1} \\ 1 \end{pmatrix} \tag{2.21}$$

$$|\psi_-\rangle = \sqrt{\frac{1}{2 + 2\left(\frac{\Delta_E}{2J}\right)^2 - \frac{\Delta_E}{J}\sqrt{\left(\frac{\Delta_E}{2J}\right)^2 + 1}}} \begin{pmatrix} \frac{\Delta_E}{2J} - \sqrt{\left(\frac{\Delta_E}{2J}\right)^2 + 1} \\ 1 \end{pmatrix} \tag{2.22}$$

The resulting energy levels, and how well the eigenstates correspond to the local basis states, can be seen in Fig. 2.4.

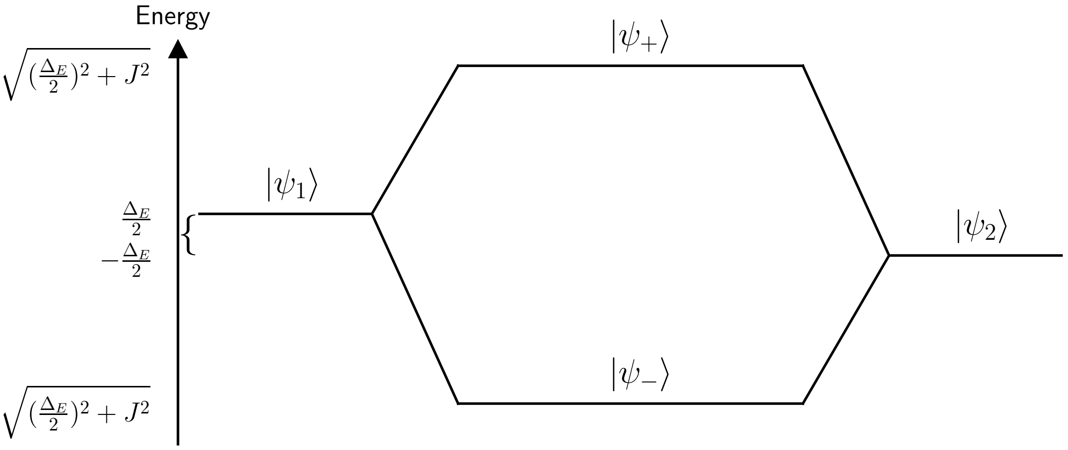

FIGURE 2.4: The splitting of states $|\psi_1\rangle$ and $|\psi_2\rangle$ in site basis, into eigenstates $|\psi_\pm\rangle$. One can see that the overlaps $\langle\psi_+|\psi_1\rangle$ and $\langle\psi_-|\psi_2\rangle$ should be slightly larger than $\langle\psi_+|\psi_2\rangle$ and $\langle\psi_-|\psi_1\rangle$. However, since J appears larger than Δ_E, the system is rather delocalised.

$\Delta_E \ll J$, the delocalised case

We can also look at the other extreme case, where the difference between site energies is negligible with respect to the coupling. We can see that exciton transport between the two sites is at its largest, and in fact, when starting out with a full population on site 1, after a time $\frac{J}{\hbar}$ we will find the full population on site 2. When taking the limit as $\frac{\Delta_E}{J}$ goes to zero, we can see that our eigenvalues and eigenvectors will become:

$$\epsilon_\pm = \pm J \tag{2.23}$$

$$|\psi_+\rangle = \frac{1}{\sqrt{2}}\begin{pmatrix}1\\1\end{pmatrix}, \qquad |\psi_-\rangle = \frac{1}{\sqrt{2}}\begin{pmatrix}-1\\1\end{pmatrix} \tag{2.24}$$

This means that our exciton system is fully delocalised, and a population starting fully on site 1 will, after a time $\frac{\hbar}{4J}$ be completely on site 2, as shown in Fig. 2.5.

$\Delta_E \gg J$, the localised case

In the case that the energy levels are far apart, very little transport will occur between them. An excitation on molecule 1 will remain there with large probability. Indeed, if we

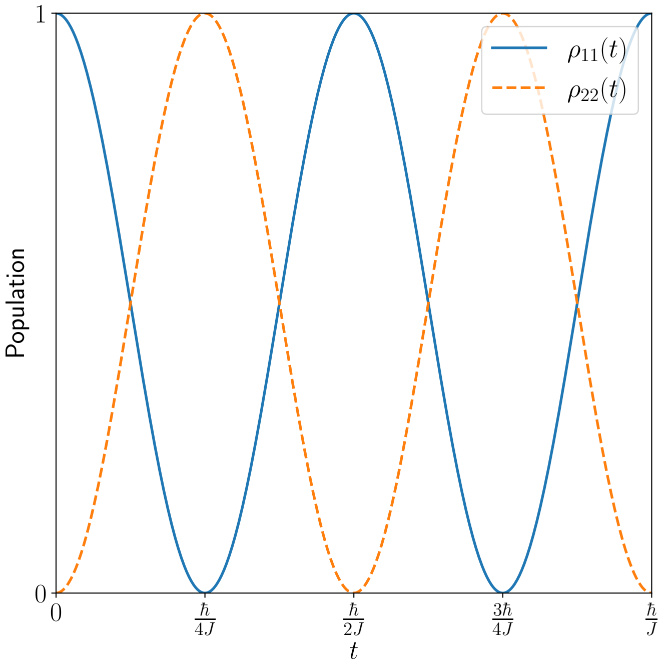

FIGURE 2.5: The population dynamics in the case where $J >> \Delta_E$. Notice that a population that starts out completely on site 1 will result in a system which is fully on site 2 after a time $\frac{\hbar}{4J}$, and that the dynamics are periodic, with a period of $T = \frac{\hbar}{2J}$.

take the limit as $\frac{J}{\Delta_E}$ goes to zero, we are left with the eigenvalues and eigenvectors:

$$\epsilon_+ = \Delta_E = E_1, \qquad \epsilon_- = 0 = E_2 \tag{2.25}$$

$$|\psi_+\rangle = \begin{pmatrix} 1 \\ 0 \end{pmatrix}, \qquad |\psi_-\rangle = \begin{pmatrix} 0 \\ 1 \end{pmatrix} \tag{2.26}$$

The stationary states overlap completely with the states in site basis, which implies that the exciton system is fully localised: no transport happens between the states. If we instead consider J to be perturbatively small, we can find the amplitude of oscillation in site basis populations. Expanding Eq. (2.20), (2.21) and (2.22) considering $\frac{J}{\Delta_E} \ll 1$, we can use the binomial approximation $(1+x)^n \approx 1 + nx$ to find the perturbed eigenvalues and eigenvectors.

$$\sqrt{\left(\frac{\Delta_E}{2J}\right)^2 + 1} = \frac{\Delta_E}{2J}\sqrt{1 + \left(\frac{2J}{\Delta_E}\right)^2} \approx \frac{\Delta_E}{2J}\left[1 + \frac{1}{2}\left(\frac{2J}{\Delta_E}\right)^2\right] = \frac{\Delta_E}{2J} + \frac{J}{\Delta_E} \tag{2.27}$$

This means that the perturbed eigenvalues are:

$$\epsilon_\pm = \begin{cases} \frac{\Delta_E}{2}\left[2 + \frac{1}{2}\left(\frac{2J}{\Delta_E}\right)^2\right] = \Delta_E + \frac{J^2}{\Delta_E} \\ \frac{\Delta_E}{2} \cdot -\frac{1}{2}\left(\frac{2J}{\Delta_E}\right)^2 = -\frac{J^2}{\Delta_E} \end{cases} \tag{2.28}$$

The (unnormalised) eigenvectors are then given by:

$$|\psi_+\rangle = \begin{pmatrix} \frac{\Delta_E}{2J}\left[2 + \frac{1}{2}\left(\frac{2J}{\Delta_E}\right)^2\right] \\ 1 \end{pmatrix} = \begin{pmatrix} \frac{\Delta_E}{J} + \frac{J}{\Delta_E} \\ 1 \end{pmatrix} \overset{norm.}{\approx} \frac{1}{\sqrt{1 + \left(\frac{J}{\Delta_E}\right)^2}} \begin{pmatrix} 1 \\ \frac{J}{\Delta_E} \end{pmatrix} \tag{2.29}$$

$$|\psi_-\rangle = \begin{pmatrix} \frac{\Delta_E}{2J}\left[1 - 1 - \frac{1}{2}\left(\frac{2J}{\Delta_E}\right)^2\right] \\ 1 \end{pmatrix} \overset{norm.}{\approx} \frac{1}{\sqrt{1 + \left(\frac{J}{\Delta_E}\right)^2}} \begin{pmatrix} -\frac{J}{\Delta_E} \\ 1 \end{pmatrix} \tag{2.30}$$

Let's write down a trial wavefunction and its time evolution:

$$|\psi(t)\rangle = \tilde{c}_1 e^{-\frac{i}{\hbar}(\Delta_E + \frac{J^2}{\Delta_E})t} \begin{pmatrix} 1 \\ \frac{J}{\Delta_E} \end{pmatrix} + \tilde{c}_2 e^{\frac{i}{\hbar}\frac{J^2}{\Delta_E}t} \begin{pmatrix} -\frac{J}{\Delta_E} \\ 1 \end{pmatrix} \tag{2.31}$$

Where $\tilde{c}_1$ and $\tilde{c}_2$ are the wavefunction coeffients of the eigenstates. If we assume them to be constant over time, and if we have all our population on the first site, we can set the total coefficient of site 2 to zero at $t = 0$, which means that $\tilde{c}_2 = -\frac{J}{\Delta_E}\tilde{c}_1$. Finding the approximate time-dependent population on site 2 is then an easy task: it is given by

$$\rho_{22}(t) = \left(\frac{J}{\Delta_E}\right)^2 \sin^2 \frac{\Delta_E t}{2\hbar} \tag{2.32}$$

An example of this can be seen in Fig. 2.6.

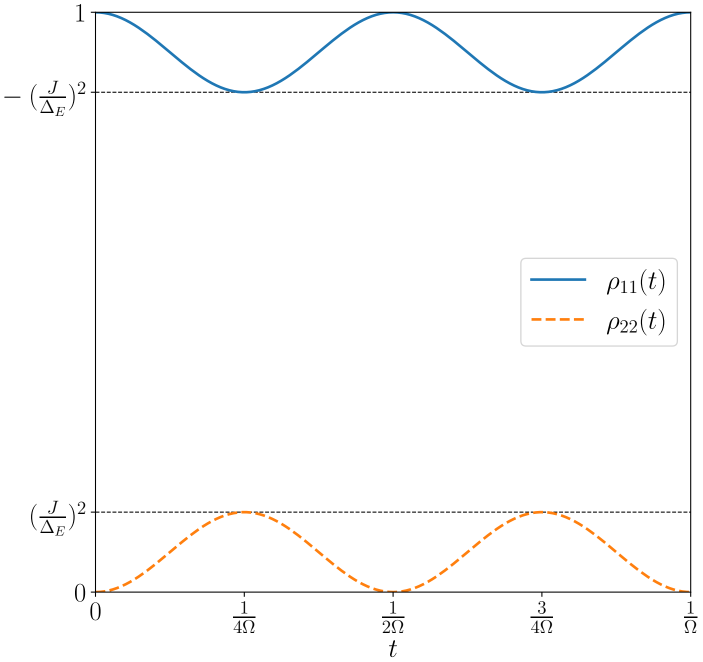

FIGURE 2.6: Population dynamics in the case where $\Delta_E >> J$. The population fluctuations are exaggerated for purposes of clarity. Note that the dynamics are periodic, with a period of $T = \frac{1}{2\Omega}$, where $\Omega = \sqrt{\left(\frac{\Delta_E}{2}\right)^2 + J^2}$. The amplitude of these oscillations is $\frac{1}{2}\left(\frac{J}{\Delta_E}\right)^2$.

Large dynamic disorder causes localisation

One can add an additional term to the Hamiltonian: a time-dependent potential which is generated by some additional interaction with the environment (usually with a solvent). This is called *dynamic disorder* [34]. Let us consider this potential to fluctuate quickly compared to the dynamics of our excitonic system without the presence of such fluctuations. Our Hamiltonian now looks as follows:

$$H(t) = \begin{pmatrix} \sigma x_1(t) & J \\ J & \sigma x_2(t) \end{pmatrix} \tag{2.33}$$

To decide whether an excitonic system is localised or delocalised, we must compare the size of the dynamic disorder to the excitonic coupling. The small-fluctuation regime is quite easy to treat perturbatively: there will be very little effect on transport, similar to when the static disorder is small. Instead, let us look at the case where $\sigma \gg J$, i.e. the dynamic disorder is large. The time-averaged expectation value of the energy difference is given as:

$$\langle E_1(t) - E_2(t) \rangle = \sigma \langle x_1(t) - x_2(t) \rangle = \sigma(\langle x_1(t) \rangle - \langle x_2(t) \rangle) = 0 \tag{2.34}$$

This expectation value might be zero, but we can still look at the mean squared difference, which can tell us a little bit more.

$$\begin{aligned}
\langle (E_1(t) - E_2(t))^2 \rangle &= \sigma^2 \big[\langle x_1(t)^2 \rangle + \langle x_2(t)^2 \rangle - 2 \langle x_1(t) x_2(t) \rangle \big] && (2.35)\\
&= \sigma^2 \big[\langle x_1(t)^2 \rangle + \langle x_2(t)^2 \rangle - 2 \langle x_1(t) \rangle \langle x_2(t) \rangle \big] && (2.36)\\
&= \sigma^2 \big[\langle x_1(t)^2 \rangle + \langle x_2(t)^2 \rangle \big] && (2.37)\\
&= 2\sigma^2 && (2.38)
\end{aligned}$$

The mean squared difference in site energies is large, therefore it must be sampled from a wide Gaussian distribution. This means that the energy difference between sites is likely to be much larger than J. We can safely say that a large dynamic disorder causes exciton localisation.

Dynamic disorder causes decoherence

We know that the cause of dynamic disorder is the bath coupling. In the present model, there is one effective phonon mode coupled to each chromophore. These phonons are considered overdamped Brownian harmonic oscillators as in Section 2.2.2.

When integrating the Schrödinger equation with a Hamiltonian whose diagonal elements are given by such Brownian oscillators, we are using a single trajectory which constitutes only a small amount of the microstates that our bath can occupy. When dealing with a bath, knowing only its macrostate, we must sum over as large a number of microstates as possible (i.e. we must sample all or most of its phase space). One does this by generating a large amount of Hamiltonian trajectories, integrating the Schrödinger equation and averaging all of the resulting population trajectories. The system will decohere and no longer be in a pure superposition of states. The populations will relax to their equilibrium values (which, in the case of N states in the NISE formalism, is $\rho_{nn} = \frac{1}{N}$ for all values of n: a uniform distribution). Applying more exact methods such as HEOM, the Boltzmann populations will be recovered at large timescales.

The dynamic disorder parameter influences the behaviour of the system. To distinguish between different disorder regimes, a parameter $\kappa = \frac{\gamma}{\sigma}$ is defined which characterises the speed of the bath dynamics [17].

Fast modulation limit

$\kappa \gg 1$ tells us that bath dynamics are fast, and that the energy fluctuations are uncorrelated between different timesteps (see Eq. (2.39)). The correlation function is given as:

$$C(t) = \langle \Delta_{E,n}(t)\Delta_{E,m}(t) \rangle = \frac{\sigma^2}{\gamma}\delta(t)\delta_{nm} = \Gamma\delta(t)\delta_{nm} \tag{2.39}$$

where Γ is called the *inhomogeneous linewidth* [17], In this case, the Haken-Strobén-Reineker (HSR) model describes the system well [58]. The density matrix elements evolve in Liouville space as follows:

$$\frac{\mathrm{d}}{\mathrm{d}t}\rho_{nm} = -\frac{i}{\hbar}[H_0, \rho]_{nm} - 2\Gamma(1 - \delta_{nm})\rho_{nm}(t) \tag{2.40}$$

Slow modulation limit or static limit

$\kappa \ll 1$ means bath dynamics are slow. Instead of generating a bath trajectory, one can get away with generating a single bath coordinate. This simplifies the solution of the Schrödinger equation, as the same time-evolution operator applies throughout the integration. Averaging over the bath needs to be done in the same fashion as before.

The effects of fluctuation speed on observables

In spectroscopic experiments, we cannot detect quantities such as populations and coherences. Instead, we must look at *observables*. These are usually the energies in our spectra. Given a simple dimer of two-level systems, the peak energies in the spectrum are usually not equal to the fluctuating site energies. Instead, the energies are eigenvalues of the Hamiltonian which has been averaged over the time that the light interacts with our system. Therefore, if we wish to accurately predict observables, we must look at the average eigenbasis and adiabatic basis.

In the fast-modulation limit, the interaction time is much longer than the time of fluctuation $\frac{1}{\gamma}$, and our Hamiltonian can be represented by its long-term average, which means our energies are given by the average eigenvalues. In the static limit, the fluctuation timescale is much longer than the interaction time, and therefore our system's energies are best represented by the instantaneous eigenvalues of the Hamiltonian, and our observables are best regarded in the adiabatic basis.

2.3 Detailed balance

As we have seen from the population dynamics in 2.2.3, the populations are not guaranteed to reach the Boltzmann distribution as expected from systems in thermal equilibrium with the bath. We must first identify the reason for this, and come up with a physically acceptable solution.

2.3.1 Perturbation theory

The detailed balance methods proposed in Refs. [5, 46–48] rely on time-dependent perturbation theory. Therefore, it is useful to look at two different definitions of the perturbation, which in turn inform two different detailed balance methods, NISE-DBa and NISE-DBb.

Perturbation from the average Hamiltonian

The first of these methods, which will become NISE-DBb, considers a Hamiltonian defined as follows:

$$H(t) = H_0 + V(t) \tag{2.41}$$

where H_0 is the average Hamiltonian, and $V(t)$ contains the energetic disorder, which is considered the perturbation. For reasons that will become clear shortly, this perturbation needs to be considered in average eigenbasis. The Hamiltonian will be transformed from local basis to average eigenbasis as follows:

$$H_{\mathrm{a}}(t) = CH_0C^\dagger + CV(t)C^\dagger \tag{2.42}$$

where $CH_0C^\dagger$ is a diagonal matrix whose entries are the eigenvalues of the average Hamiltonian. The C matrix contains the average eigenvectors as row vectors (not to be confused with the autocorrelation function) and $C^\dagger$ is its hermitean conjugate. $CV(t)C^\dagger$ is the projection of the dynamic disorder onto the average eigenbasis. Its off-diagonal entries, by Fermi's Golden Rule, determine the transition rate between two states in average eigenbasis. They are also the ones that need to be adjusted for detailed balance.

Perturbations in the adiabatic basis

The second method, which will become NISE-DBa, considers the Hamiltonian and perturbation to be defined in a slightly different way: via the nonadiabatic couplings. First of all, this requires an explanation of the adiabatic basis. Using the derivation in Section A.3, we find that the time evolution is given by

$$|\psi(t+\Delta t)\rangle_{\mathrm{ad}} = e^{-\frac{i}{\hbar}P(t)\Delta t}\,|\psi(t)\rangle_{\mathrm{ad}} \tag{2.43}$$

where $P_{mn}(t) = \epsilon_m(t)\delta_{mn} + i\hbar S_{mn}(t)$. Assuming that the nonadiabatic couplings $S_{mn}(t)$ are small, we can approximate $[\epsilon(t), S(t)]$ to be zero (where $\epsilon_{mn}(t) = \epsilon_m(t)\delta_{mn}$, the diagonal matrix of instantaneous energies), which lets us rewrite the above equation to

$$|\psi(t+\Delta t)\rangle_{\mathrm{ad}} = e^{-\frac{i}{\hbar}\epsilon(t)\Delta t}e^{S(t)\Delta t}\,|\psi(t)\rangle_{\mathrm{ad}} \tag{2.44}$$

where the nonadiabatic couplings are defined as:

$$S_{mn}(t) = \langle\dot{\tilde{\psi}}_m(t)|\tilde{\psi}_n(t)\rangle \tag{2.45}$$

Given that $C(t)$ is a matrix containing the adiabatic basis vectors as its columns, this means

$$e^{S(t)\Delta t} = e^{(C^\dagger(t+\Delta t) - C^\dagger(t))C(t)} \tag{2.46}$$

where we have used the definition

$$\dot{C}(t) = \lim_{\Delta t\to 0}\frac{C(t+\Delta t) - C(t)}{\Delta t} \tag{2.47}$$

2.3.2 Rate equations

Let us consider Fermi's Golden Rule as given in Eq. (A.23), which states that the rate of transfer between two states is proportional to $|V(t)|^2$, the absolute value squared of the perturbing potential, or to $|S(t)|^2$, the absolute value squared of the nonadiabatic coupling, as explored in A.3.2. Hermiticity of the perturbing potential (or antisymmetry of the nonadiabatic couplings) tells us that $k_{m\longleftarrow n} = k_{n\longleftarrow m}$, as dictated by the rate equation:

$$\frac{\partial \rho_n}{\partial t} = k_{n\longleftarrow m}\rho_m - k_{m\longleftarrow n}\rho_n \tag{2.48}$$

The rate equation is the differential equation that governs the time evolution of the populations. $k_{0\longleftarrow 1}$ tells us the rate at which population in state 1 will transfer to state 0, and $k_{1\longleftarrow 0}$ tells us the rate of the inverse process. The equilibrium of the system governed by Eq. (2.48) is found at $k_{n\longleftarrow m}\rho_n = k_{m\longleftarrow n}\rho_m$, or $\rho_m = \rho_n$, as the net population transfer rate is zero. Here, densities with single indices imply the diagonal elements $\rho_n = \rho_{nn}(t)$.

Evidently, this perturbative formalism does not contain any explicit temperature dependence. In fact, quantum mechanics as described in such a fashion is completely insensitive to any classical notion of temperature, and any transition probabilities that follow from Fermi's Golden Rule are not automatically subject to the Boltzmann equilibrium as given by

$$\frac{\rho_n}{\rho_m} = e^{-\beta E_{nm}} \tag{2.49}$$

where $E_{nm} = E_n - E_m$ and $\beta = \frac{1}{k_B T}$. Our task is to find a correction to the dynamics as given by the Schrödinger equation that will yield the proper Boltzmann populations.

2.3.3 Population dynamics of a two-level system

Let us consider a two-level system whose populations dynamics are governed by the differential equation Eq. (2.48), so that we can derive its behaviour by solving the system of coupled equations.

$$\dot{\rho}_0(t) = -k_{1\longleftarrow 0}\rho_0(t) + k_{0\longleftarrow 1}\rho_1(t) \tag{2.50}$$

$$\dot{\rho}_1(t) = -k_{0\longleftarrow 1}\rho_1(t) + k_{1\longleftarrow 0}\rho_0(t) \tag{2.51}$$

Taking the time derivative of the first of these equations, and subsequently substituting the values of $\dot{\rho}_1(t)$ and $\rho_1(t)$ that we get from these equations, we come to the following conclusion:

$$\begin{aligned}
\ddot{\rho}_0(t) &= -k_{1\leftarrow 0}\dot{\rho}_0(t) + k_{0\leftarrow 1}\dot{\rho}_1(t) && (2.52)\\
&= -k_{1\leftarrow 0}\dot{\rho}_0(t) + k_{0\leftarrow 1}(-k_{0\leftarrow 1}\rho_1(t) + k_{1\leftarrow 0}\rho_0(t)) && (2.53)\\
&= -k_{1\leftarrow 0}\dot{\rho}_0(t) + k_{0\leftarrow 1}(-\dot{\rho}_0(t) - k_{1\leftarrow 0}\rho_0(t) + k_{1\leftarrow 0}\rho_0(t)) && (2.54)\\
&= -(k_{1\leftarrow 0} + k_{0\leftarrow 1})\dot{\rho}_0(t) && (2.55)
\end{aligned}$$

Performing a double integration yields the following results:

$$\begin{aligned}
\ln\frac{\dot{\rho}_0(t)}{\dot{\rho}_0(0)} &= -(k_{0\leftarrow 1} + k_{1\leftarrow 0})t && (2.56)\\
\dot{\rho}_0(t) &= e^{-(k_{0\leftarrow 1}+k_{1\leftarrow 0})t}\dot{\rho}_0(0) && (2.57)\\
\rho_0(t) &= \rho_0(0) + \dot{\rho}_0(0)\frac{1-e^{-(k_{0\leftarrow 1}+k_{1\leftarrow 0})t}}{k_{0\leftarrow 1}+k_{1\leftarrow 0}} && (2.58)
\end{aligned}$$

Filling in the conditions $\rho_0(0) = 1$, $\rho_1(0) = 0$, and as a result $\dot{\rho}_0(0) = -k_{1\leftarrow 0}$, we get the result

$$\rho_0(t) = \frac{k_{0\leftarrow 1} + k_{1\leftarrow 0}e^{-(k_{0\leftarrow 1}+k_{1\leftarrow 0})t}}{k_{0\leftarrow 1}+k_{1\leftarrow 0}} \tag{2.59}$$

Here, we can define a relaxation timescale $T_1 = (k_{0\leftarrow 1} + k_{1\leftarrow 0})^{-1}$.

2.3.4 A thermal correction to the population dynamics

One can deduce from Eq. (2.59) that a two-level system will relax to uniform population distribution since $k_{0\leftarrow 1} = k_{1\leftarrow 0}$. This is, unfortunately, not always equal to the Boltzmann distribution. In literature, multiple ways are defined of adjusting the rate constants, in order to recover detailed balance. The most important of these is a result of Oxtoby [49], Bader and Berne [50], which works by finding approximations to the quantum time-correlation functions by using the classical correlation functions related to the time-dependent perturbations. We will now discuss a heuristic derivation of this result, which goes as follows.

In order to satisfy detailed balance, we must have the following relation between the rate constants:

$$k_{m\leftarrow n} = e^{-\beta\hbar\omega_{mn}}k_{n\leftarrow m} \tag{2.60}$$

That is, population transfer from state n to state m must be suppressed by a factor $e^{-\beta\hbar\omega_{mn}}$ as compared to the inverse process. We can come up with a simple modification to the classical rate constants, which goes as follows. Assuming $\omega_{mn} \leq 0$, we can say

$$k^{\text{tc}}_{m\leftarrow n} = e^{-\frac{1}{2}\beta\hbar\omega_{mn}} k_{m\leftarrow n} \tag{2.61}$$

We can see that these new rate constants obey detailed balance. However, we would prefer the relaxation timescale T_1 not to be affected by such thermal corrections on the grounds that the capacity of the bath to absorb heat from our system does not depend on the dynamics of the system. The ratio of the relaxation timescales is

$$\frac{T_1^{\text{tc}}}{T_1} = \frac{k_{n\leftarrow m} + k_{m\leftarrow n}}{k_{n\leftarrow m} e^{\frac{1}{2}\beta\hbar\omega_{mn}} + k_{m\leftarrow n} e^{-\frac{1}{2}\beta\hbar\omega_{mn}}} = \frac{2}{1+e^{-\beta\hbar\omega_{mn}}} e^{-\frac{1}{2}\beta\hbar\omega_{mn}} \tag{2.62}$$

As such, we can introduce an additional factor $\frac{2}{1+e^{-\beta\hbar\omega_{mn}}} e^{-\frac{1}{2}\beta\hbar\omega_{mn}}$ to our thermally adjusted rate constants and get

$$k^{\text{tc}}_{m\leftarrow n} = e^{-\beta\hbar\omega_{mn}} \frac{2}{1+e^{-\beta\hbar\omega_{mn}}} k_{m\leftarrow n} = \frac{2}{1+e^{\beta\hbar\omega_{mn}}} k_{m\leftarrow n} \tag{2.63}$$

which agrees with Refs. [49, 50], who used it to describe vibrational energy relaxation (VER) in liquids. This correction is often quoted as the *standard* (thermal) *correction.* We could now decide to use equation Eq. (2.64) to modify the perturbing potential, or equation Eq. (2.65) for the adiabatic couplings. This should get us back to the Boltzmann equilibrium.

$$\tilde{V}_{nm}(t) = V_{nm}(t)\sqrt{\frac{2}{1+e^{-\beta E_{nm}}}} \tag{2.64}$$

$$\tilde{S}_{nm}(t) = \tilde{S}_{mn}(t)\sqrt{\frac{2}{1+e^{-\beta E_{nm}}}} \tag{2.65}$$

It is important to note that, while Eq. 2.64 is used in VER and also applied to EET [5,46–48], theoretical work by Kim and Rossky [59] suggests that it may not be completely suited for adiabatic transitions between multiple PES. They propose a different equation to correct for the semi-classical approach, which is an interesting topic for future study, although it will most likely be of use to the Ehrenfest method with feedback to the bath, since NISE only propagates its bath variables on the PES of the electronic ground state.

2.3.5 A symmetrical thermal correction

However, the requirement of hermiticity states that for real values of V_{nm}, $\tilde{V}_{nm} = \tilde{V}_{mn}$ [5]. We can therefore introduce a *symmetric thermal correction* which assures $\tilde{V}_{nm} = \tilde{V}_{mn}$.

$$\tilde{V}_{nm}(t) = \sqrt{\frac{2}{1+e^{\beta E_{nm}}}}|c_m(t)|H_{nm}(t) - \sqrt{\frac{2}{1+e^{-\beta E_{nm}}}}|c_n(t)|V_{mn}(t) \tag{2.66}$$

$$= \left(\sqrt{\frac{2}{1+e^{\beta E_{nm}}}}|c_m(t)| - \sqrt{\frac{2}{1+e^{-\beta E_{nm}}}}|c_n(t)|\right)V_{nm}(t) \tag{2.67}$$

This has the property that the rate constants follow the Boltzmann relation, and that it conserves the hermiticity of the Hamiltonian. Anti-hermiticity of the nonadiabatic couplings leads to [46, 48]

$$\tilde{S}_{nm}(t) = \sqrt{\frac{2}{1+e^{\beta E_{nm}}}}|c_m(t)|S_{nm}(t) + \sqrt{\frac{2}{1+e^{-\beta E_{nm}}}}|c_n(t)|S_{mn}(t) \tag{2.68}$$

$$= \left(\sqrt{\frac{2}{1+e^{\beta E_{nm}}}}|c_m(t)| - \sqrt{\frac{2}{1+e^{-\beta E_{nm}}}}|c_n(t)|\right)S_{nm}(t) \tag{2.69}$$

One can derive that the transition rates will be zero (i.e. the system will be in equilibrium) if $\tilde{S}_{nm} = 0$, so if

$$\sqrt{\frac{2}{1+e^{\beta E_{nm}}}}|c_m(t)| = \sqrt{\frac{2}{1+e^{-\beta E_{nm}}}}|c_n(t)| \tag{2.70}$$

which implies

$$\frac{\rho_m}{\rho_n} = \frac{1+e^{\beta E_{nm}}}{1+e^{-\beta E_{nm}}} = e^{\beta E_{nm}} \tag{2.71}$$

following the Boltzmann distribution.

2.3.6 The recovery of high-temperature results

There is one problem with the definitions of the thermally corrected perturbation potential and nonadiabatic couplings in Eq. (2.66) through Eq. (2.69): they do not recover the population dynamics in the high-temperature limit, where

$$\lim_{\beta \longrightarrow 0} \sqrt{\frac{2}{1+e^{\beta E_{mn}}}} = \lim_{\beta \longrightarrow 0} \sqrt{\frac{2}{1+e^{-\beta E_{mn}}}} = 1 \tag{2.72}$$

Plugging this result into Eq. (2.69), for instance, gets us

$$\tilde{S}_{nm}(t) = (|c_m(t)| - |c_n(t)|)S_{nm}(t) \tag{2.73}$$

which means the rate constants follow the relation

$$\tilde{k}_{m\leftarrow n} \propto ||c_m(t)| - |c_n(t)||^2 |S_{nm}(t)|^2 \tag{2.74}$$

which does not (necessarily) equal $|S_{nm}(t)|^2$. This problem was noted by Aghtar *et al.* [47], and a solution was proposed: dividing each nonadiabatic coupling by a factor $|c_m(t)| - |c_n(t)|$, which gives us

$$\tilde{S}_{nm}(t) = \frac{\sqrt{\frac{2}{1+e^{\beta E_{nm}}}}|c_m(t)| - \sqrt{\frac{2}{1+e^{-\beta E_{mn}}}}|c_n(t)|}{|c_m(t)| - |c_n(t)|} S_{nm}(t) \tag{2.75}$$

which, as one can check, still obeys antisymmetry, and has the added bonus that it recovers high-temperature results.

A sanity check

The eventual aim of this project is to apply the thermal corrections to NISE even in large systems. Therefore, we should check that the adjustments we make do not adversely affect population transfer between sparsely populated states. Consider a trimer, where state $|\tilde{\psi}_0(t)\rangle$ has a population of $\frac{1}{2}$. Now, also consider that there is no coupling between $|\tilde{\psi}_0(t)\rangle$ and the other two states, $|\tilde{\psi}_1(t)\rangle$ and $|\tilde{\psi}_2(t)\rangle$. Therefore, if the other half of the population starts out in state $|\tilde{\psi}_1(t)\rangle$, we can say that the dynamics are the same, except for the absolute values of the wavefunction coefficients, which are effectively halved. However, our rate constants must be the same, since they govern the relative transfer of populations between states. Halving the rate constants (which would happen if we were to leave out the denominator of Eq. (2.75)) would yield significantly slower dynamics. With this in mind, we realise that Eq. (2.75) does indeed give a sensible thermal correction.

One last problem?

One can see that the denominator of Eq. (2.75) is not necessarily positive, and that it may become zero. In this case, Aghtar *et al.* built in a numerical boundary for the denominator [47], such that values of $|c_n(t)|$ and $|c_m(t)|$ that are too close together would not reach a singularity. However, in their work, they also establish that this numerical boundary is never reached during many hours of computations.

2.3.7 Alternative thermal corrections

Other corrections to the perturbation Hamiltonian or nonadiabatic couplings exist, and we can postulate other thermal corrections based on a few simple rules:

1. $\tilde{k}_{m\leftarrow n} = e^{-\beta E_{mn}}\tilde{k}_{n\leftarrow m}$, i.e. the rate constants follow the Boltzmann distribution. For this, $|V_{mn}(t)|^2 = e^{-\beta E_{mn}}|V_{nm}(t)|^2$
2. Use the process outlined in 2.3.5 to symmetrise the the thermal correction (or anti-symmetrise it in the case of the nonadiabatic couplings).
3. $\tilde{k}_{m\leftarrow n} = \tilde{k}_{n\leftarrow m} = k_{n\leftarrow m} = k_{m\leftarrow n}$ in the high-temperature limit.
   This implies that $|\tilde{V}_{mn}(t)|^2 = |\tilde{V}_{nm}(t)|^2 = |V_{nm}(t)|^2 = |V_{mn}(t)|^2$
   and $|\tilde{S}_{nm}(t)|^2 = |\tilde{S}_{mn}(t)|^2 = |S_{nm}(t)|^2 = |S_{mn}(t)|^2$.
4. Another limitation is that, while transport from a lower-energy state to a higher-energy state should be suppressed, transport from a higher-energy state to a lower-energy state should not be enhanced significantly. Relaxation through bath interactions cannot occur on infinitely short timescales. If possible, we would like to preserve the relaxation time, $\tilde{T}_1 = (\tilde{k}_{m\leftarrow n} + \tilde{k}_{n\leftarrow m})^{-1} = T_1 = (k_{m\leftarrow n} + k_{n\leftarrow m})^{-1}$ for all temperatures.

Ref. 60 contains a collection of a few alternative thermal corrections, that each have their benefits and drawbacks, and are each suited to particular parameter regimes.

2.4 Summary

In short, this work will cover two different methods of recovering the Boltzmann distribution in the dynamics of open quantum systems at finite temperatures.

The first of these is called NISE-DBa (Numerical Integration of the Schrödinger Equation with Detailed Balance, version a). It adjusts the nonadiabatic couplings between the states, such that the resulting perturbative rate constants will drive the dynamics of the system toward the Boltzmann distribution. This method has been described in Sections 2.3.4 and 2.3.5. The difference between the method used here and in Refs. 46 and 48, is that an additional correction has been implemented (taken from Ref. 47 and outlined in Section 2.3.6) to recover the high-temperature results of NISE.

The second of these methods is called NISE-DBb (NISE-DB, version b). It computes the difference between the Hamiltonian at any timestep, and the time-averaged (or 'ideal') Hamiltonian. This difference is considered a perturbation. From this perturbation, we can compute the perturbative rate constants, which are subsequently adjusted such that the system is driven to the Boltzmann distribution. It has been implemented in full in Ref. 47, including the high-temperature correction outlined in Section 2.3.6 but not compared to NISE-DBa. Additionally, the dynamics will be computed in the average eigenbasis in addition to the local and adiabatic bases. Initially exciting a particular excitonic state (closely linked to an average eigenstate) and watching the system's dynamics is very close to the physical processes of absorption that occur in nature and experiment.

These methods will be compared to each other and two benchmark methods: NISE and HEOM, in several parameter regimes (perturbative, highly nonperturbative, fast and slow fluctuations). This will give an idea of whether these methods can be used in the simulation of two-dimensional spectra and comparison to experiment.

Chapter 3

Results

This chapter will show the results of the simulations done with the HEOM, NISE and NISE-DB methods. Important is that both *populations* and *coherences* are displayed.

The first section will cover how to reproduce the plots, by providing the code used for all of the methods involved. The second section will quickly go over recovering the high-temperature results. The third section shows results in dimer (two-chromophore) systems that mimic natural light-harvesting systems. The fourth section shows results for artificial systems in various parameter regimes. In the fifth section, we will explore how the methods generalise to larger-scale systems. Finally, in the sixth section, we will summarise and discuss the results.

3.1 Reproducing the plots

For the simulation of the population trajectories with HEOM, I have made use of the PHI (Parallel Hierarchy Integration) designed by Johann Strümpfer [44]. Unless indicated otherwise, no use has been made of Matsubara frequencies, the timestep taken has been 1 fs and the hierarchy truncation depth has been 20. In accordance with the model Hamiltonians, only diagonal energetic disorder has been applied. The disorder associated with each of the sites is considered uncorrelated with the rest.

For the simulation with NISE and the NISE-DB methods, I developed new subroutines for the NISE_2017 package developed by Thomas la Cour Jansen. The explanation of this code and a quick-use manual can be found in Appendix B.

The plots in the following sections will have very similar layouts. A plot shown in local basis, also means that the system has been propagated with the excitation having been put on the highest-energy chromophore initially. In average eigenbasis, the highest average eigenstate has been excited initially, and in the adiabatic basis, the same holds for the highest-energy instantaneous eigenstate. Four methods will be compared: HEOM, NISE, NISE-DBa and NISE-DBb. The symbols on the y-axes are $\bar{\rho}_{00}(t)$, or the bath-averaged population, and $\bar{\rho}_{01}(t)$, or the bath-averaged (absolute value of the) coherence.

In all cases except the adiabatic basis, the HEOM results shall be used as a benchmark for the other methods: their quality of thermalisation shall be determined by comparing the long-term (equilibrium) populations. Other features that will be inspected are short-term population oscillations and long-term coherences.

3.2 High-temperature limit

Let us first check the easiest box: whether the methods described in the previous chapter actually yield the same results in the high-temperature limit. The Hamiltonian under consideration is as follows:

$$H(t) = \begin{pmatrix} V + \sigma x_1(t) & V \\ V & \sigma x_2(t) \end{pmatrix} \tag{3.1}$$

where $V = 100\,\mathrm{cm}^{-1}$. The values of σ_i are fixed to $100\,\mathrm{cm}^{-1}$ as well. For this, a small bit of mental gymnastics is needed, since Eq. (2.14) tells us that the value of σ is not only determined by the reorganisation energy, but also by the thermal energy. At a temperature of $10^9\,\mathrm{K}$, the value of λ needs to be fixed to $\lambda = 7.19 \cdot 10^{-6}\,\mathrm{cm}^{-1}$. The number of samples used is 10000. The value of γ is given as $10\,\mathrm{ps}^{-1}$. The results of this simulation can be found in Figs. 3.1, 3.2 and 3.3.

As can be seen, the results in all three bases are roughly similar. Any differences between HEOM and the NISE methods (with and without detailed balance) can be ascribed to insufficient sampling. There is no observable difference between the different NISE methods, regardless of thermal corrections. This is as expected, and shows that the methods behave as expected in the high-temperature limit.

3.3 Intermediate temperatures

Of course, the justification for the detailed balance methods is that they should perform better than NISE at finite temperatures. Therefore, this section shall cover three different

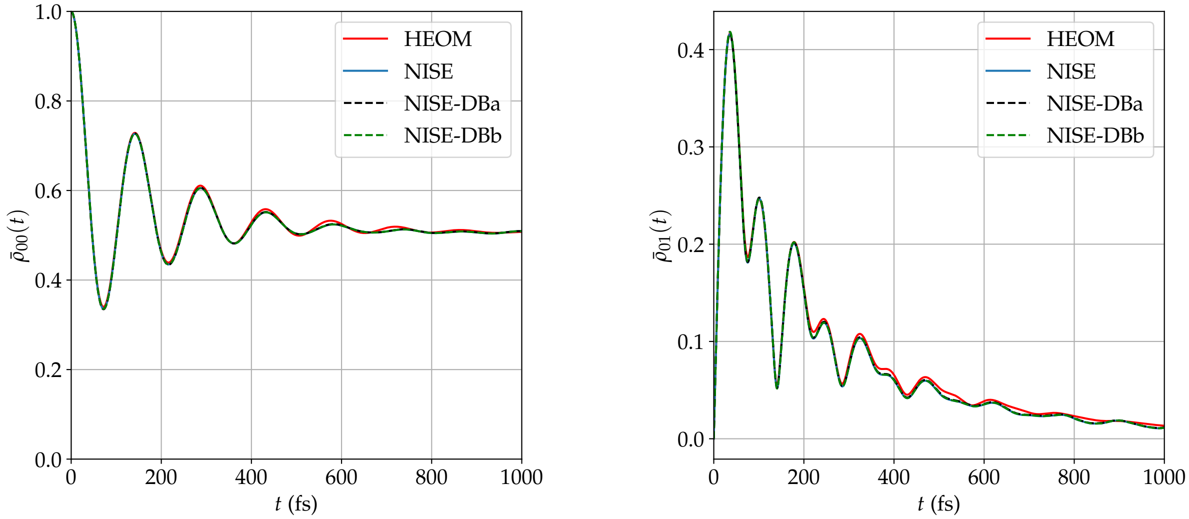

(a) Population of the highest-energy site in the high-temperature limit. As expected, the populations all tend to the same equilibrium.

(b) The absolute value of the coherence between the two sites. Once again, the four methods all recover similar results.

FIGURE 3.1: The populations and coherences in site basis, in the high-temperature limit. Owing to the high-temperature correction proposed in Ref. 47, all four methods recover the same result.

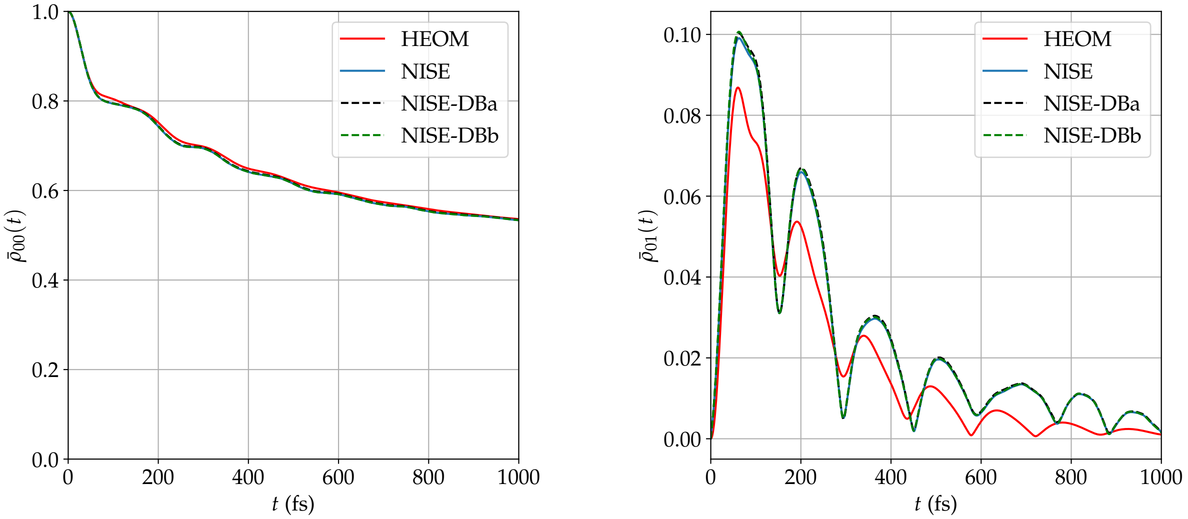

(a) Population of the highest-energy average eigenstate in the high-temperature limit. As expected, all four methods tend to the same, uniformly distributed, equilibrium.

(b) The absolute value of the coherence between the two average eigenstates. The discrepancies between the HEOM and NISE methods can be attributed to poor sampling.

FIGURE 3.2: The populations and coherences in average eigenbasis, in the high-temperature limit. The methods yield very similar results.

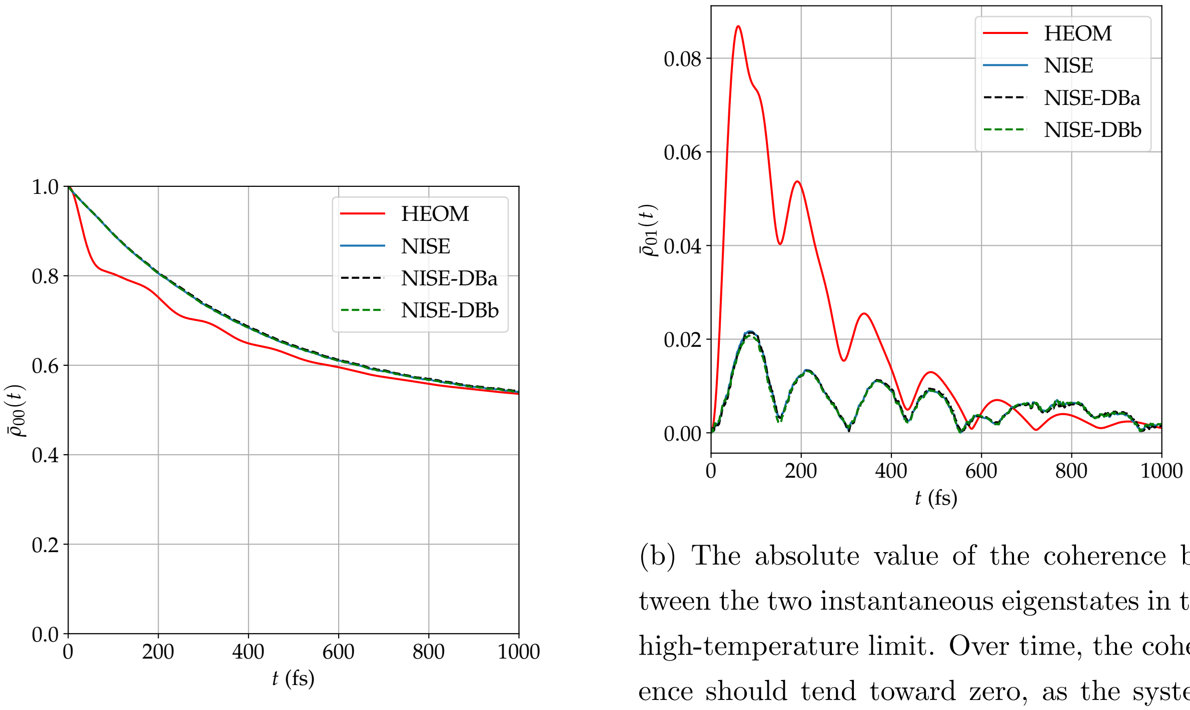

(a) The population of the highest-energy instantaneous eigenstate in the high-temperature limit.

(b) The absolute value of the coherence between the two instantaneous eigenstates in the high-temperature limit. Over time, the coherence should tend toward zero, as the system is relaxing toward thermal equilibrium. The remaining coherence at longer timescales can be attributed to poor sampling.

FIGURE 3.3: The populations and coherences in adiabatic basis, in the high-temperature limit. Important to note is the discrepancy between the HEOM and NISE methods. The results of HEOM are shown in the average eigenbasis, as the method has no equivalent in the adiabatic basis. Other methods, such as surface hopping, can be used to find a physically plausible result in the adiabatic basis. A feature that will arise in other systems is the significantly higher coherence peak in the HEOM trajectory. This should not be considered a failing of the other methods, rather a limitation of HEOM.

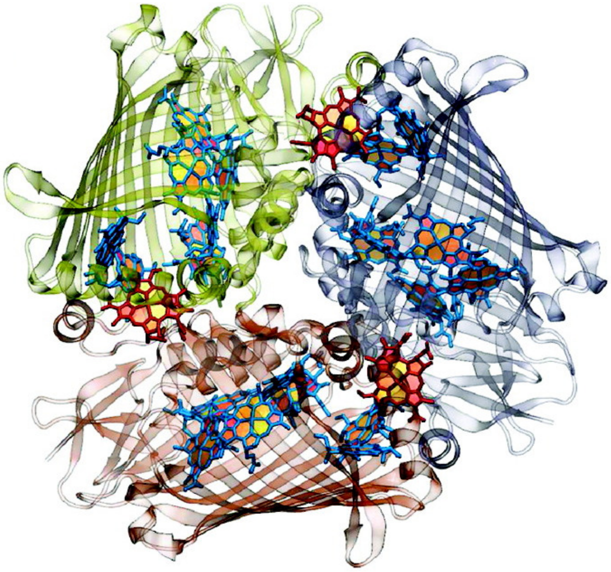

Figure 3.4: FMO trimer with the protein structure in cartoon representation. Adapted with permission from Ref. 61. © 2011, American Chemical Society.

systems inspired by real life. In all three cases, the temperatures are considered to be at room temperature, 300 K.

3.3.1 The FMO complex

The Fenna-Mathews-Olson (FMO) complex (Fig. 3.4) is a light harvesting system found in the green sulphur bacterium *Chlorobium tepidium* and has been the subject of many experimental studies due to the (disputed) suggestion of long-lived excitonic coherences [18, 19, 21, 24]. It consists of a trimer, each of whose parts contains eight chromophores.

In previous work [4] the system has been described with dimer parameters obtained from Ref. 22. In this description, the average Hamiltonian is given as in Eq. 3.2.

$$H_0 = \begin{pmatrix} 140 & -106 \\ -106 & 0 \end{pmatrix} \mathrm{cm}^{-1} \tag{3.2}$$

The width of the energetic fluctuations is $150\,\mathrm{cm}^{-1}$ and its coherence time is around 140 fs. In the calculation, a timestep of 1 fs has been used. For the results of the NISE-related methods, a stochastic average was taken over 50000 samples in order to reduce the error due the wobbly nature of the individual trajectories. The results for the FMO complex can be seen in Figs. 3.5 (local basis), 3.6 (average eigenbasis) and 3.7 (adiabatic basis).

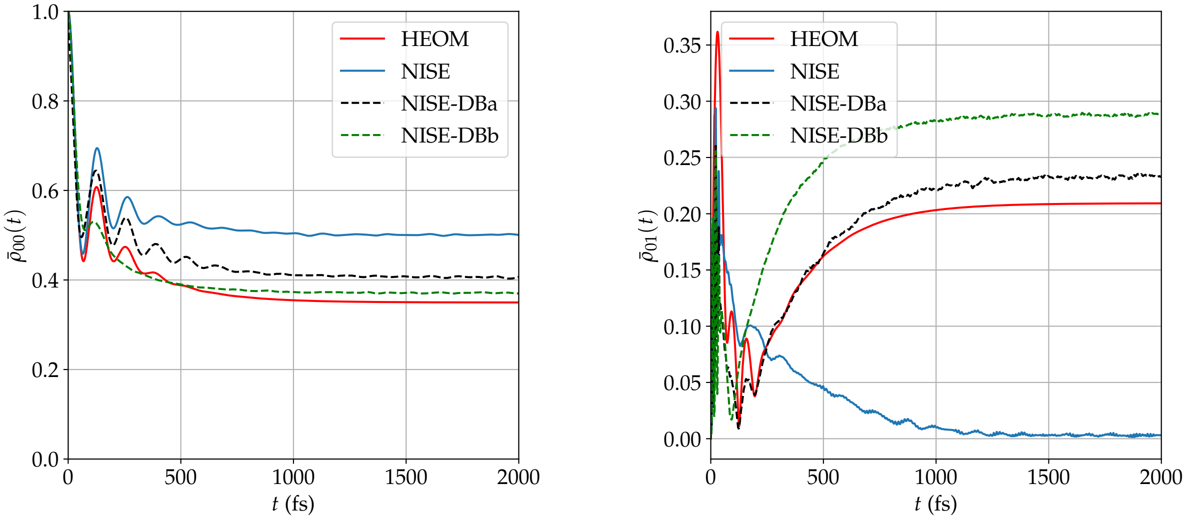

(a) The population of the highest-energy site as a function of time. Important features to note are the fast decoherence of the trajectory according to NISE-DBb, and the fact that NISE-DBb provides a better match to the equilibrium population as predicted by HEOM than NISE-DBa.

(b) The coherence between the two states in site basis as a function of time. Important to note is the fact that NISE underestimates the equilibrium coherence, whereas both NISE-DBa and NISE-DBb overshoot the mark, although NISE-DBa provides a much closer approximation.

FIGURE 3.5: The populations and coherences of the FMO complex (Eq. (3.2)) in local basis, with the excitation initially on the highest-energy chromophore. As shown before by Aghtar *et al.* (Ref. 47), the NISE-DBb approach underestimates the coherent oscillations at timescales below 500 fs. NISE-DBa provides a reasonable approximation, though, as shown by Nijjar *et al.* (Ref. 48), it does not fully reach the thermal equilibrium as predicted by HEOM.

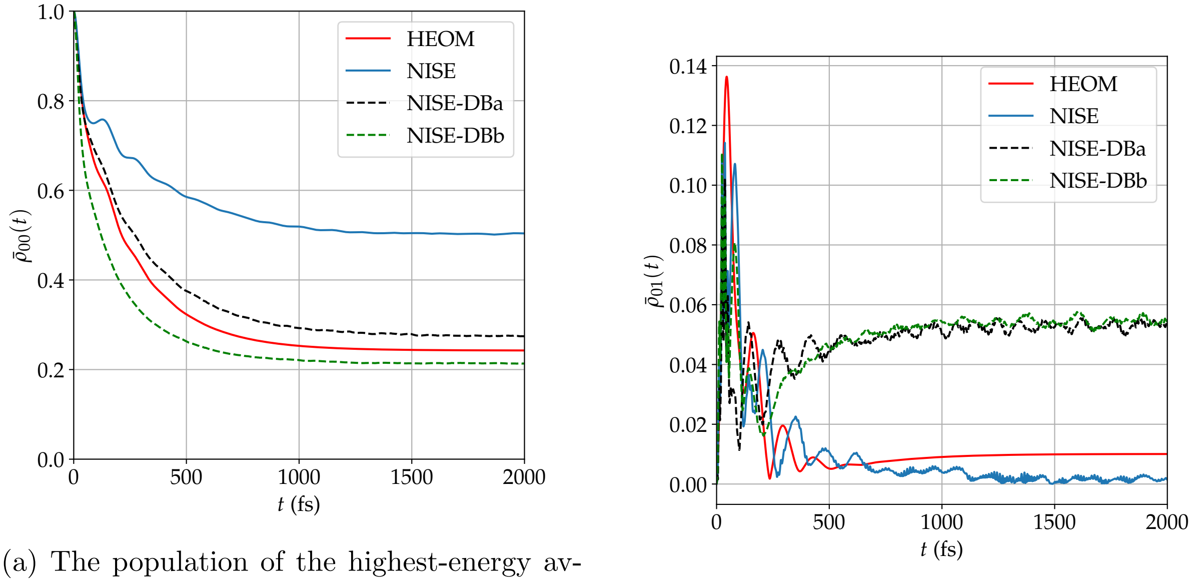

(a) The population of the highest-energy average eigenstate over time. Note the large discrepancy between NISE and HEOM, and the fact that both NISE-DBa and NISE-DBb approximate the thermal equilibrium predicted by HEOM very closely.

(b) The absolute value of the coherence between the average eigenstates. The trajectories are noisy on short timescales. Moreover, both NISE-DBa and NISE-DBb highly overestimate the coherence at longer timescales.

FIGURE 3.6: The populations and coherences of the FMO complex (Eq. (3.2)) in average eigenbasis, with the system initially being in the highest-energy average eigenstate. Both NISE-DBa and NISE-DBb manage to approach the equilibrium population expected by HEOM, with NISE-DBa more closely approaching HEOM at short timescales.

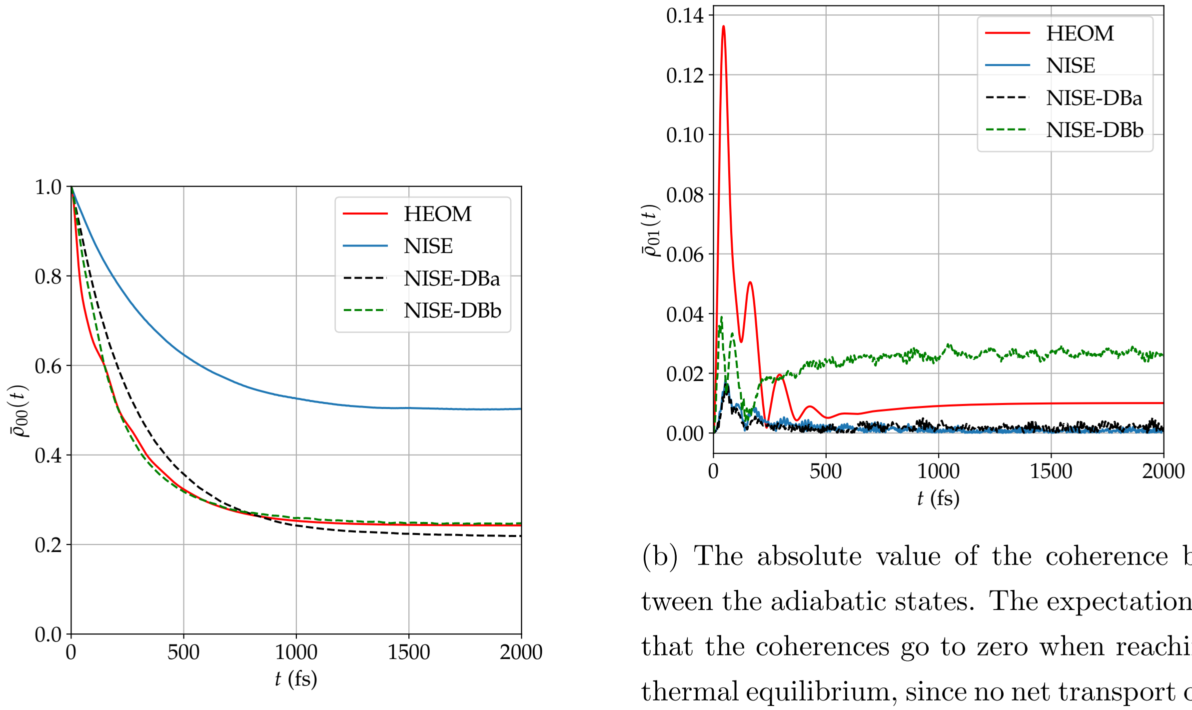

(a) The population of the highest-energy instantaneous eigenstate over time. Although both NISE-DB methods provide a close approximation to the HEOM results, the HEOM populations are shown in average eigenbasis, complicating a comparison.

(b) The absolute value of the coherence between the adiabatic states. The expectation is that the coherences go to zero when reaching thermal equilibrium, since no net transport occurs between the adiabatic eigenstates. Both NISE and NISE-DBa follow this prediction. HEOM, shown in average eigenbasis, does not agree with this. NISE-DBb significantly overestimates the equilibrium value of the coherence.

FIGURE 3.7: The populations and coherences of the FMO complex (Eq. (3.2)) in adiabatic basis, with the system initially being in the highest-energy adiabatic state. NISE and NISE-DBa reproduce the correct expectation for the absolute value of the coherence at long timescales, tending to zero. The physical equilibrium found by both methods is difficult to compare to the result from HEOM, which is shown in average eigenbasis instead.

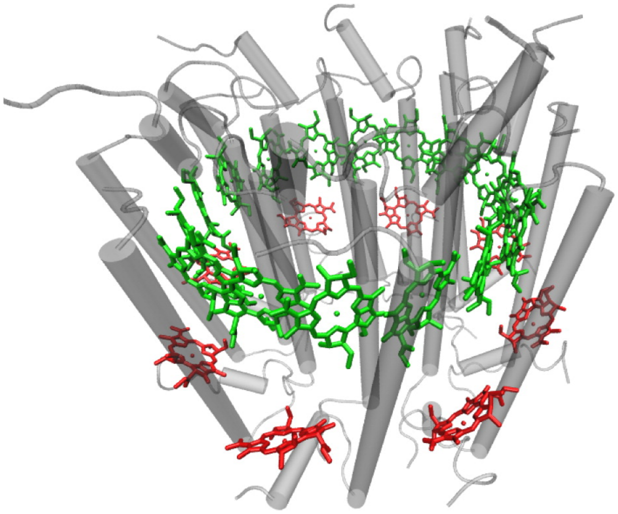

FIGURE 3.8: Schematic overview of the LH2 complex of *Rsp. molischianum*. Reprinted with permission from Ref. 1. © 2015, American Chemical Society.

These results suggest that NISE-DBb shows slightly more accurate population relaxation in the local basis, accompanied by slightly too fast short-term loss of coherence and an overestimated equilibrium value of the coherence. NISE-DBa manages to recover the equilibrium coherence quite well. In the average eigenbasis, however, both NISE-DBa and NISE-DBb achieve reasonably accurate population relaxation, at the expense of a slightly worse agreement in the coherences. In the adiabatic basis, both methods show similarly accurate population relaxation, but only NISE-DBa manages to reach the expected equilibrium coherence.

NISE-DBa manages to perform quite well. The relatively slow bath decoherence appears to be helpful in this regard: slow fluctuations mean that the nonadiabatic couplings remain small and the assertion that they can be treated perturbatively (which underpins the NISE-DBa method) appears true.

3.3.2 The LH2 complex

The LH2 complex (Fig. 3.8) is a second light-harvesting system, a vital part of the photosystems of purple bacteria such as *Rhodospirillum photometricum* and *Rsp. molischianum* [1, 16]. In previous work (Ref. 4) it has been described with dimer parameters obtained from *Rsp. molischianum* in Ref. 62. This Hamiltonian is given in Eq. 3.3.

$$H_0 = \begin{pmatrix} 300 & 47 \\ 47 & 0 \end{pmatrix} \text{cm}^{-1} \tag{3.3}$$

The width of the energetic disorder is $100\,\text{cm}^{-1}$, the decoherence time is 100 fs and a timestep has been used of 1 fs. A stochastic average was taken over 20000 samples. The results can be seen in Fig. 3.9.

These results suggests that NISE-DBb has a significant edge over NISE-DBa in the parameter regime associated with the Hamiltonian in Eq. (3.3), that is, the dynamic disorder ($\sigma = 100\,\text{cm}^{-1}$) is significantly smaller than the static disorder ($\Delta_E = 300\,\text{cm}^{-1}$) and the difference in energy between the average eigenstates. This means that the average Hamiltonian is a good description of the system, and the perturbative treatment in NISE-DBb is justified.

3.3.3 The amide I and II bands

The third and last nature-inspired system that we will be considering in this work is the coupling between the amide I and II bands. Relaxation from the amide I to amide II band has been suggested to play a role in the transport of excess energy, e.g. after ATP hydrolysis [63].

As done before in Ref. 4, the dimer parameters are taken from Ref. 63, where N-methyl acetamide (NMA) is used as a model for the peptide bond found in the backbone of proteins. The average Hamiltonian is given in Eq. (3.4).

$$H_0 = \begin{pmatrix} 70 & 36 \\ 36 & 0 \end{pmatrix} \text{cm}^{-1} \tag{3.4}$$

The width of the energetic disorder is $25\,\text{cm}^{-1}$, the decoherence time is 50 fs. A timestep has been taken of 1 fs and a stochastic average has been taken over 20000 samples. The results of the simulations are shown in Fig. 3.10.

These results show that the parameter regime of relatively fast fluctuations ($\tau = 50\,\text{fs}$) is not suited to the NISE-DBa method. The NISE-DBb method performs slightly better in showing the right trend, despite the $\sim 5\%$ absolute difference between HEOM and NISE-DBb populations. The dynamic disorder is small enough that the average Hamiltonian describes the system decently.

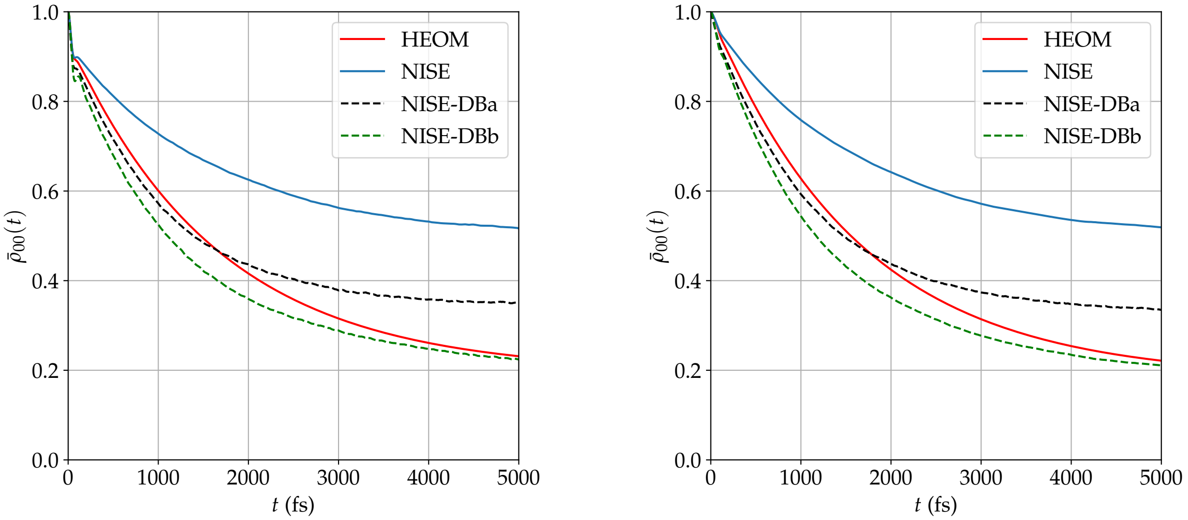

(a) The populations in local basis.

(b) The populations in average eigenbasis.

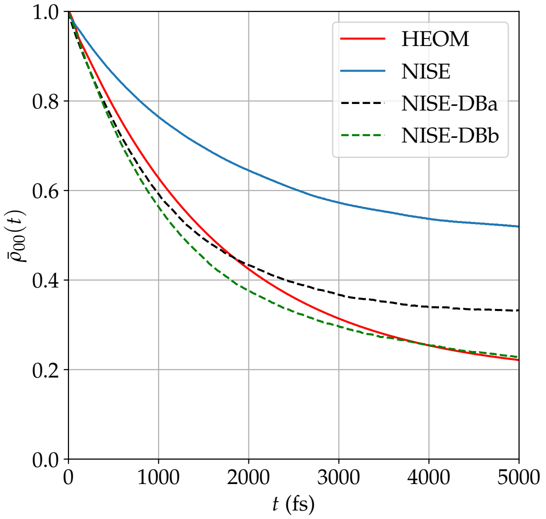

(c) The populations in adiabatic basis.

FIGURE 3.9: The populations of the LH2 complex (Eq. (3.3)) in (a) local basis, (b) average eigenbasis and (c) adiabatic basis. There are very few differences between each of the three graphs except short-term population dynamics. While NISE-DBb shows faster-than-expected population relaxation at short timescales, it makes up for the loss by giving accurate results for the equilibrium population. NISE-DBa, while showing promising results in short-timescale dynamics, does not achieve nearly as accurate equilibrium populations.

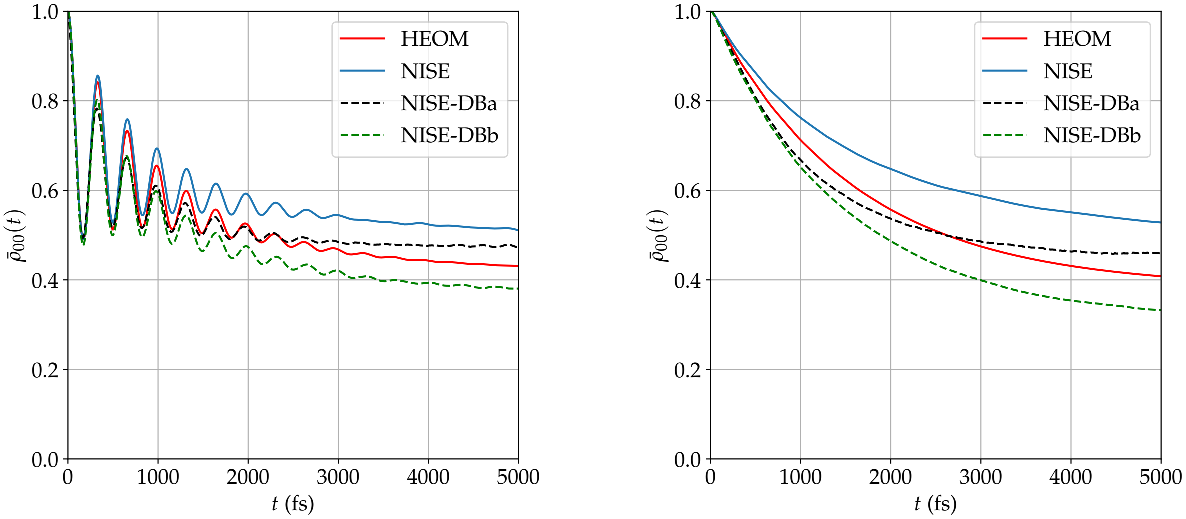

(a) The populations in local basis.

(b) The populations in average eigenbasis.

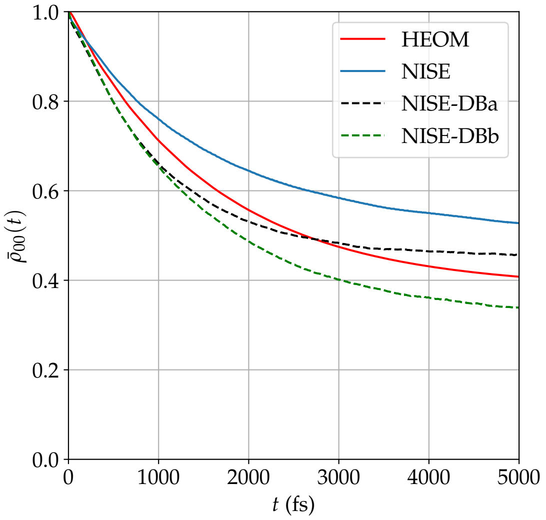

(c) The populations in adiabatic basis.

FIGURE 3.10: The populations of the amide I/amide II system (Eq. (3.4)) in (a) local basis, (b) average eigenbasis and (c) adiabatic basis. The discrepancies between HEOM and the NISE-DB methods are large, especially after $t = 1000\,\text{fs}$.

3.4 Limitations of the perturbative approach

For this section, an approach is used that reflects Ref. 47. There, the authors fix the average Hamiltonian to Eq. (3.5).

$$H_0 = \begin{pmatrix} V & V \\ V & 0 \end{pmatrix} \tag{3.5}$$

where $V = 100\,\mathrm{cm}^{-1}$. The temperature is kept at a constant 300 K, but the reorganisation energy, which determines the width of the distribution of site energies, is varied between different values. The bath decoherence time is kept constant at 100 fs. Doing this, it is possible to identify the parameter regimes in which the approach works best. From the use of Fermi's Golden Rule, it has become clear that the accuracy of the thermal corrections should depend on the strength of the fluctuations. The expectation is that systems with small fluctuations can be described better by the thermalised model than systems with large fluctuations. The goal is to get a decent grasp on the parameter regimes that can be described by the two thermalised models. The results of these simulations can be seen in Fig. 3.11 (local basis) and Fig. 3.12 (average eigenbasis).

In local basis, NISE-DBb appears to lose coherence quickly, but manages to converge to the population predicted by HEOM. A feature that can be seen in Fig. 3.11 is the fast population relaxation (starting linearly at $t = 0$, rather than quadratically like other methods) as predicted by NISE-DBa. This is an unphysical result, which can be due to large denominators in Eq. (2.75). The performance of NISE-DBa can see improvements if we find a solution to this problem.

A nice observation is that when exciting only the highest average eigenstate, the NISE-DBa method can yield results that are strikingly close to the results predicted by HEOM. This spells good news for its ability to reproduce some two-dimensional spectra, since the observables are closely (but not exactly) linked to dynamics in the average eigenbasis.

3.5 Larger-scale systems

It is promising that the adiabatic detailed balance method (NISE-DBa) seems to work well for many systems, especially when considering the populations in average eigenbasis. However, in order for this method to have a marginal benefit over NISE or HEOM, it must continue to yield accurate results in larger systems. To this end, it is useful to start simulating larger systems. The first hurdle to overcome is to go from a dimer system to

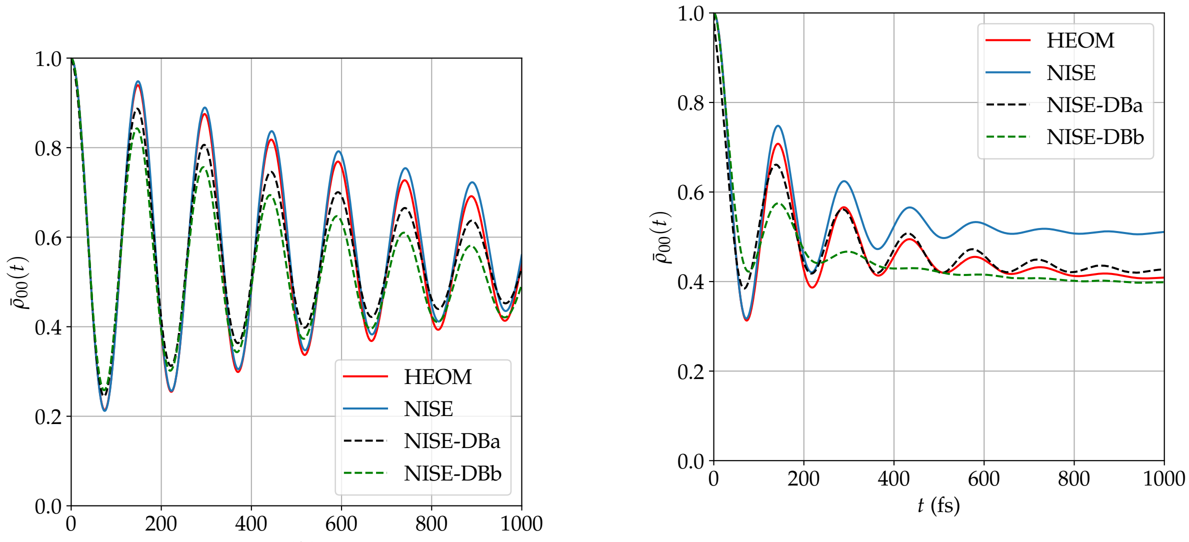

(a) The small fluctuation limit, where $\lambda = 2\,\mathrm{cm}^{-1}$, resulting in a width of $\sigma = 28.9\,\mathrm{cm}^{-1}$

(b) The intermediate fluctuation limit, where $\lambda = 20\,\mathrm{cm}^{-1}$, resulting in a width of $\sigma = 91.3\,\mathrm{cm}^{-1}$

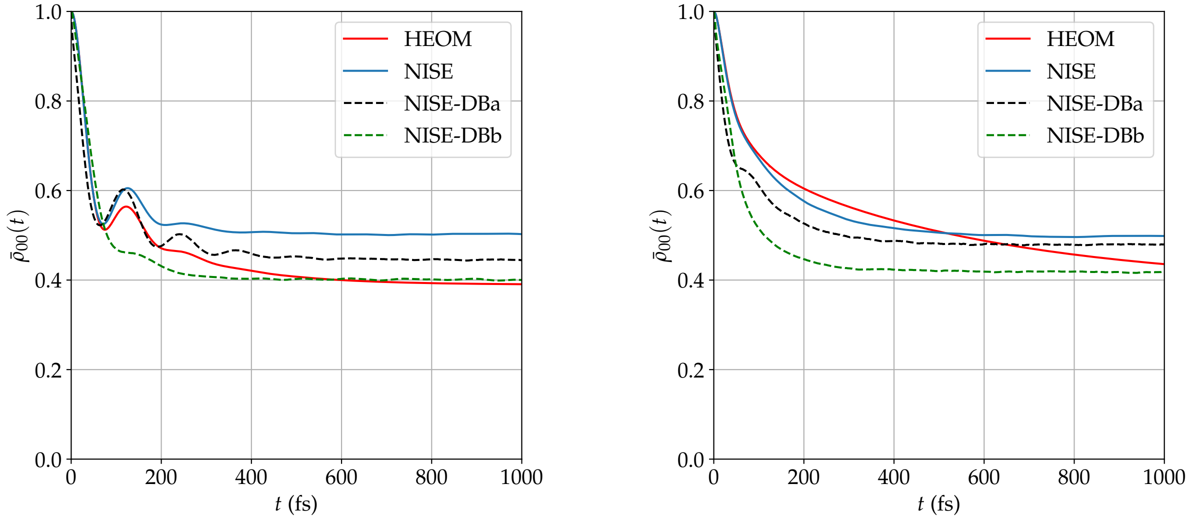

(c) The large fluctuation limit, where $\lambda = 100\,\mathrm{cm}^{-1}$ and $\sigma = 204.2\,\mathrm{cm}^{-1}$

(d) The very large fluctuation limit, where $\lambda = 500\,\mathrm{cm}^{-1}$ and $\sigma = 456.6\,\mathrm{cm}^{-1}$

FIGURE 3.11: The population of the highest-energy chromophore over time, for the Hamiltonian in Eq. (3.5). For small fluctuations, up to $\sigma = 91.3\,\mathrm{cm}^{-1}$, the NISE-DBa method gives reasonable results. In the large fluctuation limit, despite its quick short-term loss of coherence, NISE-DBb reproduces the equilibrium population very accurately. For large dynamic disorder, neither of the NISE-DB methods achieves good agreement with HEOM.

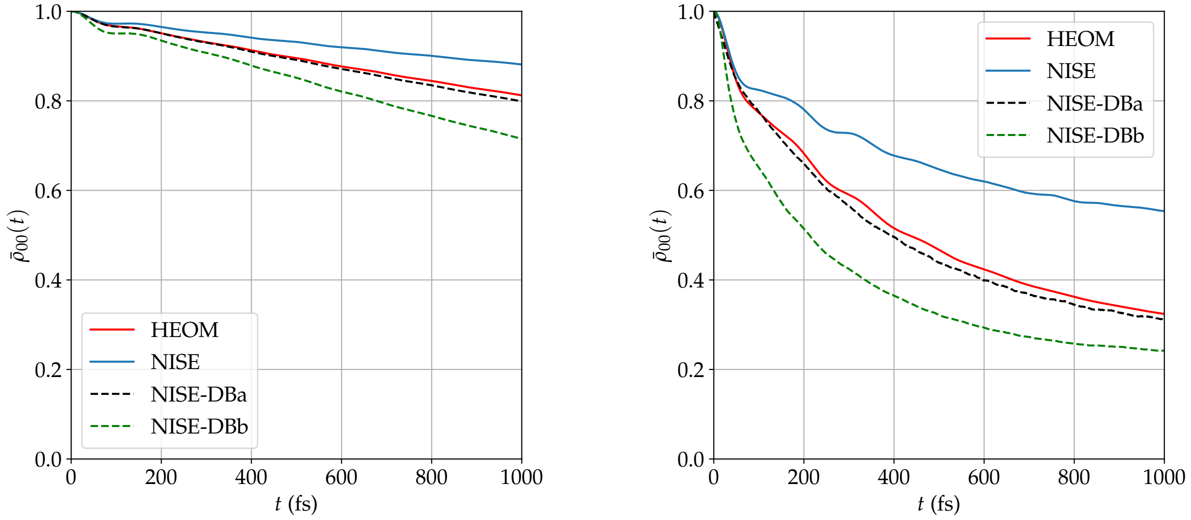

(a) The small fluctuation regime, where $\lambda = 2\,\mathrm{cm}^{-1}$ and $\sigma = 28.9\,\mathrm{cm}^{-1}$

(b) The intermediate fluctuation regime, where $\lambda = 20\,\mathrm{cm}^{-1}$ and $\sigma = 91.3\,\mathrm{cm}^{-1}$

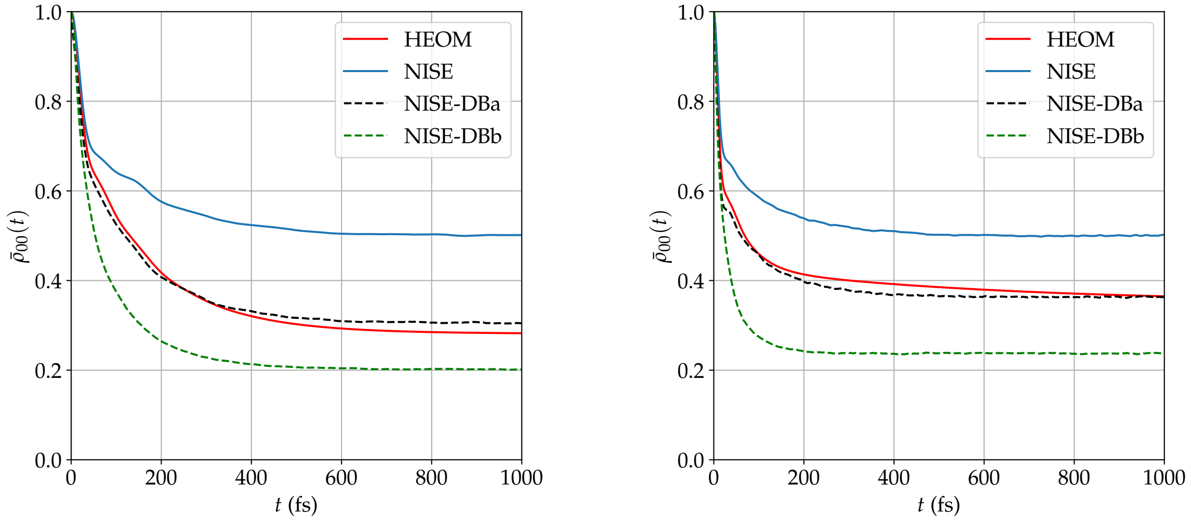

(c) The large fluctuation regime, where $\lambda = 100\,\mathrm{cm}^{-1}$ and $\sigma = 204.2\,\mathrm{cm}^{-1}$

(d) The very large fluctuation regime, where $\lambda = 500\,\mathrm{cm}^{-1}$ and $\sigma = 456.6\,\mathrm{cm}^{-1}$

FIGURE 3.12: The populations of the highest-energy average eigenstates over time, for the Hamiltonian in Eq. (3.5). No matter the size of the dynamic disorder, NISE-DBa appears to reproduce the dynamics of HEOM very accurately.

a trimer system. NISE-DBa deals with populations in the adiabatic basis. In a dimer, the two adiabatic states are always correctly ordered: crossings of the site basis energies yields an avoided crossing in adiabatic basis. However, this ordering disappears when we are dealing with a trimer system - suddenly, there is a possibility of level crossings. While this is easy to realise in a analytic setting, since the time evolution preserves invariant subspaces of the Hilbert space, the *in silico* implementation has proven to be challenging: the ordering of the eigenstates causes computational problems, and we must thus keep track of it ourselves. This has resulted in the 'swaps' subroutine, explained in Appendix B.

3.5.1 A dimer disguised as a trimer

The simplest trimer system that adds complexity to our calculation would be a system whose Hamiltonian is defined in Eq. .

$$H_0 = \begin{pmatrix} V & V & 0 \\ V & 0 & 0 \\ 0 & 0 & -V \end{pmatrix} \mathrm{cm}^{-1} \tag{3.6}$$

where $V = 100\,\mathrm{cm}^{-1}$. This would be equivalent to taking the system in Section 3.4 and adding a third chromophore at infinity. All three chromophores' energies fluctuate, however only two of the molecules feel each others' influence due to a nonzero excitonic coupling.

It is now possible to define two invariant subspaces in our Hilbert space: populations in the first two states will evolve in exactly the same way as in 3.4, whereas any population on the third site will not evolve over time at all.

Having implemented the aforementioned 'swaps' routine, it becomes easy to see that the results are identical to the ones in 3.4. Given that $\lambda = 20\,\mathrm{cm}^{-1}$ and $\gamma = 10\,\mathrm{ps}^{-1}$, the results can be seen in Fig. 3.13.

These results show that all methods used in this work conserve the invariant subspaces of the system's Hilbert space.

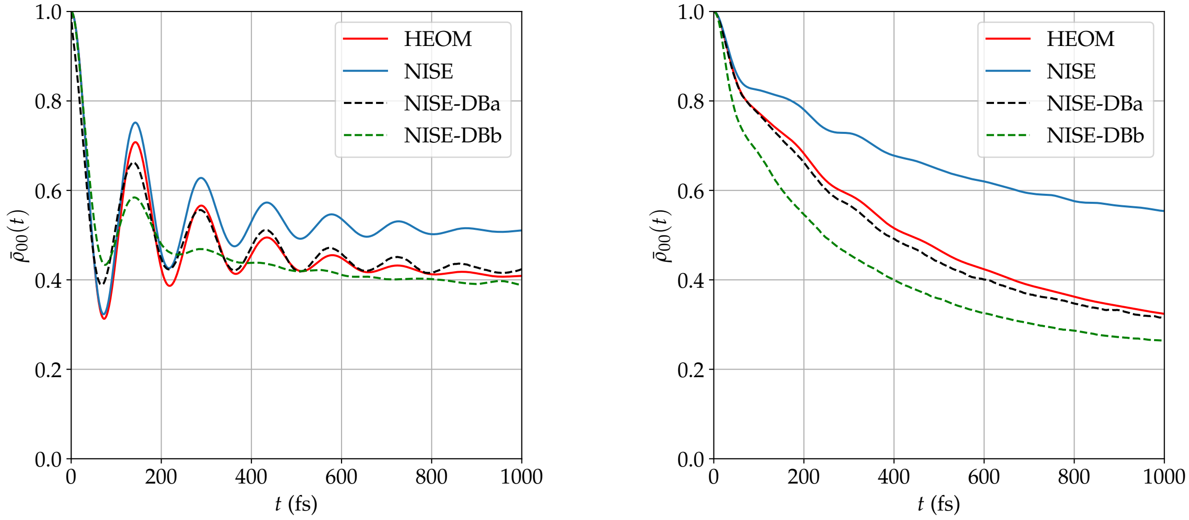

(a) The population in local basis.

(b) The population in average eigenbasis.

FIGURE 3.13: The time dependence of the populations in the hypothetical trimer system whose Hamiltonian is given by Eq. (3.6). As expected, the population transfer follows the same dynamics as the dimer system in the intermediate fluctuation regime, as shown in Figs. 3.11b and 3.12b.

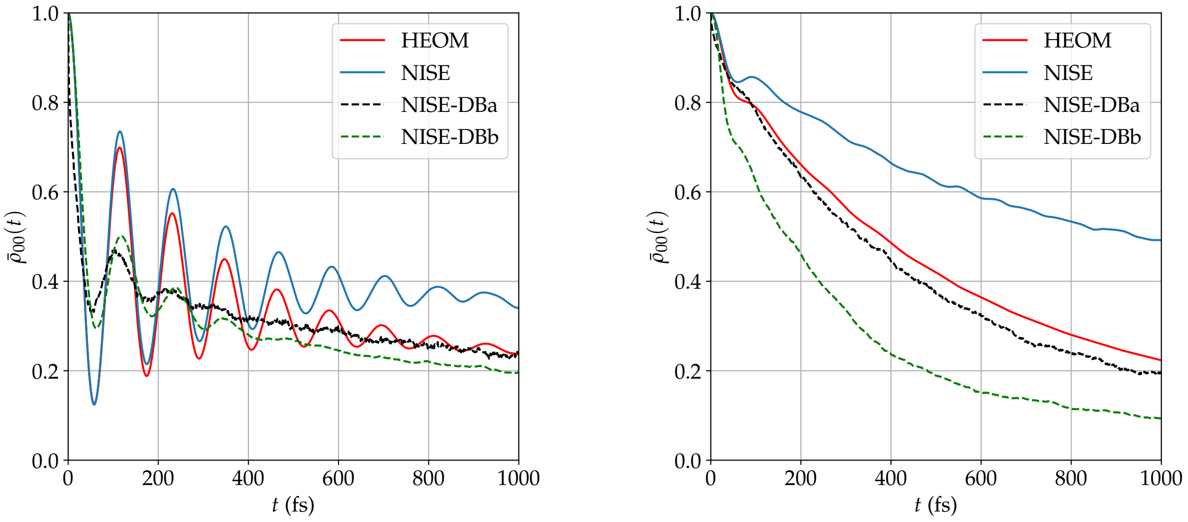

(a) The population in local basis.

(b) The population in average eigenbasis.

FIGURE 3.14: The time dependence of the populations in the hypothetical trimer system whose Hamiltonian is given by Eq. (3.7).

3.5.2 One step further: an equilateral trimer

Now, it is time to explore the accuracy of the NISE-DBa and NISE-DBb methods if we are dealing with a fully-connected trimer whose Hamiltonian is given in Eq. (3.7).

$$H_0 = \begin{pmatrix} V & V & V \\ V & 0 & V \\ V & V & -V \end{pmatrix} \text{cm}^{-1} \tag{3.7}$$

where $V = 100\,\text{cm}^{-1}$. This would be equivalent to placing the three chromophores in an equilateral triangle, since the interactions between each of the three pairs of chromophores is equally strong. The resulting trajectories are shown in Fig. 3.14.

An obvious feature of the above trajectories is the quick loss of coherence in the NISE-DBa and NISE-DBb schemes, when starting out with all population on the highest-energy chromophore. However, NISE-DBa still performs well when looking at the trajectory in average eigenbasis. Perhaps the performance of NISE-DBa can be improved by looking at alternatives to its ‘swaps’ routine, as laid out in Appendix B.

3.6 Discussion

Of all the simulations in this chapter, perhaps the most important are the computations in average eigenbasis, and the simulations of the equilateral trimer.

The former are important because they are closely linked to how excitons are transported in nature and experiment: the excitonic states are the eigenstates of the time-averaged Hamiltonian over the relevant interaction time (i.e. the pulse lengths in a 2D spectroscopic experiment). Therefore, producing results that are close to the HEOM predictions in the average eigenbasis spells good news for a method. In many of the simulations, NISE-DBa appears to get results that are very close to those of HEOM.

The latter are important because our models must be easily generalisable to larger systems, since this is where NISE has an edge over HEOM in terms of computational cost. While neither of the NISE-DB methods give very good results when considering the transport between individual chromophores, but NISE-DBa, at least in the parameter regime considered, gives reasonable results in the average eigenbasis.

3.6.1 On the relevance of basis

The astute reader might find a problem with particular methods doing well in one basis, while not performing well in another. This would indeed be a problematic thing if the physics displayed in the graphs were completely the same. The thermal corrections in the NISE-DB methods are not basis-dependent (luckily so, or else we might find that our results make no physical sense). However, the way the simulations are set up prevents a simple comparison between the results in two bases. That is, the physics of the underlying processes are ever so slightly different.

Consider first the population dynamics in local basis: this involves the excitation of a single chromophore. This excitation will be transported to other chromophores, and eventually the system will arrive at a thermal equilibrium, which is the same for all possible bases. In average eigenbasis, the highest-energy average eigenstate will be excited, which is (on average) the state that light will couple to. Over time, the system will again find thermal equilibrium. The final states might be the same, but the initial conditions, and thus the dynamics, will not be.

3.6.2 Computational artifacts

There are two issues that arise in the NISE-DBa method. The first of these is the quick transport between individual chromophores around $t = 0$, which shows approximately linear behaviour, rather than quadratic as expected. This is likely to be caused by the possibility of small denominators in Eq. (2.75). This only (noticeably) occurs in local basis, which can happen because two sites can temporarily be very close in energy. This brings the wavefunction coefficients in adiabatic basis close together, yielding a small denominator. It might be necessary to find an alternative formulation to reproduce the high-temperature results.

The second is that larger-than-dimer systems can have crossings between adiabatic states. This makes it difficult to keep track of the adiabatic states, which is necessary to correctly compute the time evolution with NISE-DBa. Current methods of tracking these states might allow small errors, yielding very ‘noisy’ data such as in Fig. 3.14. If a better method exists, it might be useful to look into. Otherwise, the only option will be to reduce the timestep, since this allows tracking individual states more easily. A more detailed explanation is given in Appendix B.

3.6.3 Computational cost

A quick evaluation of the computational cost of the new methods is in order. In principle, there is a small difference between the two NISE-DB methods, giving a slight edge to the NISE-DBb method (as previously mentioned by Bastida *et al.* in Ref. 5).

NISE-DBa

The NISE-DBa method requires two matrix diagonalisations. The first finds the basis functions of the adiabatic basis at any particular timestep, and the energies associated with these basis functions. From this, it is possible to calculate the nonadiabatic couplings and their thermal corrections. However, a second matrix diagonalisation is needed, because the nonadiabatic couplings still need to be exponentiated. As such, the algorithm requires two eigenvalue decompositions of order $\mathcal{O}(N^3)$.

NISE-DBb

In principle, NISE-DBb allows the computation of the average Hamiltonian outside of the main loop of the NISE algorithm, meaning that it need only be exponentiated once. What remains is exponentiating the (corrected) perturbation at every timestep. This means that the computational cost of NISE-DBb is slightly smaller than that of NISE-DBa. However, since this is a simple factor and not a scaling effect, it will not cause drastic differences in computational cost.

Chapter 4

Conclusion

This chapter will cover the conclusions of this work. In the first section, we will talk about the interpretation of the results. In the second section, we will talk about the possible improvements that can be made on the different methods. In the third section, we will finish off by talking about the possible implications of this work.

4.1 Interpretation of the results

In this work, a comparison was made of two different perturbative finite-temperature methods to describe open quantum systems, named NISE-DBa and NISE-DBb (Numerical Integration of the Schrödinger Equation with Detailed Balance, versions a and b). NISE-DBa uses a thermal correction to the nonadiabatic couplings, whereas NISE-DBb corrects the perturbations in average eigenbasis, i.e. the basis associated with the idealised excitonic states of a system. Both methods are designed to improve the finite-temperature calculations of NISE, which is originally temperature-agnostic but provides much better scaling with system size than the Hierarchical Equations of Motion (HEOM). Although both methods have been implemented and tested before (albeit under different names and with slight adjustments) [5, 46–48], this research is, to the best of our knowledge, the first to compare both versions in quantum parameter regimes that are relevant to light-harvesting systems.

The NISE-DBb method, first introduced by Bastida *et al.* in Ref. 5 and modified by Aghtar *et al.* in Ref. 47, has been tested extensively, albeit under the name of the Ehrenfest method, while the supposed quantum feedback due to the Hellmann-Feynman forces has been neglected. The NISE-DBa method, implemented by Bastida *et al.* in Ref. 46 and modified by Nijjar *et al.* in Ref. 48 (there named Ehrenfest-DDB, or the

Ehrenfest method with decoherence and detailed balance). In order to be able to compare the results of the two methods on equal footing, we modified the NISE-DBa method to recover high-temperature results using the approach in Ref. 47 and described in Section 2.3.6.

This work provides insight into how the results of the two methods compare to HEOM, which is considered a 'gold standard' for quantum dynamics simulations, and whose results have been compared to experimental data, albeit not very thoroughly (see Section 1.4.1).

In the high-temperature limit, the methods all show the same behaviour, owing to the high-temperature correction proposed by Aghtar *et al.* in Ref. 47.

Comparing the results side-by-side for a few systems, including FMO, LH2 and the amide I to amide II relaxation, and some artificial systems shows that both methods provide a significant gain in accuracy over NISE without detailed balance. Depending on the system, picking either NISE-DBa or NISE-DBb can have an advantage over the other.

Due to the perturbative nature of both methods, NISE-DBa works best in situations where the energies fluctuate slowly (i.e. at or near the *static limit*). NISE-DBb works best in case the Hamiltonian can be approximated by its average (i.e. when the width of the energetic disorder is small compared to the other energetic parameters, i.e. the energy difference between individual chromophores, and the couplings).

4.2 The next steps for NISE-DB

Generalisation of the NISE-DB methods to larger-scale systems appears to work adequately. However, additional performance enhancements are possible for both the NISE-DBa and NISE-DBb methods. Both methods are hampered by the possibility of a small denominator in the thermal correction of the perturbations, which can lead to unphysically fast decoherence. In addition, the need to keep track of adiabatic basis populations in the case of NISE-DBa leads to slightly worse performance (read: faster decoherence and more noisy results) for larger systems. A routine that manages to correctly preserve the physics, regardless of the system, needs to be developed in order to fix this problem.

The next step in verifying the effectiveness of the detailed balance schemes for NISE is to use them to compute observables such as absorption spectra, and in particular 2D spectra. If the spectra simulated using the NISE-DB methods come close to experimental spectra, or those generated with HEOM, we know that we have a model whose physics can describe actual observations. Being able to do so with relatively little computational effort will prove to be useful in discovering the underlying physics in large-scale biological systems.

4.3 The future in semi-classical models

The current developments in computationally cheap methods of simulating open quantum systems show that no method is foolproof, and none of the newly proposed methods exactly reflect reality. However, having methods that closely match the results of HEOM, but which use only a fraction of the computational resources, will be beneficial in the discovery of the working of light harvesting systems. The relative computational time gain achieved by these methods may prove to speed up the search for potential artificial light harvesting systems, which might otherwise be impossible, due to the large number of potential systems that need to be investigated. Additionally, the scale of the systems that can be studied will increase, as the scaling of NISE and the NISE-DB methods with respect to system size is very favourable.

If we can deduce the factors that are important for efficient exciton transport, we will not only learn how nature has developed efficient light harvesting systems, but also how to mimic nature and build organic electronics and artificial light harvesting systems, paving the way for clean and abundant energy production.

Chapter 5

Contributions

For this work, I have made use of the NISE_2017 code [64–68] written by Thomas la Cour Jansen. Contributions to the code have been previously made by Floris P. Westerman. I have also made use of the PHI software [44] for the HEOM calculations.

I have personally contributed the thermal corrections, NISE_DBa and NISE_DBb routines, and performed all the simulations (HEOM, NISE and NISE-DB) shown in this work.

Chapter 6

Acknowledgement

A long year has come to a close, and this work and research have gone through many iterations. First of all, I am very thankful to Thomas la Cour Jansen, my supervisor, who has always entertained my many questions, but also provided pivotal feedback and helped me keep my head on the rails and get this project finished.

Next, I would like to thank all the members of the Theory of Condensed Matter research group, with a special shout-out to Teun Zijp, Vesna Eric and Gijsbert ten Hoven for helping me through my presentation by sparring about the actual story I was going to tell. I also greatly appreciate Tenzin Kunsel's and Gijsbert's feedback on this more-than-60-page work. As for the rest of the research group: this work is not something that could have been accomplished in isolation. The social contact was essential in keeping me sane, and I thank you all for the many interesting talks and discussions we have had over the past year and a half.

Very importantly, I would like to thank my 'clan': my birth and found family. In particular: Aoibhin, for being incredibly supportive during the long days spent working on this manuscript, my sister and Amara, for always listening without judgement, and my mother, for giving me the metaphorical kicks in the behind that I needed to get this thing done.

Lastly, I would like to thank the reader for their interest in this work, an object of my pride and dedication.

Appendix A

Mathematical proofs and derivations

Here, we will lightly touch on some of the proofs that underlie some of the assumptions in this chapter. Some of these, such as Fermi's Golden Rule and the adiabatic theorem, can be found in (introductory) texts on quantum mechanics [3], but they have been compiled here for brevity.

The first section will cover the Langevin equation. In the second section, we will cover Fermi's Golden Rule. The third section is about the adiabatic theorem. In the fourth section, we will cover the different definitions of the nonadiabatic couplings used, and show that they are equivalent. The fifth section covers the formal derivation of the so-called 'quantum correction' or thermal correction used in this work.

A.1 Solving the Langevin equation

The Langevin equation, as given before in (2.16), is as follows:

$$\dot{v}(t) = -\frac{\gamma}{m}v(t) + \xi(t) \tag{A.1}$$

We will look at its solution, following the methods outlined in Ref. 55.

The random force $f(t)$ has a Gaussian distribution centered on zero, which is considered to be white noise:

$$\langle f_i(t) \rangle = 0 \tag{A.2}$$

$$\langle f_i(t) f_j(t') \rangle = g\delta_{ij}\delta(t - t') \tag{A.3}$$

where the delta function δ_{ij} indicates that the forces on different bath variables are completely uncorrelated, and $\delta(t-t')$ indicates that the noise is white in nature. The 'strength'

g has yet to be determined, but is considered to be the standard deviation of the random variable. From Eq. (2.16) we can infer that

$$\langle \xi_i(t)\xi_j(t')\rangle = \frac{g}{m^2}\delta_{ij}\delta(t-t') \tag{A.4}$$

In finding g, we will derive the fluctuation-dissipation theorem for overdamped Brownian motion. The first step is to find the Green function for Eq. (2.16), which is

$$G(t,t') = e^{-\frac{\gamma}{m}(t-t')}\Theta(t-t') \tag{A.5}$$

where $\Theta(t)$ is the Heaviside step function. The solution for $v(t)$ is

$$v(t) = \int\limits_{-\infty}^{\infty} \mathrm{d}t' e^{-\frac{\gamma}{m}(t-t')}\Theta(t-t')\xi(t') \tag{A.6}$$

and substituting $t_1 = t - t'$ yields

$$v(t) = \int\limits_{-\infty}^{\infty} \mathrm{d}t_1 e^{-\frac{\gamma}{m}t_1}\Theta(t_1)\xi(t-t_1) = \int\limits_{0}^{\infty} \mathrm{d}t_1 e^{-\gamma t_1}\xi(t-t_1) \tag{A.7}$$

The expectation value $\langle v^2\rangle$ is then given as

$$\begin{aligned} \langle v^2(t)\rangle &= \int_0^\infty \mathrm{d}t_1 \int_0^\infty \mathrm{d}t_2 e^{-\frac{\gamma}{m}(t_1+t_2)} \left\langle \xi(t-t_1)\xi(t-t_2)\right\rangle && \text{(A.8)} \\ &= \tfrac{g}{m^2} \int_0^\infty \mathrm{d}t_1 \int_0^\infty \mathrm{d}t_2 e^{-\frac{\gamma}{m}(t_1+t_2)}\delta(t_1-t_2) && \text{(A.9)} \\ & && \text{(A.10)} \end{aligned}$$

whose result is

$$\langle v^2(t)\rangle = \frac{g}{2\gamma m} \tag{A.11}$$

Using the equipartition theorem in one dimension, we know that

$$\langle v^2(t)\rangle = \frac{k_B T}{m} \tag{A.12}$$

and equating the last two equations gives

$$g = 2\gamma k_B T \tag{A.13}$$

This is the simplest form of the fluctuation-dissipation theorem [55]: the size of the fluctuations is proportional to the friction (dissipation) in the system.

A.2 Fermi's Golden Rule

We can use a short derivation to compute the transition rates between states in perturbation theory, which is given in Ref. 2. Given a wavefunction $|\Psi(t)\rangle$ which is defined as follows

$$|\Psi(t)\rangle = \sum_n c_n(t) \left|\psi_n\right\rangle e^{-\frac{i}{\hbar}E_n t} \tag{A.14}$$

and a Hamiltonian $H(t) = H^0 + V(t)$ whose the time-dependence is considered to be fully contained in the perturbing potential $V(t)$, we can use the Schrödinger equation, Eq. (2.1), to find

$$\sum_n c_n(t)H(t) \left|\psi_n\right\rangle e^{-\frac{i}{\hbar}E_n t} = i\hbar \sum_n \left[\dot{c}_n(t) \left|\psi_n\right\rangle - \frac{i}{\hbar}E_n c_n(t) \left|\psi_n\right\rangle\right] e^{-\frac{i}{\hbar}E_n t} \tag{A.15}$$

where we can bring the last term on the right over to the left-hand side to get

$$\sum_n c_n(t) e^{-\frac{i}{\hbar}E_n t} V(t) \left|\psi_n\right\rangle = i\hbar \sum_n \dot{c}_n(t) \left|\psi_n\right\rangle e^{-\frac{i}{\hbar}E_n t} \tag{A.16}$$

and multiply by $\langle\psi_m|$ on both sides to get

$$\sum_n V_{mn}(t) c_n(t) e^{-\frac{i}{\hbar}E_n t} = i\hbar \sum_n \dot{c}_n(t) \delta_{nm} e^{-\frac{i}{\hbar}E_n t} = i\hbar \dot{c}_m(t) e^{-\frac{i}{\hbar}E_m t} \tag{A.17}$$

where we have used $V_{mn} = \langle\psi_m|V(t)|\psi_n\rangle$ and $\langle\psi_m|\psi_n\rangle = \delta_{mn}$. We can rewrite it as follows

$$\dot{c}_m(t) = -\frac{i}{\hbar} \sum_n V_{mn}(t) c_n(t) e^{i\omega_{mn} t} \tag{A.18}$$

where $\omega_{mn} = \frac{E_m - E_n}{\hbar}$.

In most physical cases, the diagonal elements of $V(t)$ are zero, which comes in handy if we want to give a perturbative estimate for the populations in each of the states. In the adiabatic basis, as shown in A.3, this assumption holds because of the antisymmetry of the nonadiabatic coupling matrix.

If we now consider a two-level system with energies E_a and E_b, we get two coupled differential equations for the individual coefficients $c_a(t)$ and $c_b(t)$. Assuming that we start out with our population fully in state $|\psi_a\rangle$, we can find the transition probability perturbatively. To first order in perturbation theory, we find

$$\dot{c}_b^{(1)}(t) = -\frac{i}{\hbar} V_{ba}(t) e^{i\omega_{ba} t} \tag{A.19}$$

which can be integrated to get

$$c_b^{(1)}(t) = -\frac{i}{\hbar}V_{ba}\int_0^t \mathrm{d}t' e^{i\omega_{ba}t} = \frac{V_{ba}}{\hbar\omega_{ba}}(1 - e^{i\omega_{ba}t}) \tag{A.20}$$

where we assume that our perturbation is (at least temporarily) time-independent. Now, we can find the population in state $|\psi_b\rangle$ to first order:

$$\rho_{bb}^{(1)}(t) = |c_b^{(1)}(t)|^2 = \left|\frac{V_{ba}}{\hbar\omega_{ba}}\right|^2 (2 - 2\cos\omega_{ba}t) = \left|\frac{2V_{ba}}{\hbar\omega_{ba}}\right|^2 \sin^2\frac{\omega_{ba}t}{2} \tag{A.21}$$

For short timescales, this is proportional to t^2, so we cannot define a proper rate constant. Over long timescales, however, we can take the limit

$$\rho_{bb}^{(1)}(t) = \lim_{t\longrightarrow\infty}\left|\frac{V_{ba}}{\hbar}\right|^2 t\frac{\sin^2\Omega t}{\Omega^2 t} = \pi t\left|\frac{V_{ba}}{\hbar}\right|^2 \delta(\frac{\omega_{ba}}{2}) = \frac{2\pi|V_{ba}|^2}{\hbar^2}\delta(\omega_{ba})t \tag{A.22}$$

If we take the derivative of the previous equation, we can find the transition rate:

$$k_{b\longleftarrow a} = \frac{\partial}{\partial t}\rho_{bb}^{(1)}(t) = \frac{2\pi|V_{ba}|^2}{\hbar^2}\delta(\omega_{ba}) \tag{A.23}$$

We thus find out that $k_{n\longleftarrow m} \propto |V_{nm}|^2$ and $k_{m\longleftarrow n} \propto |V_{mn}|^2$, which is the consequence of **Fermi's Golden Rule**.

A.3 The adiabatic theorem

The adiabatic theorem is a result in time-dependent perturbation theory, where we can describe the dynamics of our system as moving on a single adiabatic surface, provided that the time dependence of our system is slow enough that we can describe the perturbations as roughly constant. It should remind the reader of the Born-Oppenheimer approximation, which assumes the time evolution of the nuclear positions occurs on much smaller timescales than the evolution of the electronic degrees of freedom. In deriving the adiabatic theorem, one usually obtains a term which is negligible under the assumption that the perturbation varies slowly [2]. In our case, however, this assumption does not hold and therefore we should keep this term.

First of all, let us assume $|\tilde{\psi}_n(t)\rangle$ is the set of eigenvectors of our Hamiltonian at time t, each with eigenvalues $\epsilon_n(t)$. This is also called the *adiabatic basis* [69].

$$H(t)\,|\tilde{\psi}_n(t)\rangle = \epsilon_n(t)\,|\tilde{\psi}_n(t)\rangle \tag{A.24}$$

We can write the original Hamiltonian $H(t)$ in its eigendecomposition as follows:

$$H(t) = C^{\dagger}(t)\tilde{H}(t)C(t) \tag{A.25}$$

Where $C(t)$ is the unitary matrix containing the Hamiltonian's eigenvectors in column form, and $C^{\dagger}(t)$ is its Hermitean conjugate. In the case of a real Hamiltonian, we can find an orthogonal $C(t)$, simplifying any calculations we might want to do.

Next, let us decompose our wavefunction $|\Psi(t)\rangle$ in adiabatic basis:

$$|\Psi(t)\rangle = \sum_n c_n(t) \, |\tilde{\psi}_n(t)\rangle \tag{A.26}$$

According to the Schrödinger equation, its time evolution is given as:

$$i\hbar \frac{\partial}{\partial t} \sum_n c_n(t) \, |\tilde{\psi}_n(t)\rangle = H(t) \sum_n c_n(t) \, |\tilde{\psi}_n(t)\rangle \tag{A.27}$$

Which can be rewritten to

$$\sum_n c_n(t)\epsilon_n(t) \, |\tilde{\psi}_n(t)\rangle = i\hbar \sum_n \left[\dot{c}_n(t) \, |\tilde{\psi}_n(t)\rangle + c_n(t) \, |\dot{\tilde{\psi}}_n(t)\rangle \right] \tag{A.28}$$

Where a dot above a variable indicates its time derivative. Remembering that our goal is to find an expression for $c_n(t)$, we would like to make this into a differential equation. Bringing all instances of $\dot{c}_n(t)$ to the left-hand side, and all instances of $c_n(t)$ to the right and multiplying by $\langle\tilde{\psi}_m(t)|$ gives us:

$$\sum_n \dot{c}_n(t) \, \langle\tilde{\psi}_m(t)|\tilde{\psi}_n(t)\rangle = -\frac{i}{\hbar} \sum_n c_n(t) \left[\epsilon_n(t) \, \langle\tilde{\psi}_m(t)|\tilde{\psi}_n(t)\rangle - i\hbar \, \langle\tilde{\psi}_m(t)|\dot{\tilde{\psi}}_n(t)\rangle \right] \tag{A.29}$$

Realising that $\langle\tilde{\psi}_m(t)|\tilde{\psi}_n(t)\rangle = \delta_{mn}$, we can rewrite it in the following form:

$$\dot{c}_m(t) = -\frac{i}{\hbar} \sum_n P_{mn}(t)c_n(t) \tag{A.30}$$

where we have defined a propagator matrix $P(t)$ combining both adiabatic and non-adiabatic behaviour, which can be written as follows:

$$P_{mn} = \epsilon_m(t)\delta_{mn} + i\hbar S_{mn}(t) \tag{A.31}$$

where $S_{mn}(t) = \langle\dot{\tilde{\psi}}_m(t)|\tilde{\psi}_n(t)\rangle$ are the *nonadiabatic couplings*, which promote transfer between adiabatic basis states. We can integrate Eq. (A.30) numerically to find

$$c_m(t + \Delta t) = \sum_n \left(e^{-\frac{i}{\hbar}P(t)\Delta t}\right)_{mn} c_n(t) \tag{A.32}$$

From their definition in Dirac notation, we can write the nonadiabatic couplings in matrix notation as follows

$$S_{mn}(t) = \dot{C}^{\dagger}_{mk}(t)C_{kn}(t) \tag{A.33}$$

where $C(t)$ is the matrix containing the eigenvectors of $H(t)$ in its columns. Since the propagator matrix needs to be Hermitean, we can infer that $i\hbar S(t)$ needs to be anti-Hermitean, i.e. $(i\hbar S(t))^{\dagger} = i\hbar S(t)$, so $S^{\dagger}(t) = -S(t)$. Moreover, since the eigenvectors of the Hamiltonian will be real, up to an arbitrary complex phase, we can infer that $S(t)$ must be real and antisymmetric.

A.3.1 An alternative nonadiabatic coupling

There is another way of defining the nonadiabatic couplings, which exploits a time derivative of the eigenvalue equation, as shown in Ref. 2:

$$\frac{\partial}{\partial t}(H(t)\,|\tilde{\psi}_n(t)\rangle) = \frac{\partial}{\partial t}(E_n(t)\,|\tilde{\psi}_n(t)\rangle) \tag{A.34}$$

which is expanded to

$$\dot{H}(t)\,|\tilde{\psi}_n(t)\rangle + H(t)\,|\dot{\tilde{\psi}}_n(t)\rangle = \dot{E}_n(t)\,|\tilde{\psi}_n(t)\rangle + E_n(t)\,|\dot{\tilde{\psi}}_n(t)\rangle \tag{A.35}$$

We can multiply on the left by $\langle\tilde{\psi}_m(t)|$ to get

$$\langle\tilde{\psi}_m(t)|\dot{H}(t)|\tilde{\psi}_n(t)\rangle + \langle\tilde{\psi}_m(t)|H(t)|\dot{\tilde{\psi}}_n(t)\rangle = \dot{E}_n(t)\,\langle\tilde{\psi}_m(t)|\tilde{\psi}_n(t)\rangle + E_n(t)\,\langle\tilde{\psi}_m(t)|\dot{\tilde{\psi}}_n(t)\rangle \tag{A.36}$$

Using the hermiticity of $H(t)$ and the orthonormality of basis vectors, we get

$$\langle\tilde{\psi}_m(t)|\dot{H}(t)|\tilde{\psi}_n(t)\rangle = \dot{E}_n(t)\delta_{nm} + (E_n(t) - E_m(t))\,\langle\tilde{\psi}_m(t)|\dot{\tilde{\psi}}_n(t)\rangle \tag{A.37}$$

and for $n \neq m$, we get

$$-S_{mn}(t) = \langle\tilde{\psi}_m(t)|\dot{\tilde{\psi}}_n(t)\rangle = \frac{\langle\tilde{\psi}_m(t)|\dot{H}(t)|\tilde{\psi}_n(t)\rangle}{E_n(t) - E_m(t)} \tag{A.38}$$

from which one can see that energy levels that are close together will yield high nonadiabatic couplings. If two energy levels in diabatic basis cross each other, the resulting nonadiabatic couplings will be the largest. We call this an *avoided crossing*, since the denominator in Eq. (A.38) will not go to zero, but it will find a minimum.

A.3.2 An extension of Fermi's Golden Rule

In the adiabatic basis, as we can see, the role of the perturbing potential is played by the nonadiabatic couplings. We can consider the substitution $V(t) = i\hbar S(t)$, and assume $S(t)$ to be constant for a short amount of time, such that we can solve our differential equations numerically. If this is the case, then it follows from Fermi's Golden Rule, Eq. (A.23), that

$$k_{m\leftarrow n} = \frac{2\pi\hbar^2|S_{mn}(t)|^2}{\hbar^2}\delta(\omega_{mn}) = 2\pi|S_{mn}(t)|^2\delta(\omega_{mn}) \tag{A.39}$$

A.4 Equivalence of nonadiabatic couplings

Among many definitions of population dynamics in the adiabatic basis, the one used by Bastida and Prezhdo [46, 48] is as follows

$$i\hbar\dot{c}_m(t) = \sum_n \big(E_m\delta_{mn} - i\hbar\vec{d}^{(1)}_{mn}\cdot\frac{\vec{P}}{M}\big)c_n(t) \tag{A.40}$$

Here, the term $-i\hbar\vec{d}^{(1)}_{mn}\cdot\frac{\vec{P}}{M}$ looks eerily like $i\hbar S_{mn}$. Let us check that the two definitions are equivalent. The definition of the nonadiabatic coupling is:

$$\vec{d}^{(1)}_{mn} = \langle\tilde{\psi}_m(\vec{r},\vec{R}(t))|\vec{\nabla}\tilde{\psi}_n(\vec{r},\vec{R}(t))\rangle \tag{A.41}$$

with $\vec{r}$ being the electronic coordinates (which we shall not consider in this derivation), $\vec{R}(t) = R_i(t)$ being the nuclear coordinates, $\vec{\nabla} = \frac{\partial}{\partial R_i}$ indicating derivatives with respect to the nuclear coordinates, and $\frac{\vec{P}}{M} = \frac{P_i}{M}$ indicating the velocities of the nuclei themselves.

The fact that $|\tilde{\psi}_m\rangle$ depends on $R_i(t)$ shows us that Without loss of generality with regards to the equation of motion of the nuclear degrees of freedom, we can state:

$$-\vec{d}^{(1)}_{mn}\cdot\frac{\vec{P}}{M} = -\langle\tilde{\psi}_n(\vec{r},\vec{R}(t))|\frac{\partial t}{\partial R_i}\frac{\partial}{\partial t}\tilde{\psi}_m(\vec{r},R_i(t))\rangle\,\frac{P_i}{M} \tag{A.42}$$

$$= -\langle\tilde{\psi}_n(t)|\dot{\tilde{\psi}}_m(t)\rangle\left(\frac{P_i}{M}\right)^{-1}\frac{P_i}{M} \tag{A.43}$$

$$= S_{mn} \tag{A.44}$$

And thus, we can conclude that these two definitions of the nonadiabatic coupling are equivalent.

A.5 Semi-classical time-correlation functions

I have covered a heuristic explanation of the thermal correction to the perturbing potential and the nonadiabatic couplings in Section 2.3.4. Now, I will touch on the basics of the original derivation of this correction, and a few of the alternatives laid out in Ref. 60.

For a complete description of our quantum system in its bath environment, we must treat the bath degrees of freedom quantum mechanically as well. That means that we consider our complete wavefunctions $|\Psi\rangle$ to be of the form

$$|\Psi\rangle = |\psi_S\rangle\,|\chi_B\rangle \tag{A.45}$$

where $|\psi_S\rangle$ are the system wavefunctions and $|\chi_B\rangle$ are the bath wavefunctions. The transition rates according to Fermi's Golden Rule given in Eq. (A.23) can now be rewritten [49, 60] by considering the bath expectation value of the transition rates:

$$k^q_{m\leftarrow n}(t) = \frac{2\pi}{\hbar^2}\sum_\alpha P(\alpha)\,\langle\alpha|\,|V_{mn}|^2\,|\alpha\rangle\,\delta\Big(\frac{E_m - E_n + E_\alpha - E_\beta}{\hbar}\Big) \tag{A.46}$$

where $P(\alpha)$ is the probability of finding the bath in state $|\alpha\rangle$, which is given by the Boltzmann factor $\frac{1}{Z}e^{-\beta E_\alpha}$, where $Z = \sum\limits_\alpha e^{-\beta E_\alpha} = \mathrm{Tr}[e^{-\beta H_B}]$ is the partition function. We can turn the delta function into an exponential as follows

$$k^q_{m\leftarrow n}(t) = \frac{1}{\hbar^2}\sum_\alpha e^{-\beta E_\alpha}\int\limits_{-\infty}^{\infty}\mathrm{d}t'\,e^{\frac{it'}{\hbar}(E_m - E_n + E_\alpha - E_\beta)}\,\langle\alpha|\,|V_{mn}|^2\,|\alpha\rangle \tag{A.47}$$

we can replace $|V_{mn}|^2$ by the symmetrical formula

$$|V_{mn}|^2 = \frac{1}{2}[V^\dagger_{nm}V_{mn} + V_{mn}V^\dagger_{nm}] \tag{A.48}$$

from which it follows that

$$k^q_{m\leftarrow n} = \frac{1}{2\hbar^2}\int\limits_{-\infty}^{\infty}\mathrm{d}t'\,e^{i\omega_{mn}t'}\sum_\alpha \frac{1}{Z}e^{-\beta E_\alpha}e^{\frac{it'}{\hbar}(E_\alpha - E_\beta)}[\langle\alpha|\,V^\dagger_{nm}V_{mn} + V_{mn}V^\dagger_{nm}\,|\alpha\rangle] \tag{A.49}$$

where we can insert a complete set of states $\sum\limits_\beta |\beta\rangle\langle\beta| = 1$ to turn the sum over α into a double sum:

$$\sum_{\alpha,\beta} \frac{1}{Z} e^{-\beta E_\alpha} e^{\frac{it'}{\hbar}(E_\alpha - E_\beta)} [\langle\alpha| V^\dagger_{nm} |\beta\rangle \langle\beta| V_{mn} |\alpha\rangle + \langle\alpha| V_{mn} |\beta\rangle \langle\beta| V^\dagger_{nm} |\alpha\rangle] \tag{A.50}$$

$$= \sum_{\alpha,\beta} \frac{1}{Z} e^{-\beta E_\alpha} [\langle\alpha| e^{\frac{i}{\hbar}H_B t} V^\dagger_{nm} e^{-\frac{i}{\hbar}H_B t} |\beta\rangle \langle\beta| V_{mn} |\alpha\rangle + \langle\alpha| e^{\frac{i}{\hbar}H_B t} V_{mn} e^{-\frac{i}{\hbar}H_B t} V^\dagger_{nm} |\beta\rangle \langle\beta| V_{mn} |\alpha\rangle] \tag{A.51}$$

$$= \sum_{\alpha} \frac{1}{Z} e^{-\beta E_\alpha} [\langle\alpha| V^\dagger_{nm}(t') V_{mn}(0) + V_{mn}(t') V^\dagger_{nm}(0) |\alpha\rangle] = G_{mn}(t) \tag{A.52}$$

where $G(t)$ is the quantum time-correlation function (TCF) of the perturbing potential, which is defined as

$$G_{mn}(t) = \frac{1}{2}\big[\, \langle V^\dagger_{nm}(t) V_{mn}(0)\rangle + \langle V_{mn}(t) V^\dagger_{nm}(0)\rangle \,\big] \tag{A.53}$$

where

$$\langle V^\dagger_{nm}(t) V_{mn}(0)\rangle = \frac{\mathrm{Tr}[e^{-\beta H_B} V^\dagger_{nm}(t) V_{mn}(0)]}{\mathrm{Tr}[e^{-\beta H_B}]} \tag{A.54}$$

whose numerator must obey a few time symmetries. First, we must be aware of the relation

$$\begin{aligned} \mathrm{Tr}[e^{-\beta H_B} V^\dagger_{mn}(t) V_{mn}(0)] &= \mathrm{Tr}[e^{-\beta H_B} e^{\frac{it}{\hbar}H_B} V^\star_{nm}(0) e^{-\frac{it}{\hbar}H_B} V_{mn}(0)] && \text{(A.55)}\\ &= \mathrm{Tr}[e^{-\beta H_B} V^\star_{nm}(0) e^{-\frac{it}{\hbar}H_B} V_{mn}(0) e^{\frac{it}{\hbar}H_B}] && \text{(A.56)}\\ &= \mathrm{Tr}[e^{-\beta H_B} V^\star_{nm}(0) V_{mn}(-t)] && \text{(A.57)} \end{aligned}$$

where we exploit the cyclic property of the trace and write $V_{mn}(t) = e^{\frac{it}{\hbar}H_B} V_{mn}(0) e^{-\frac{it}{\hbar}H_B}$ in the Heisenberg picture. I have also assumed that $V_{mn}(t)$ is an operator on the bath coordinates. One can now perform the following manipulation:

$$\langle V^\dagger_{nm}(-t) V_{mn}(0)\rangle = \frac{\mathrm{Tr}[e^{-\beta H_B} e^{-\frac{it}{\hbar}H_B} V^\dagger_{nm}(0) e^{\frac{it}{\hbar}H_B} V_{mn}(0)]}{\mathrm{Tr}[e^{-\beta H_B}]} = \frac{\mathrm{Tr}[e^{-\beta H_B} V_{mn}(t) V^\dagger_{nm}(0)]}{\mathrm{Tr}[e^{-\beta H_B}]} \tag{A.58}$$

where I used the cyclic property of the trace, and a little sleight of hand with Eq. (A.55) yields the relations

$$G_{mn}(-t) = G^\star_{mn}(t) = G_{mn}(t - i\beta\hbar) \tag{A.59}$$

The first equality makes sure that the TCF consists of a real, symmetric part and an imaginary, antisymmetric part. The second ensures that the TCF obeys detailed balance, as will become clear when looking at the Fourier transform of the TCF:

$$\hat{G}_{mn}(\omega) = \int_{-\infty}^{\infty} \mathrm{d}t\, e^{i\omega t} G_{mn}(t) \tag{A.60}$$

which has the property

$$\hat{G}_{mn}(-\omega) = \int_{-\infty}^{\infty} \mathrm{d}t\, e^{-i\omega t} G_{mn}(t) = \int_{-\infty}^{\infty} \mathrm{d}t' e^{i\omega t'} G_{mn}(-t') \tag{A.61}$$

$$= \int_{-\infty}^{\infty} \mathrm{d}t' e^{i\omega t'} G_{mn}(t' - i\beta\hbar) = \int_{-\infty}^{\infty} \mathrm{d}t'' e^{i\omega(t'' + i\beta\hbar)} \tag{A.62}$$

$$= \int_{-\infty}^{\infty} e^{-\beta\hbar\omega} \int_{-\infty}^{\infty} \mathrm{d}t'' e^{i\omega t''} G(t'') = e^{-\beta\hbar\omega} \hat{G}_{mn}(\omega) \tag{A.63}$$

which means that the rate constants indeed satisfy detailed balance.

The challenge in carrying over the detailed balance to the semi-classical approximation, lies in finding the quantum TCF. Since taking the trace over the bath variables is not a viable option in the case of large systems, some other solution is needed. As said before, $G(t)$ can be split up into $G_R(t)$, a real, symmetric part, and $iG_I(t)$, an imaginary antisymmetric part.

$$G(t) = G_R(t) + iG_I(t) \tag{A.64}$$

whose symmetries are proven by the following equation:

$$G(-t) = G_R(-t) + iG_I(-t) = G^\star(t) = G_R(t) - iG_I(t) \tag{A.65}$$

The Fourier transform of the TCF can also be rewritten:

$$\hat{G}(\omega) = \hat{G}_S(\omega) + \hat{G}_A(\omega) \tag{A.66}$$

where

$$\hat{G}_S(\omega) = \int_{-\infty}^{\infty} \mathrm{d}t\, e^{i\omega t} G_R(t) \tag{A.67}$$

and

$$\hat{G}_A(\omega) = i \int_{-\infty}^{\infty} \mathrm{d}t\, e^{i\omega t} G_I(t) \tag{A.68}$$

which are the symmetric and antisymmetric contributions, respectively. Using the detailed balance time symmetry (Eq. (A.63)) one gets

$$\hat{G}(-\omega) = \hat{G}_S(-\omega) + \hat{G}_A(-\omega) = \hat{G}_S(\omega) - \hat{G}_A(\omega) = e^{-\beta\hbar\omega} \hat{G}(\omega) \tag{A.69}$$

$$= e^{-\beta\hbar\omega} [\hat{G}_S(\omega) + \hat{G}(\omega)] \tag{A.70}$$

which yields the relation

$$\hat{G}_A(\omega) = \left(\frac{1-e^{-\beta\hbar\omega}}{1+e^{-\beta\hbar\omega}}\right)\hat{G}_S(\omega) = \left(\frac{e^{\frac{\beta\hbar\omega}{2}} - e^{-\frac{\beta\hbar\omega}{2}}}{e^{\frac{\beta\hbar\omega}{2}} + e^{-\frac{\beta\hbar\omega}{2}}}\right)\hat{G}_S(\omega) = \tanh\left(\frac{\beta\hbar\omega}{2}\right)\hat{G}_S(\omega) \tag{A.71}$$

or, alternatively,

$$\hat{G}(\omega) = \left(1 + \frac{1-e^{-\beta\hbar\omega}}{1+e^{-\beta\hbar\omega}}\right)\hat{G}_S(\omega) = \left(\frac{2}{1+e^{-\beta\hbar\omega}}\right)\hat{G}_S(\omega) = \left(\frac{2}{1-e^{-\beta\hbar\omega}}\right)\hat{G}_A(\omega) \tag{A.72}$$

It is possible to find a relation between $G_R(t)$ and $G_I(t)$ by taking the inverse Fourier transform of the series expansion of $\hat{G}_A(\omega)$:

$$G_I(t) = \int\limits_{-\infty}^{\infty} \mathrm{d}\omega\, e^{-i\omega t} \tanh\left(\frac{\beta\hbar\omega}{2}\right)\hat{G}_S(\omega) = \int\limits_{-\infty}^{\infty} \mathrm{d}\omega\, e^{-i\omega t} \sum_n \frac{a_n}{n!}\left(\frac{\beta\hbar\omega}{2}\right)^n \hat{G}_S(\omega) \tag{A.73}$$

where we can exploit the fundamental theorem of calculus to get

$$G_I(t) = \sum_n \frac{a_n}{n!}\left(\frac{i\beta\hbar\frac{\partial}{\partial t}}{2}\right)^n \int\limits_{-\infty}^{\infty} \mathrm{d}\omega\, e^{-i\omega t}\hat{G}_S(\omega) = \tan\left(\frac{\beta\hbar\frac{\partial}{\partial t}}{2}\right) G_R(t) \tag{A.74}$$

There are different ways of solving the relation in Eq. (A.74). The first is to decompose $G(t)$ into a Taylor series in $\hbar$ and to take the limit as $\hbar \to 0$.

$$G_I(t) = \tan\left(\frac{\beta\hbar}{2}\frac{\partial}{\partial t}\right) G_R(t) \approx \frac{\beta\hbar}{2}\frac{\partial}{\partial t} G_R(t) \tag{A.75}$$

$$\lim_{\hbar\to 0} G(t) = \lim_{\hbar\to 0} G_R(t) + i\lim_{\hbar\to 0} G_I(t) = \lim_{\hbar\to 0} G_R(t) = G_{cl}(t) \tag{A.76}$$

Where $\lim\limits_{\hbar\to 0} G_I(t) = 0$. The semi-classical (or *standard*) approximation then takes $G_R(t) \approx G_{cl}(t)$, which means that using Eq. (A.72) we have

$$\hat{G}(\omega) = \left(\frac{2}{1+e^{-\beta\hbar\omega}}\right)\hat{G}_{cl}(\omega) \tag{A.77}$$

Taking the Fourier transform of Eq. (A.75), we find

$$\hat{G}_A(\omega) = i\frac{\beta\hbar}{2}\int\limits_{-\infty}^{\infty} \mathrm{d}t\, e^{i\omega t}\frac{\partial}{\partial t}G_R(t) = \frac{\beta\hbar\omega}{2}\int\limits_{-\infty}^{\infty} \mathrm{d}t\, e^{i\omega t} G_R(t) + \lim_{T\to\infty}\left[e^{i\omega t}G_R(t)\right]_{-T}^{T} \tag{A.78}$$

$$= \frac{\beta\hbar\omega}{2}\hat{G}_{cl}(\omega) \tag{A.79}$$

where we have used the fact that $G_R(t)$ is symmetric and $G_R(t) \approx G_{cl}(t)$. The next step is to take Eq. (A.72) and say

$$\hat{G}(\omega) = \left(\frac{2}{1 - e^{-\beta\hbar\omega}} \right) \frac{\beta\hbar\omega}{2} \hat{G}_{cl}(t) = \left(\frac{\beta\hbar\omega}{1 - e^{-\beta\hbar\omega}} \right) \hat{G}_{cl}(\omega) \tag{A.80}$$

which is called the *harmonic approximation* [60]. We can use this to postulate another thermal correction to the perturbing potential or the nonadiabatic couplings. Following the guidelines in 2.3.7, the thermal correction to the perturbing potential should be

$$\tilde{V}_{mn}(t) = \frac{V_{mn}(t)}{|c_n(t)| - |c_m(t)|} \left[\sqrt{\frac{\beta E_{mn}}{1 - e^{-\beta E_{mn}}}} |c_n(t)| - \sqrt{\frac{\beta E_{nm}}{1 - e^{-\beta E_{nm}}}} |c_m(t)| \right] \tag{A.81}$$

and the correction to the nonadiabatic coupling:

$$\tilde{S}_{mn}(t) = S_{mn}(t) \left[\sqrt{\frac{\beta E_{mn}}{1 - e^{-\beta E_{mn}}}} |c_n(t)| - \sqrt{\frac{\beta E_{nm}}{1 - e^{-\beta E_{nm}}}} |c_m(t)| \right] \tag{A.82}$$

Appendix B

Explanation of the computational tools

For this work, a new subroutine was developed for the NISE_2017 [64–68] code.

For an explanation on how to use the NISE_2017 code, the reader is referred to its official GitHub repository. Before you can get started using the code, you must first 'build' it. Instructions for this can be found in the user manual. The new code can be found in my personal GitHub repository.

B.1 File structure and building

The file structure of the repository is as follows (after following the 'build' instructions in the user manual):

```
NISE_2017
|
|-examples
|  |
|  |--dimer
|  |--tutorial
|  |--trimer
|
|-build
|-other directories, such as src
```

Before you can start using the example systems, you must build the ‘stochastic_general’ code, which can generate an arbitrarily large Hamiltonian with random, uncorrelated dynamic disorder. You do this by navigating to the ‘build’ directory and using the command ‘make examples’. This generates the ‘stochastic_general’ program in the ‘tutorial’ directory.

B.2 Generating the Hamiltonian

To create the input files, you must use the ‘stochastic_general’ code. The arguments that need to be passed to this program are: Length (the number of snapshots), the timestep in fs, the width (standard deviation) of the dynamic disorder in cm^{-1}, the bath correlation time in fs, the correlation angle of the dipoles (which is not important for the PopT2 routine but the program structure still requires us to supply a Dipole file, hence we must fill in something here), and the Hamiltonian in cm^{-1}.

For the latter, the upper triangle of the Hamiltonian is passed. The Hamiltonian is assumed to be real-valued. To reproduce the results in this work, a time-averaged Hamiltonian such as in Eq. (B.1) must be entered as ‘0 200 100’, with the highest diagonal element going first. The design choice was made to keep consistency between results in different bases: the eigenstates are put in ascending order by their energies, and therefore it makes sense to put the highest-energy chromophore last as well.

$$H_0 = \begin{pmatrix} 100 & 200 \\ 200 & 0 \end{pmatrix} \mathrm{cm}^{-1} \tag{B.1}$$

B.3 The NISE input files

The following changes are necessary in NISE_2017 to make use of the NISE_DBa and NISE_DBb. First, the keyword ‘Technique’ needs to be followed by ‘PopT2’. Next, the keyword ‘Basis’ needs to be followed by ‘Local’, ‘Average’ (for average eigenbasis) or ‘Adiabatic’. Additionally, the temperature can set with the keyword ‘Temperature’, followed by the temperature in Kelvin.

For every execution of the code, two output files are generated in txt format. One contains the populations of the wanted state (highest-energy chromophore, average eigenstate or adiabatic state), the other contains the absolute value of the coherence between the highest and second highest-energy chromophores or eigenstates.

B.4 The tutorial files

The directories ‘dimer’ and ‘trimer’ contain two separate examples. The first, ‘dimer’, contains a file ‘run.sh’ that generates a Hamiltonian trajectory, which is turned into a binary file. The default average Hamiltonian is:

$$H = \begin{pmatrix} 100 & 100 \\ 100 & 0 \end{pmatrix} \text{cm}^{-1} \tag{B.2}$$

The width of the dynamic disorder is $100\,\text{cm}^{-1}$, and its bath correlation time is 100 fs. The second, ‘trimer’, contains a similarly named file. Its default Hamiltonian is:

$$H = \begin{pmatrix} 100 & 100 & 100 \\ 100 & 0 & 100 \\ 100 & 100 & -100 \end{pmatrix} \text{cm}^{-1} \tag{B.3}$$

The width of the dynamic disorder and the bath correlation time are the same as for the ‘dimer’ tutorial file. To perform the NISE(-DB) calculations, you have to run the command ‘../../bin/NISE inputPop’. The files ‘inputPop’ contain the necessary settings to run the population dynamics in average eigenbasis.

B.5 The ‘swaps’ routine

A problem with NISE-DBa is that it makes use of a routine that keeps track of the order of the adiabatic states. In a two-level system, this is an easy task, since the eigenvalues always stay separated by an amount $2J$. This changes in trimers and larger systems.

Let us consider a trimer system with a Hamiltonian as given in Eq. (B.4), whose Hilbert space contains two invariant subspaces (i.e. the Hamiltonian is block diagonal with two blocks).

$$H = \begin{pmatrix} \sigma x_1(t) + V & V & 0 \\ V & \sigma x_2(t) & 0 \\ 0 & 0 & \sigma x_3(t) \end{pmatrix} \tag{B.4}$$

where V and σ are arbitrary energies, and $x_i(t)$ where $i \in \{1, 2, 3\}$ are dimensionless, normally distributed random variables with zero mean. Since the Hamiltonian is block-diagonal, the third eigenvalue is going to be equal to $\sigma x_3(t)$ at any point in time. This means that this eigenvalue can cross in between the two eigenvalues of the upper left block. The eigendecomposition algorithms pay this no heed, and the eigenvalues and eigenvectors associated with the two invariant subspaces get mixed as a result. This would not be a problem in the original NISE implementation, as this mixing only plays a role in the nonadiabatic couplings. Since NISE does not adjust the nonadiabatic couplings, the physics remain the same, even if the order of the eigenvectors is changed.

The problem arises in NISE-DBa, where the nonadiabatic couplings are changed. A mixing in the eigenvectors between times t and $t + \mathrm{d}t$ means that the off-diagonal elements of $\dot{C}^\dagger(t + \mathrm{d}t)C(t)$, and therefore the nonadiabatic couplings, between the different invariant subspaces becomes very large. The thermal correction thus corrects a very large (unphysical) nonadiabatic coupling, yielding unphysical results in the transport. Suddenly, seemingly impossible transport between particular adiabatic states can occur. This must be prevented, which can be done by tracking the individual eigenstates.

The routine is performed at every timestep. It starts by multiplying the matrix eigenvectors at the next timestep $C^\dagger(t + \mathrm{d}t)$, by the eigenvectors at the current timestep $C(t)$, as follows: $C^\dagger(t + \mathrm{d}t)C(t)$. If the change in eigenstates is small enough, this matrix will be close to identity. If two eigenvectors have suddenly swapped places, there will be large off-diagonal components in this matrix. As a benchmark, the largest off-diagonal component (LODC) is compared to the smallest diagonal component (SDC). If the SDC is smaller than the LODC, this is a strong indication that two eigenvectors have swapped places. The coordinates of the LODC are denoted (i, j). To finish off, the eigenvalues at indices i and j are swapped, and so are the column vectors of $C(t + \mathrm{d}t)$.

Bibliography

[1] C.P. van der Vegte, J.D. Prajapati, U. Kleinekathöfer, J. Knoester and T.L.C. Jansen. *J. Phys. Chem. B*, **119**(4):1302–1313, (January 2015).

[2] J.J. Sakurai and J. Napolitano. *Modern Quantum Mechanics.* Cambridge University Press, second edition, 2017.

[3] D.F. Schroeter and D.J. Griffiths. *Introduction to Quantum Mechanics.* Cambridge University Press, third edition, 2018.

[4] T.L.C. Jansen. *J. Phys. Chem. A*, **122**(1):172–183, (January 2018).

[5] A. Bastida, C. Cruz, J. Zúñiga, A. Requena and B. Miguel. *Chem. Phys. Lett.*, **417**(1):53–57, (January 2006).

[6] G.D. Scholes, G.R. Fleming, A. Olaya-Castro and R. van Grondelle. *Nat. Chem.*, **3**(10):763–774, (October 2011).

[7] N.S. Lewis and D.G. Nocera. *Proc. Natl. Acad. Sci.*, **103**(43):15729–15735, (October 2006).

[8] C.B. Field, M.J. Behrenfeld, J.T. Randerson and P. Falkowski. *Science*, **281**(5374):237–240, (July 1998).

[9] R.E. Blankenship. *Plant Physiol.*, **154**(2):434–438, (October 2010).

[10] A.E. Becquerel. Recherche sur les effets de la radiation chimique de la lumière solaire, au moyen des courants électriques. *Comptes rendus hebdomadaires des séances de l'Académie des sciences*, volume 9, pages 145–149.
Académie des sciences (France), (1839).

[11] R.E. Blankenship, D.M. Tiede, J. Barber, G.W. Brudvig, G. Fleming, M. Ghirardi, M.R. Gunner, W. Junge, D.M. Kramer, A. Melis, T.A. Moore, C.C. Moser, D.G. Nocera, A.J. Nozik, D.R. Ort, W.W. Parson, R.C. Prince and R.T. Sayre. *Science*, **332**(6031):805–809, (May 2011).

[12] A. Melis. *Plant Sci.*, **177**(4):272–280, (October 2009).

[13] N.R. Baker. *Annu. Rev. Plant Biol.*, **59**(1):89–113, (2008).

[14] W. Sakamoto. *Annu. Rev. Plant Biol.*, **57**(1):599–621, (2006).

[15] R.R. Choubeh, R.B.M. Koehorst, D. Bína, P.C. Struik, J. Pšenčík and H. van Amerongen. *Biochim. Biophys. Acta Bioenerg.*, **1860**(2):147–154, (February 2019).

[16] S. Scheuring and J.N. Sturgis. *Science*, **309**(5733):484–487, (July 2005).

[17] A.S. Bondarenko, J. Knoester and T.L.C. Jansen. *Chem. Phys.*, **529**:110478, (January 2020).

[18] P. Ball. *Nature*, **474**(7351):272–274, (June 2011).

[19] G.S. Engel, T.R. Calhoun, E.L. Read, T.K. Ahn, T. Mančal, Y.C. Cheng, R.E. Blankenship and G.R. Fleming. *Nature*, **446**(7137):782–786, (April 2007).

[20] H. Lee, Y.C. Cheng and G.R. Fleming. *Science*, **316**(5830):1462–1465, (June 2007).

[21] G. Panitchayangkoon, D. Hayes, K.A. Fransted, J.R. Caram, E. Harel, J. Wen, R.E. Blankenship and G.S. Engel. *Proc. Natl. Acad. Sci.*, **107**(29):12766–12770, (July 2010).

[22] R. Tempelaar, T.L.C. Jansen and J. Knoester. *J. Phys. Chem. B*, **118**(45):12865–12872, (November 2014).

[23] E. Thyrhaug, R. Tempelaar, M.J.P. Alcocer, K. Žídek, D. Bína, J. Knoester, T.L.C. Jansen and D. Zigmantas. *Nat. Chem.*, **10**(7):780–786, (July 2018).

[24] J. Cao, R.J. Cogdell, D.F. Coker, H.G. Duan, J. Hauer, U. Kleinekathöfer, T.L.C. Jansen, T. Mančal, R.J.D. Miller, J.P. Ogilvie, V.I. Prokhorenko, T. Renger, H.S. Tan, R. Tempelaar, M. Thorwart, E. Thyrhaug, S. Westenhoff and D. Zigmantas. *Sci. Adv.*, **6**(14):eaaz4888, (April 2020).

[25] A.S. Davydov. *Sov. Phys. Usp.*, **7**(2):145, (February 1964).

[26] S.K. Saikin, A. Eisfeld, S. Valleau and A. Aspuru-Guzik. *Nanophotonics*, **2**(1):21–38, (February 2013).

[27] T. Brixner, R. Hildner, J. Köhler, C. Lambert and F. Würthner. *Adv. Energy Mater.*, **7**(16):1700236, (2017).

[28] A.S. Bondarenko, I. Patmanidis, R. Alessandri, P.C. T. Souza, T.L. C. Jansen, A.H. de Vries, S. J. Marrink and J. Knoester. *Chem. Sci.*, **11**(42):11514–11524, (2020).

[29] M. Cho, T. Brixner, I. Stiopkin, H. Vaswani and G.R. Fleming. *J. Chin. Chem. Soc.*, **53**(1):15–24, (2006).

[30] P. Hamm and M. Zanni. *Concepts and Methods of 2D Infrared Spectroscopy.* Cambridge University Press, Cambridge, 2011.

[31] V. Tiwari, Y.A. Matutes, A.T. Gardiner, T.L.C. Jansen, R.J. Cogdell and J.P. Ogilvie. *Nat. Commun.*, **9**(1):4219, (October 2018).

[32] M. Mohseni, P. Rebentrost, S. Lloyd and A. Aspuru-Guzik. *J. Chem. Phys.*, **129**(17):174106, (November 2008).

[33] S. Lloyd, M. Mohseni, A. Shabani and H. Rabitz. *arXiv:1111.4982 [physics, physics:quant-ph]*, (November 2011).

[34] T. Kunsel, T.L.C. Jansen and J. Knoester. *J. Chem. Phys.*, **155**(13):134305, (October 2021).

[35] Y. Tanimura and R. Kubo. *J. Phys. Soc. Jpn.*, **58**(4):1199–1206, (1989).

[36] Y. Tanimura. *Phys. Rev. A*, **41**(12):6676–6687, (June 1990).

[37] A. Ishizaki and G.R. Fleming. *J. Chem. Phys.*, **130**(23):234111, (June 2009).

[38] C. Kreisbeck and T. Kramer. *J. Phys. Chem. Lett.*, **3**(19):2828–2833, (October 2012).

[39] R.P. Feynman. *Phys. Rev.*, **56**(4):340–343, (August 1939).

[40] J.C. Tully. *J. Chem. Phys.*, **93**(2):1061–1071, (July 1990).

[41] R. Tempelaar, C.P. van der Vegte, J. Knoester and T.L.C. Jansen. *J. Chem. Phys.*, **138**(16):164106, (April 2013).

[42] J. Knoester and V.M. Agranovich. Frenkel and Charge-Transfer Excitons in Organic Solids. *Thin Films and Nanostructures*, volume 31 of *Electronic Excitations in Organic Nanostructures*, pages 1–96.
Academic Press, (January 2003).

[43] J.R. Albani. *Structure and Dynamics of Macromolecules: Absorption and Fluorescence Studies*. Elsevier, August 2011.

[44] J. Strümpfer and K. Schulten. *J. Chem. Theory Comput.*, **8**(8):2808–2816, (August 2012).

[45] K.M. Ramachandran and C.P. Tsokos. *Mathematical Statistics with Applications*. Elsevier, 2009.

[46] A. Bastida, C. Cruz, J. Zúñiga, A. Requena and B. Miguel. *J. Chem. Phys.*, **126**(1):014503, (January 2007).

[47] M. Aghtar, J. Liebers, J. Strümpfer, K. Schulten and U. Kleinekathöfer. *J. Chem. Phys.*, **136**(21):214101, (June 2012).

[48] P. Nijjar, J. Jankowska and O.V. Prezhdo. *J. Chem. Phys.*, **150**(20):204124, (May 2019).

[49] D.W. Oxtoby. *Annu. Rev. Phys. Chem.*, **32**(1):77–101, (1981).

[50] J.S. Bader and B.J. Berne. *J. Chem. Phys.*, **100**(11):8359–8366, (June 1994).

[51] A.S. Bondarenko, T.L.C. Jansen and J. Knoester. *J. Chem. Phys.*, **152**(19):194302, (May 2020).

[52] D.M. Eisele, C.W. Cone, E.A. Bloemsma, S.M. Vlaming, C.G.F. van der Kwaak, R.J. Silbey, M.G. Bawendi, J. Knoester, J.P. Rabe and D.A. Vanden Bout. *Nat. Chem.*, **4**(8):655–662, (August 2012).

[53] M.E. Madjet, A. Abdurahman and T. Renger. *J. Phys. Chem. B*, **110**(34):17268–17281, (August 2006).

[54] K. Huang. *Statistical Mechanics.* Wiley & Sons, second edition, 1987.

[55] N.G. van Kampen. *Stochastic Processes in Physics and Chemistry.* Elsevier, 1992.

[56] D. Cringus, T.L.C. Jansen, M.S. Pshenichnikov and D.A. Wiersma. *J. Chem. Phys.*, **127**(8):084507, (August 2007).

[57] S.J. Blundell and K.M. Blundell. *Concepts in Thermal Physics.* Oup Oxford, 2009.

[58] H. Haken and G. Strobl. *Z. Physik*, **262**(2):135–148, (April 1973).

[59] H. Kim and P.J. Rossky. *J. Chem. Phys.*, **125**(6):066101, (August 2006).

[60] S.A. Egorov, K.F. Everitt and J.L. Skinner. *J. Phys. Chem. A*, **103**(47):9494–9499, (November 1999).

[61] C. Olbrich, T.L.C. Jansen, J. Liebers, M. Aghtar, J. Strümpfer, K. Schulten, J. Knoester and U. Kleinekathöfer. *J. Phys. Chem. B*, **115**(26):8609–8621, (July 2011).

[62] J. Koepke, X. Hu, C. Muenke, K. Schulten and H. Michel. *Structure*, **4**(5):581–597, (May 1996).

[63] R. Bloem, A.G. Dijkstra, T.L.C. Jansen and J. Knoester. *J. Chem. Phys.*, **129**(5):055101, (August 2008).

[64] T.L.C. Jansen and J. Knoester. *J. Phys. Chem. B*, **110**(45):22910–22916, (November 2006).

[65] T.L.C. Jansen and J. Knoester. *Acc. Chem. Res.*, **42**(9):1405–1411, (September 2009).

[66] T.L.C. Jansen, B.M. Auer, M. Yang and J.L. Skinner. *J. Chem. Phys.*, **132**(22):224503, (June 2010).

[67] C. Liang and T.L.C. Jansen. *J. Phys. Chem. B*, **117**(23):6937–6945, (June 2013).

[68] C. Liang, M. Louhivuori, S.J. Marrink, T.L.C. Jansen and J. Knoester. *J. Phys. Chem. Lett.*, **4**(3):448–452, (February 2013).

[69] T.L.C. Jansen, W. Zhuang and S. Mukamel. *J. Chem. Phys.*, **121**(21):10577–10598, (December 2004).